UNIVERSITÀ DEGLI STUDI DI PADOVA

Dipartimento di Fisica e Astronomia "Galileo Galilei"

Master Degree in Physics

Final Dissertation

An experimental setup for the detection of e^+e^- pairs in the decay of $^8Be^*$

Thesis supervisor

Prof. Gianmaria Collazuol

Thesis co-supervisor

Dr. Tommaso Marchi

Candidate

Riccardo Bolzonella

Academic Year 2020/2021

An experimental setup for detection of e^+e^- pairs in the decay of $^8Be^*$

Riccardo Bolzonella

Abstract

The existence of a light neutral boson, possible mediator of a new fundamental interaction, has been recently proposed by A.J. Krasznahorkay and collaborators [1]. A series of experiments was carried out at the Atomki laboratory (Debrecen, Hungary) measuring electron-positron pairs emitted in the decay of excited ^8Be and ^4He. Anomalies in the e^+e^- angular correlation distributions with respect to the Internal Pair Creation (IPC) process have been reported. The first results concern the decay of the 18.15 MeV 1^+ state in ^{8}Be, while the group later focused on the ≈ 20 MeV excited states in ^{4}He [2].

In order to explain the reported anomaly several interpretation have been developed. The approach proposed by X. Zhang and G. Miller aims to describe the anomalies in an almost conventional nuclear physics framework, improving the reaction modeling. Conversely, a possible interpretation given by J. Feng and collaborators involves the appearance of a new gauge vector boson, called X17, that could possibly mediate the interaction between the SM and the dark sector.

The Atomki results and the related interpretations triggered a renewed interest in the spectroscopy of light ions by Internal Pair Creation. At this purpose, a new experimental setup is being developed at the INFN Legnaro National Laboratories of INFN (Legnaro, Padova, Italy). The first goal is to provide an independent replica of the Hungarian experiment.

This thesis work focuses on a complete simulation of the proposed setup and reports about the first experimental characterization of the prototype detectors. The text is organized as follows: after a short introduction on the physics of electromagnetic transitions and internal pair production in nuclei, the state of the art regarding the ^8Be and the ^4He anomalies will be discussed, explaining the roots of the X-boson or X17 case. Afterwards, the simulation and the experimental characterization works will be reported.

Contents

1

Internal Pair Creation in nuclear transitions

The subject of this thesis is the development of an experimental setup to measure e^+e^- pairs emitted by Internal Pair Creation (IPC) in nuclear decays. This chapter summarizes the general framework of electromagnetic transitions in nuclei and provides a dedicated focus on the electron/positron-emitting channels.

It is well known that unstable and excited nuclei emit radiation (charged particles, neutrons and gamma-rays) in order to reach a more stable configuration. The most common decay modes are:

α **decay** that consists in the emission of a ${}^4_2\mathrm{He}_2$ nucleus, also called α particle, following the reaction

$$ {}^A_Z X_N \rightarrow {}^{A-4}_{Z-2} Y_{N-2} + {}^4_2 He_2 \tag{1.1} $$

where X and Y are the initial and final nuclei, respectively. Z represents the number of protons, N the number of neutrons and A is the sum of the two, namely the number of nucleons.

β **decay** that consists in the emission or capture of electrons and positrons, called β^- and β^+, involving the weak interaction through three possible decays:

- β^- emission: $n \rightarrow p + e^- + \overline{\nu_e}$
- β^+ emission: $p \rightarrow n + e^+ + \nu_e$
- electron capture: $p + e^- \rightarrow n + \nu_e$

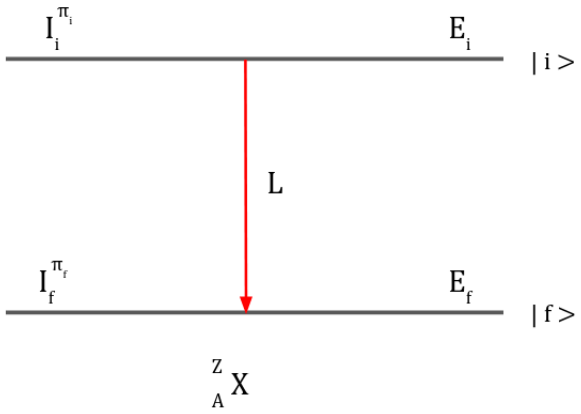

Figure 1.1: Scheme of a γ transition from an initial state of the nucleus ${}^{Z}_{A}X$ described by a wave function $|i>$ with energy E_i and isospin and parity $I_i^{\pi_i}$ to a final state of the same nucleus described by a wave function $|f>$ with energy E_f and isospin and parity $I_f^{\pi_f}$.

fission where a nucleus splits into two smaller fragments, possibly emitting one or more neutrons.

γ **decay** the consists in the emission of a γ ray from an excited state of a nucleus, resulting in a transition to a lower energy state.

The latter mechanism is of particular interest for this work because it connects an initial excited state at energy E_i described by a wave function $|i>$ to a final state at energy E_f with wave function $|f>$, as depicted in figure 1.1. Gamma-ray emission is normally the dominating process linking two nuclear states, but second order effects like Internal Conversion and Internal Pair Creation might play a role and, as we will see in the following paragraphs, there are specific cases where they represent the only allowed transition mode. The emission of two photons or more than two leptons are also possible process but their study goes beyond the scope of the present work.

It is worth recalling that there are several ways to populate an excited state of a nucleus: certainly most of the α and β decays leave the nuclei in an excited state, but a very effective way for populating selected nuclei in specific excited states is via nuclear reactions. Among the others, resonant reactions at low energy represent a very selective mechanism that is widely used for gamma and particle spectroscopy in nuclear physics. The q-value of the reaction can be exploited for populating states with energies that are much larger than the beam kinetic energy. As an example we can consider the p+^{7}Li reaction used in reference [1]

where 1 MeV beam energy allows to populate 18 MeV states in ^8Be.
We will now focus on the electromagnetic transitions depopulating such states, starting from the most common gamma decay.

1.1 γ-ray emission

The formalism of γ transitions is well known and it sets the ground for the Internal Pair Creation formalism that will be considered in the following paragraphs.

We consider a nucleus with mass M, at rest and a transition from an initial state with energy E_i to a final state at energy E_f. In the final state the nucleus will have recoil momentum and energy of p_R and $T_R = \frac{p_R^2}{2M}$, respectively. The momentum and energy conservation imposes:

$$E_i = E_f + E_\gamma + T_R \tag{1.2}$$

$$0 = \mathbf{p}_r + \mathbf{p}_\gamma \tag{1.3}$$

So, having $E_\gamma = cp_\gamma$, the energy difference between the initial and the final states is

$$\Delta E = E_\gamma + \frac{E_\gamma^2}{2Mc^2} \tag{1.4}$$

Thus, the energy of the emitted photon will be

$$E_\gamma = Mc^2 \left[-1 \pm \left(1 + 2\frac{\Delta E}{Mc^2} \right)^{\frac{1}{2}} \right] \tag{1.5}$$

In the typical case of $\frac{\Delta E}{Mc^2} \ll 1$, the previous relation could be approximated to

$$E_\gamma \simeq \Delta E - \frac{\Delta E^2}{2Mc^2} \simeq \Delta E \tag{1.6}$$

and the emitted photon energy is in a good approximation equivalent to the energy differences between the nuclear states involved [3].

Multipole expansion

Charge and current distribution generate electric and magnetic fields (if the distributions are static) or radiative fields (if the distributions change in time) that could be expanded and studied in terms of multipole orders as a function of the multipole momentum representing them.

A charge $+q$ and a second charge $-q$ in a position $\vec{z}$ with respect to the first one produce a static electric dipole $\vec{d} = q\vec{z}$. On the other hand, a magnetic dipole momentum is described by a circular spire of area A in which a current i flows: considering a versor $\vec{n}$ orthogonal to A forming a right-handed basis with the radial versor $\vec{r}$ and the current i direction, the magnetic dipole momentum is $\vec{\mu} = iA\vec{n}$. If the dipole momenta change in time, a radiation field is generated.

If L is the radiation index, the electric field E at a certain multipole order 2^L is proportional to $\frac{1}{r^{L+1}}$, while the magnetic field B is proportional to $\frac{1}{r^L}$. In general, electric and magnetic radiations are respectively named as EL and ML. Details about the multipole expansion can be found in reference [3], but the relevant features are reported:

- the radiation angular distribution is described by Legendre polynomials $P_{2^L}(\cos\theta)$;
- radiation fields parity is

$$\pi(ML) = (-1)^{L+1} \tag{1.7}$$

$$\pi(EL) = (-1)^{L} \tag{1.8}$$

- the emitted power is, considering $\sigma = E$ or M,

$$P(\sigma L) = \frac{2(L+1)c}{\epsilon_0 L\left[(2L+1)!!\right]^2}\left(\frac{\omega}{c}\right)^{2L+2}\left[m(\sigma L)\right]^2 \tag{1.9}$$

  where $m(\sigma L)$ is the multipole momentum amplitude.

In a quantum description both the radiation field sources, i.e. the multipole momenta, are quantized. They are replaced by operators bringing the nucleus from an initial state ψ_i to a final one ψ_f, and the multipole momentum amplitude is replaced by the multipole operator matrix element

$$m_{fi}(\sigma L) = \int \psi_f^* O(\sigma L)\,\psi_i dv = \langle\psi_f|\,O(\sigma L)\,|\psi_i\rangle \tag{1.10}$$

where $O(\sigma)$ are the multipole operators.

The multipole operators are $O(\sigma L) = er^L Y_{LM}(\Theta,\Phi)$: the included spherical harmonic function is related to an angular momentum L, so a multipole radiation of order L emits a photon with angular momentum $L\hbar$.
Recalling figure 1.1, considering a transition from an initial state with angular momentum $\mathbf{I}_i$ and parity π_i, that from now on will be expressed as $\mathbf{I}_i^{\pi_i}$, to a final

state $\mathbf{I}_f^{\pi_f}$, the allowed angular momentum values L are constrained by the angular momentum conservation $\mathbf{I}_i = \mathbf{I}_f + L$, and for each allowed value L the parity variation ΔE selects the type of transition (E or M) following the equations 1.7 and 1.8.
If $\mathbf{I}_i = \mathbf{I}_f = \mathbf{0}$ the emission of a single photon is strictly forbidden by spin conservation ($L \neq 0$) [3]: thus the multipole operator matrix element vanishes:

$$m_{fi}(\sigma L) = \langle \psi_f | O(\sigma L) | \psi_i \rangle = \langle 0 | L | 0 \rangle = 0 \tag{1.11}$$

The electromagnetic transitions via photon emission allowed by the selection rules, for $L \leq 3$, are reported in the table 1.1

L	Transition name	$\pi_i \pi_f = +1$	$\pi_i \pi_f = -1$
0	monopole	*forbidden*	*forbidden*
1	dipole	M1	E1
2	quadrupole	E2	M2
3	octupole	M3	E3

Table 1.1: Summary of the electromagnetic transitions with index $L \leq 3$.

The photon emission probability (or transition rate), is given by the number of photons of energy $\hbar\omega$ emitted:

$$\lambda(\sigma L) = \frac{P(\sigma L)}{\hbar\omega} = \frac{2(L+1)}{\epsilon_0 \hbar L [(2L+1)!!]^2} \left(\frac{\omega}{c}\right)^{2L+1} [m_{fi}(\sigma L)]^2 \tag{1.12}$$

Assuming that the radial term in the wave function is constant at $r \leq R$, where R is the nuclear radius, and null at $r > R$, it is possible to obtain the transition probability in the Weisskopf approximation:

$$\lambda(EL) \propto A^{\frac{2L}{3}} \frac{r_0^{2L}}{(L+3)^2} E^{2L+1} \tag{1.13}$$

$$\lambda(ML) \propto A^{\frac{2L-2}{3}} \frac{r_0^{2L-2}}{(L+3)^2} E^{2L+1} \tag{1.14}$$

Those expressions are commonly used for computing reference evaluations of the transition probabilities. The case of a nucleus with A=125 is reported in figure 1.2 where it is possible to notice that the lower multipole orders are dominant, with the transition probability decreasing of almost 10^5 for each following order. Moreover, the electric transition are sistematically favored with respect to the

magnetic one at the same multipole order.

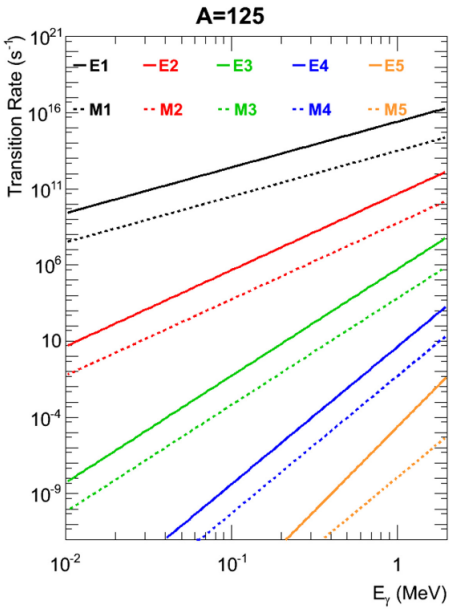

Figure 1.2: Electromagnetic transition rates of different multipole orders as functions of the transition energy. [4]

Cross section and decay rates

The S-matrix describing the emission of a photon is:

$$\hat{S}^{(1)} = -ie \int d^4x \hat{j}_n(x) \cdot \hat{A}(x) \tag{1.15}$$

where $\hat{A}$ is the electromagnetic field operator, and $\hat{j}_n$ the nuclear current operator [5]. The latter depends on the nuclear model considered while the electromagnetic field operator depends on the transition energy ω, the photon angular momentum L, the magnetic quantum number M, the type of transition (electric or magnetic) τ and the parity. Thus, this operator is composed by two different operators $A_L^{M\ electric}$ and $A_L^{M\ magnetic}$. The nucleus instead is described by the initial and final angular momentum and parity (J_i, M_i), (J_f, M_f), π_{n_i} and π_{n_f}.
The parity change is given by $\pi_n = \pi_{n_i}\pi_{n_f}$. Expanding the S-matrix it results that the only transitions contributing to the decay rate are the ones with $\pi_n = (-1)^{L+1-\lambda}$, where $\lambda = 0$ for magnetic transitions and $\lambda = 1$ for electric ones.

Integrating over the possible transition energies the photon emission probability

results

$$P_\gamma = \frac{8\pi\alpha\omega}{2J_i+1} \sum_{M_i=-J_i}^{J_i} \sum_{M_f=-J_f}^{J_f} \sum_{L=1}^{\infty} \sum_{M=-L}^{L} \sum_{\tau=e,m} |V_\gamma^{(\tau)}|^2 \tag{1.16}$$

where, naming the nucleus radius r_n,

$$V_\gamma^{(\tau)} = \int_0^\infty d\tau_n j_n(r_n) \cdot A_L^{M(\tau)}(\omega r_n) \tag{1.17}$$

1.1.1 Alternative mechanisms

The γ transition is not the only way in which an excited nucleus can decrease its energy and decay to a lower energy state.
Higher order contributes compete with this kind of decay: among this higher order contributes the dominant ones are the internal conversion and the internal pair production, but other contributes, like the emission of more photons, could compete with these mechanisms.
In this paragraph the internal conversion and the internal pair creation will be briefly introduced. Since the internal pair creation is a more interesting topic for this thesis work, it will be described in more detail in section 1.3.

In this mechanisms the radiation field interacts, respectively, with an electron in the negative energy continuum or an atomic electron. In the latter case if the transition energy is sufficient the atomic electron is emitted, as shown in figure 1.3**b**.
In the former case, if the transition energy ω is lower than $2m_e$, an electron in the negative energy continuum is promoted to a bound state, and the hole left by the electron results in the emission of a mono-energetic positron, as shown in 1.3**c**. Instead, if ω is greater than $2m_e$, an electron in the negative energy continuum with energy $\epsilon = -E < -m_e$ could be promoted to the positive energy continuum, at the energy $E' = \epsilon + \omega > m_e$, as shown in figure 1.3**a**. As in the previous case the hole is emitted as a positron, so this process results in a e^+e^- pair emission. In the latter case neither the initial or the final states are at fixed energy, so the electron and the positron energy distribution are expected to be continuous.

1.2 Internal conversion

As said, the internal conversion is given by the interaction of the radiation field with an atomic electron, causing the electron emission.
Differently from the β decay, this process involves an already available electron that is not created in the process itself. Following the electron emission, one of

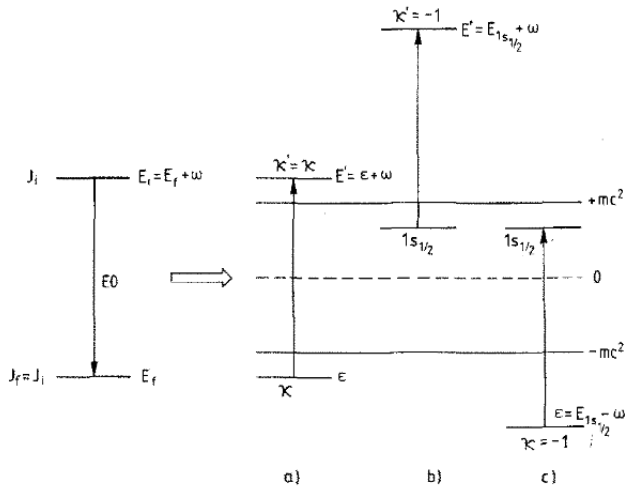

Figure 1.3: Internal conversion processes: (**a**) e^+e^- pair creation leading to a continuum energy spectrum; (**b**) internal conversion of an electron in the K shell; (**c**) mono-energetic positron production. [3]

the atomic electrons from a higher orbit fills the vacancy, and an X-ray is emitted. In a transition between two states with an energy gap ΔE, the electron kinetic energy will be $T_e = \Delta E - B$, where B is the electron binding energy. The transition energies and the electron binding energy are characteristic for each nucleus and atoms, so the energy spectrum of electrons emitted by internal conversion is discrete.
Moreover, by looking at the kinetic energy of the emitted electron, it is clear that there is a minimum energy required for the process to take place, that is the binding energy of a particular atomic shell [3].

The internal conversion coefficient (ICC) is the ratio between the internal conversion rate (λ_e) and the equivalent gamma rate (λ_γ):

$$\alpha = \frac{\lambda_e}{\lambda_\gamma} \tag{1.18}$$

It provides the branching ratio of internal conversion with respect to gamma-ray emission. Clearly, this coefficient can not be considered for $E0$ transitions, because the γ-ray emission is forbidden. Indeed, the IC and the IPC become the main processes in the case of $E0$ transitions. The ICC does not depend on the nuclear structure: indeed, since the matrix elements $m_{fi}\,(\sigma L)$ for the γ-ray emission and the internal conversion coincide, the nuclear wave functions ψ_i and ψ_f are ruled out by these two processes amplitudes ratio. The coefficient instead

depends on the atomic number, on the transition energy and on the transition multipolarity [3].

$$\alpha\left(EL\right) \propto \frac{Z^3}{n^3}\frac{L}{L+1}\left(\frac{1}{E}\right)^{L+\frac{5}{2}} \tag{1.19}$$

$$\alpha\left(ML\right) \propto \frac{Z^3}{n^3}\left(\frac{1}{E}\right)^{L+\frac{3}{2}} \tag{1.20}$$

It is worth to notice that the ICC:

- increases as the atomic number increases;
- decreases as the transition energy increases;
- increases as the multipole order increases;
- it decreases as $\frac{1}{n^3}$, where n is the atomic shell number.

1.3 Internal Pair Creation

The Internal Pair Creation mechanism is of particular interest for this thesis work, so it is worthy introduce in more detail this process.
In this section the theoretical description of internal pair creation will be described in more detail, explaining the prediction related to the Internal Pair Creation Coefficient (indicating how much this process competes with the γ decay) and the distribution of the correlation angle between the two leptons in the pair.

1.3.1 The Internal Pair Creation Coefficient

The Internal Pair Creation Coefficient (IPCC) is defined, analogously to the internal conversion, as

$$\beta = \frac{P_{e^+e^-}}{P_\gamma} \tag{1.21}$$

where $P_{e^+e^-}$ and P_γ are the photon and pair emission probability in a certain decay.
It is possible to express the IPCC also as an integral with respect to the positron energy, as

$$\beta = \int_{m_e}^{\omega - m_e} \frac{d\beta}{dE}\left(E\right) dE \tag{1.22}$$

where ω is the transition energy, while $d\beta/dE$ is called *differential pair creation coefficient* (DPCC).
Analogously to the IC case, this coefficients could not be referred to the $E0$ transitions.

The IPCC mechanism has non negligible effects, as we will see, at high transition energies (on the contrary of the internal conversion, which is more important at low energies).
In the following paragraphs the calculation performed by P. Schlüter, G. Soff and W. Greiner [5] will be presented. The IPCC will be calculated in the lowest non-vanishing order of perturbation expansion (referred as Born approximation). Moreover, it will result that for high transition energy ω and low atomic number Z the full calculation are compatible to the Born approximation result.

Pair emission

Recalling the photon emission probability computation presented in section 1.1, analogous computation will be performed to obtain the pair emission probability. The S-matrix describing the emission of a e^+e^- pair is

$$\hat{S}^{(2)} = -\frac{1}{2}e^2 \iint d^4x d^4y \hat{T}\left[\hat{j}_\mu(x)\hat{A}^\mu(x)\hat{j}_\nu(y)\hat{A}^\nu(y)\right] \tag{1.23}$$

Neglecting the nuclear component of the current, the current becomes

$$\hat{j}_\mu = \hat{j}_{\mu e} = \hat{\overline{\psi}}(x)\gamma_\mu\hat{\psi}(x) \tag{1.24}$$

The matrix element becomes

$$S_{if}^{(2)} = \left\langle f_n f_e f_A | \hat{S}^{(2)} | i_n i_e i_A \right\rangle \tag{1.25}$$

The initial and final states of the electron i_e and f_e are described by energy $-E$ and E', Dirac quantum number κ and κ', and z-projection of the angular momentum μ ad μ'. Thus, E is the energy of the emitted positron.

Integrating as in the photon emission case, it results

$$P_{e^+e^-} = \frac{2\pi}{2J_i+1}\sum_{M_i=-J_i}^{J_i}\sum_{M_f=-J_f}^{J_f}\sum_{\kappa\neq 0}\sum_{\kappa'\neq 0}\sum_{\mu=-j}^{j}\sum_{\mu'=-j'}^{j'} W_{e^+e^-} \tag{1.26}$$

where

$$W_{e^+e^-} = \int_{m_e}^{\omega-m_e} |U_{if}^{(2)}|^2 \tag{1.27}$$

and $U_{if}^{(2)}$ is the matrix element Green function analogous to the photon emission case with the appropriate substitutions.

Final results

The Green function in matrix element $U_{if}^{(2)}$ could be factorized in its magnetic, electric and monopole terms, as

$$U_{if}^{(2)} = \sum_{L=1}^{\infty} \sum_{M=-L}^{L} \left[U_{if}^{m}(L,M) + U_{if}^{e}(L,M) \right] + U_{if}^{L=0} \tag{1.28}$$

The monopole term has no analogue to a real photon emission, as explained in section 1.1, since only the scalar and longitudinal vector term contribute. Not having a real photon emission analogue, it is not possible to define a IPCC for this term, so it will be calculated for $L \geq 1$.

These components are expanded as function of the nuclear and electronic current, and then integrated over the radius and the angle.

In this way, with only algebraic calculations from now on, it is possible to estimate the DPCC for electric and magnetic transitions.
It results

$$\frac{d\beta}{dE}(EL) = \sum_{\kappa,\kappa'} A_{\kappa,\kappa'} \left| \left(\kappa - \kappa'\right)(R_3 + R_4) + L\,(R_1 + R_2 + R_3 - R_4) \right|^2 \tag{1.29}$$

$$\frac{d\beta}{dE}(ML) = \sum_{\kappa,\kappa'} B_{\kappa,\kappa'} |R_5 + R_6|^2 \tag{1.30}$$

where A and B are functions of $L, j, j', \kappa, \kappa'$ and ω, while R_i are integrals of radial functions.

Numerical results have been estimated by using a point nucleus approximation, namely substituting in the R_i integrals the wave functions for a point nucleus. The results obtained with these calculation, shown in figure 1.4 with a full line, compared with the results obtained using a Born approximation corrected with a Coulomb factor (dashed-dotted line), it is possible to see that at low transition energies the corrected Born approximation is compatible with the full calculation. The deviation grows with the transition energy and the atomic number.

Finally, the internal pair creation coefficient behaves as:

$$\beta(\tau L) \propto \frac{\omega}{(2L+1)\,L\,(L+1)} \int_{m_e}^{\omega - m_e} R^{\tau}(\omega r_n) \tag{1.31}$$

where R^{τ} are the terms in the absolute values in the equations 1.29 and 1.30.

Summarizing the results, generally the internal pair creation coefficient:

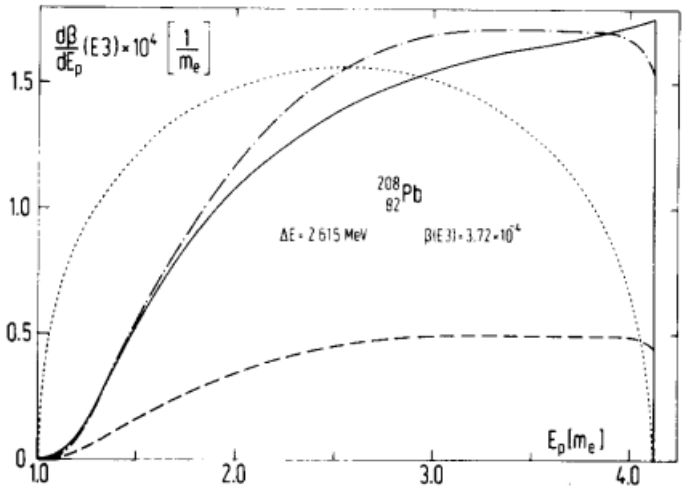

Figure 1.4: Internal pair creation coefficient with respect to positron energy E_p for the E3 transition $^{208}Pb\,(3^-; 2.615\text{ MeV}) \rightarrow^{208} Pb\,(g.s.)$. The full line represents the complete calculation in a point nucleus approximation; the dotted line is the prediction with the Born approximation; this function is multiplied by a Coulomb correction (dashed line), resulting in the corrected Born approximation (dashed-dotted line). [5]

- increases as the transition energy grows;
- slightly decreases with increasing atomic number Z;
- increases with increasing transition multipole order L.

Numerical calculation of the IPCC and the DPCC have been performed basing on the calculation just presented, obtaining tables of the two coefficients values at several transition energies as functions of the type of transition [6].

1.3.2 The correlation angle distribution

Theoretical prediction of the correlation angle distribution

A theoretical description of the distribution of the correlation angle between the electron and the positron emitted is proposed by M.E.Rose [7].
The results proposed have been calculated referring to the total counting rates, integrated over the energies of the particles, because the integral angular correlation predictions are more accurate. Indeed, the nuclear Coulomb field suppresses the number of slow positrons and enhances the number of fast ones, and these effects are canceled out by the integration.

Representing the radiation field with a scalar potential V and a vector one $\mathbf{A}$,

let's name the electron and positron energies, momentum and emission polar coordinates $E_\pm$, $p_\pm$ $\theta_\pm$ and $\phi_\pm$.
The ratio of the number of pairs per second, with e^- and e^+ traveling in the solid angles $d\Omega_-$ and $d\Omega_+$ and the positron energy included between E_+ and $E_+ + dE_+$, to the number of emitted photons per second, is

$$d\gamma_L\left(E_+;\theta_+,\phi_+;\theta_-,\phi_-\right) = \frac{\alpha\omega}{32\pi^2} p_+ p_- E_+ E_- \sum_{s_- s_+} |\langle\psi_-|V + \vec{\alpha}\cdot\mathbf{A}|\psi_+\rangle|^2 d\Omega_- d\Omega_+ dE_+ \tag{1.32}$$

The distribution of the correlation angle is obtained by integrating over the two solid angles, namely

$$\gamma_l\left(\Theta\right) = \int \left(d\gamma_l/d\Omega_- d\Omega_+ dE_+\right)\sin\theta d\theta d\phi \tag{1.33}$$

and it results, naming $\mathbf{q} = \mathbf{p}_+ + \mathbf{p}_-$:

- for the electric multipoles

$$\begin{aligned}\gamma_L\left(\Theta\right) = {} & \frac{2\alpha}{\pi\left(L+1\right)}\frac{p_+ p_-}{q}\frac{\left(q/\omega\right)^{2L-1}}{\left(\omega^2-q^2\right)^2} \\ & \times\left\{\left(2L+1\right)\left(E_+E_- + 1 - \frac{1}{3}p_+p_-\cos\Theta\right)\right. \\ & + L\left(\frac{q^2}{\omega^2}-2\right)\left(E_+E_- - 1 + p_+p_-\cos\Theta\right) \\ & \left. + \frac{1}{3}\left(L-1\right)p_+p_-\left[\frac{3}{q^2}\left(p_- + p_+\cos\Theta\right)\left(p_+ + p_-\cos\Theta\right) - \cos\Theta\right]\right\}\end{aligned} \tag{1.34}$$

- for the magnetic multipoles

$$\gamma_L\left(\Theta\right) = \frac{2\alpha}{\pi}\frac{p_+p_-}{q}\frac{\left(q/\omega\right)^{2L+1}}{\left(\omega^2-q^2\right)^2}\left\{1 + E_+E_- - \frac{p_+p_-}{q^2}\left(p_- + p_+\cos\Theta\right)\left(p_+ + p_-\cos\Theta\right)\right\} \tag{1.35}$$

By integrating these results over Θ the total pair creation coefficient is obtained, and it will be equivalent to the equation 1.31 found in 1.3.1:

$$\beta_L\left(E_+\right) = \int_0^\pi \gamma_L\left(\Theta\right)\sin\Theta d\Theta \tag{1.36}$$

This results don't consider the presence of a preferential direction, but have been

obtained by considering an isotropic distribution of **q**.
Afterwards, G. Goldring improves this model considereding an anisotropic emission in the decay of an excited nucleus, due to the preferential direction given by the direction of the beam used to excite the nucleus [8].
The resulting formula simplifies a lot if the calculations are performed on a plane orthogonal to the beam direction, since the interference terms between different multipole terms are canceled. For these reason in most of the experiments searching for pairs emitted by internal pair creation the detectors are placed orthogonally with respect to the beam.

Experimental comparison

In a following paper Goldring and S. Devons measured the pairs emitted in some high energy γ-transitions in light nuclei [9], and compared the measured correlation angle distribution with the one expected by their work described in the paragraph 1.3.1 [8].

Let's define $\Lambda = L$ for the electric transitions and $\Lambda = L + 1$ for the magnetic ones, in order to interpret the results that will be shown in figure 1.5.
The experimental data have been compared with the theoretical curves predicted for electric or magnetic transition at different multipole orders.

The investigated transitions were:

(a) ${}^{7}Li\,(p,\gamma)^{8}\,Be$ with proton bombarding energy $E_p = 440$ keV; this is a M1 transition, and it is clear the agreement between the experimental data and the predicted theoretical distribution in a M1 transition;

(b) ${}^{9}Be\,(p,\gamma)^{10}\,B$ with $E_p = 998$ keV; it results to be a mix between E1, E3 and M2 multipoles;

(c) ${}^{19}F\,(p,\alpha\gamma)^{16}\,O$ with $E_p = 340$ keV; this was known to be an E3 transition, and again the agreement between the experimental data and the theoretical prediction is very good.

Summarizing, the theoretical model developed by Rose and improved by Goldring is expected to predict with a very good accuracy the angular correlation distribution of pairs emitted in the decay of light nuclei. Its prediction will later be considered as the current nuclear physics model most accurate prediction for the correlation angle distribution.

Based on Rose model, Gulyas calculated the angular correlation of e^+e^- pairs emitted by IPC for different multipolarities at a transition energy $E = 17$ MeV, shown in figure 1.6 [10].

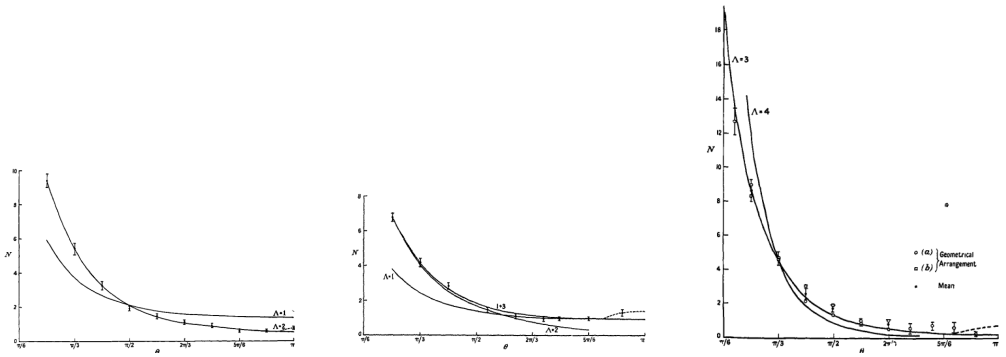

(a) (b) (c)

Figure 1.5: Angular correlation of pairs emitted in the reactions $^{7}Li\,(p,\gamma)^{8}\,Be$ (**a**), $^{9}Be\,(p,\gamma)^{10}\,B$ (**b**) and $^{19}F\,(p,\alpha\gamma)^{16}\,O$ (**c**), compared to the theoretical curves (full lines) predicted for different multipolarities. [9]

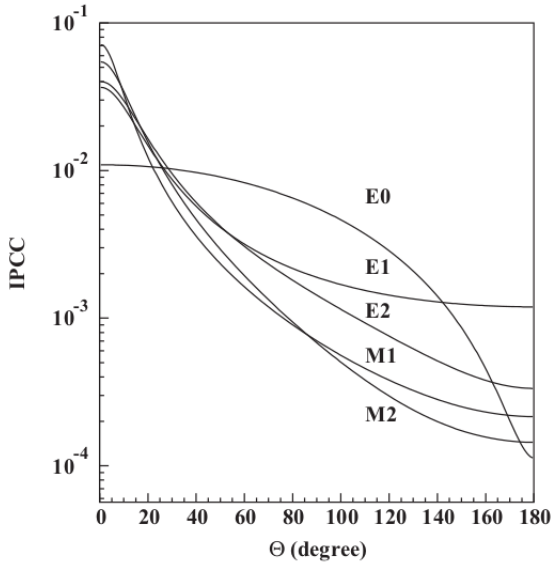

Figure 1.6: Angular correlation of $e^{+}e^{-}$ pairs emitted by IPC for different multipolarities at a transition energy $E = 17$ MeV based on Rose's model. [10]

Later, other experiment kept on studying the internal pair creation, aiming to verify the correctness of the reported model developing several pair spectrometers [11, 12]. In the context of these studies first hints of the presence of anomalies have been introduced [13–15].

2

Internal Pair Creation anomalies in light nuclei

In 2016 A. J. Krasznahorkay and collaborators (Atomki Laboratory, Debrecen, Hungary) reported the observation of an anomalous peak-like excess in the distribution of the correlation angle between the e^+ and e^- produced in pairs in the decay of an excited state of $^8Be^*$ [1]. The experiment was carryed out by measuring the $M1$ transition $^8Be\,(18.15\text{ MeV}\,;1^+) \rightarrow\ ^8Be\,(g.s.)$, depopulating the 18.15 MeV isoscalar 1^+ state [1].
The same authors suggested the hypothesis of the existence of a new light, neutral boson, possible mediator of a new fundamental interaction.

In 2019 the same group published new evidences supporting the earlier findings with new experimental data.
The experiment on $^8Be^*$ was repeated with an improved setup, and the excess in the correlation angle distribution has been observed again.
Moreover, the evidence of a similar anomaly in the $E0$ transition $^4He\,(21.01\text{ MeV}\,;0^-) \rightarrow\ ^4He\,(g.s.)$ was observed [2].

The evidenced anomalies and the proposed hypothesis began to stimulate the interest of a large number of research groups, and several hypothesis aiming to explain the anomaly have been discussed [16–19].

In the following sections the performed experiments and the possible interpretation will be described in detail.

It is worth recalling that IPCC anomalies had been previously reported in similar cases, but with different results [13–15]. In addition to the specific interpretations,

the recent data call for a global understanding of the phenomenon.

2.1 $^8Be^*$ decay and observed anomaly

2.1.1 Physics processes

The ^8Be structure is reported in figure 2.1, its ground state is unstable and decays in two α particles.
The reaction $^7Li\,(p, e^+e^-)^8\,Be$ has been exploited to populate some of the $^8Be^*$ resonant states (see figure 2.2). The Q-value of the reaction is 17.2551 MeV, therefore using protons respectively at the resonant energies $E_p = 0.441$ MeV and $E_p = 1.03$ MeV the two states at 17.64 MeV and 18.15 MeV are populated.
The transitions connecting this states with the ground state and the 3.03 MeV one, shown in figure 2.2, have been investigated to measure pairs emission; in particular, they are:

- isovector $M1$ $^8Be\,(17.64\text{ MeV}\,;1^+) \rightarrow\ ^8Be\,(g.s.)$
- isovector $M1$ $^8Be\,(17.64\text{ MeV}\,;1^+) \rightarrow\ ^8Be\,(3.03\text{ MeV}\,;2^+)$
- isoscalar $M1$ $^8Be\,(18.15\text{ MeV}\,;1^+) \rightarrow\ ^8Be\,(g.s.)$
- isoscalar $M1$ $^8Be\,(18.15\text{ MeV}\,;1^+) \rightarrow\ ^8Be\,(3.03\text{ MeV}\,;2^+)$

The proton beam has been produced by a 5 MV Van der Graaf accelerator with typical current of 1.0 μA. The beams impinged on two different kind of targets, both evaporated on 10 μm Al backings: the first one is a 15 μg/cm^2 LiF target, while the other is a 700 μg/cm^2 LiO_2 [1].

2.1.2 Experimental setup

This section summarizes the experimental setup used by the Atomki group and its characterization as described in references [1, 10].

The pair spectrometer is constituted by 5 plastic telescopes composed of two layers, respectively of dimensions $52 \times 52 \times 1$ mm^3 and $82 \times 86 \times 80$ mm^3. These telescopes are placed in a plane orthogonal to the beam direction, with the thinner layers facing the target, at relative angles of 0°, 60°, 120°, 180°, 270°.
Multi-Wire Proportional Chambers (MWPC) are placed between the target and the telescopes.
Both the telescopes and the MWPCs are placed outside a 1 mm thick Carbon beam pipe that maintains the beam and the target in vacuum. This setup is shown in figure 2.3.

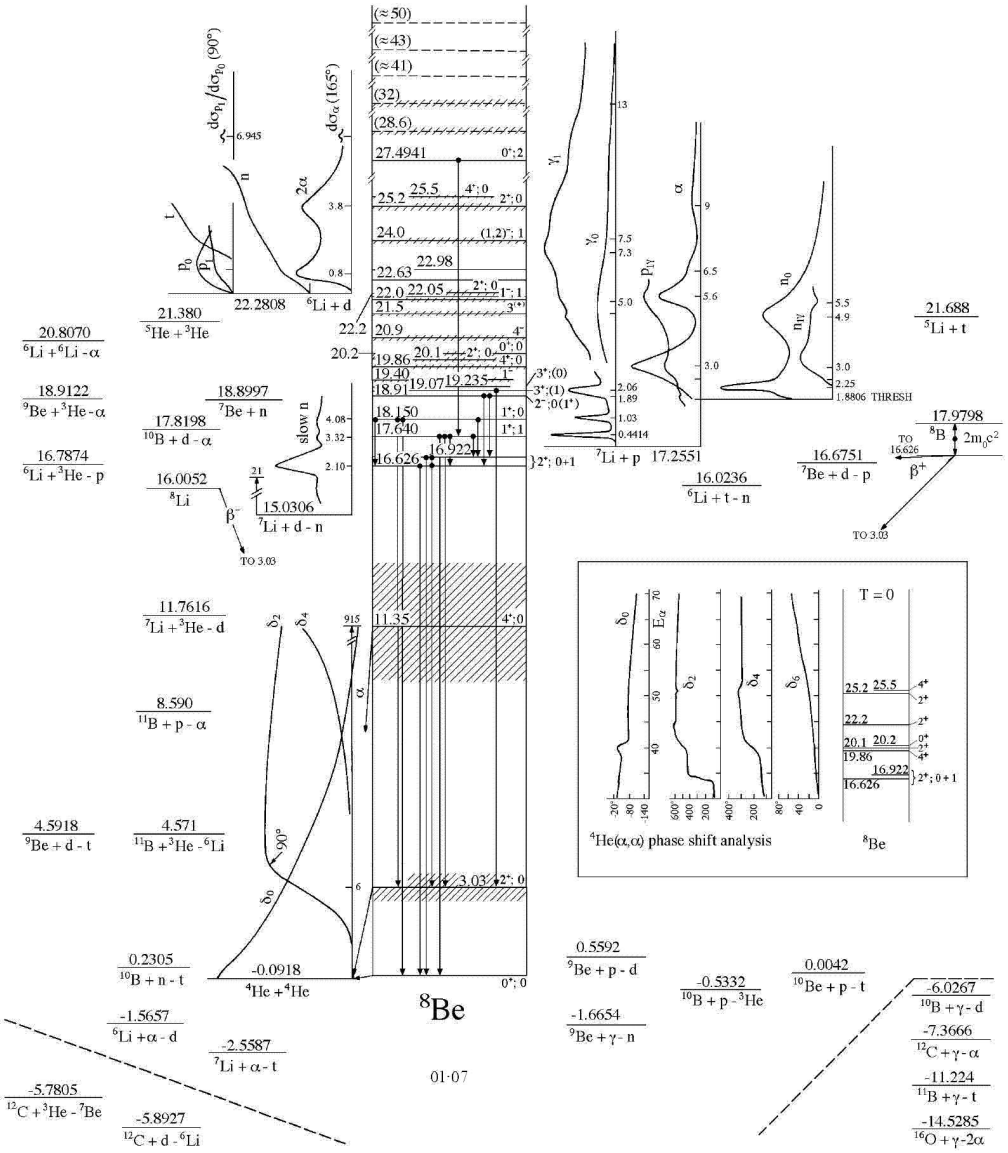

Figure 2.1: Excited states of ^8Be and allowed transitions [20].

The telescopes are used to detect electrons and positrons by correlating the measured energies in the thinner and the thicker layers, respectively ΔE and E. Plastic scintillators combined a sufficient energy resolution with good response times, useful for fast timing coincidence. They are read out by PhotoMoltiplicator Tubes (PMT).

The MWPCs are used to measure the positions of the hits. They are gaseous detectors with good energy and position resolution, high efficiency, and good uni-

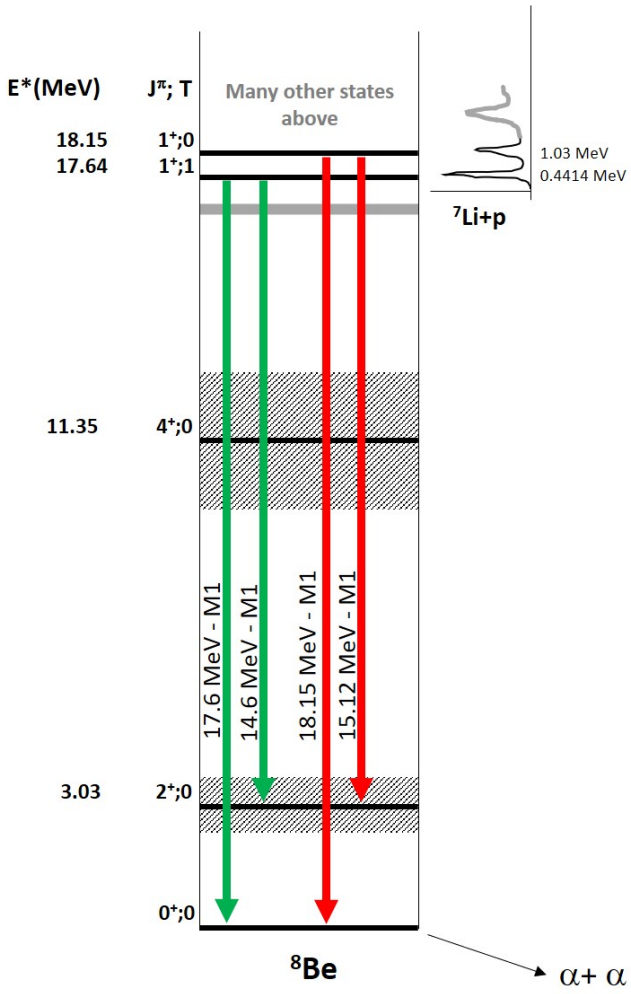

Figure 2.2: Excited states of ^8Be and transitions interesting the Atomki experiment.

formity over the sensitive volume. Moreover, they have been chosen to minimize the material budget close to the target. The anode is an array of parallel 10 µm thick gold-plated wires at a distance of 2 mm from each other. The cathodes are made of thin 100 µm printed boards with 1.25 mm-wide Cu strips. They are placed 3.5 mm away from the anode.
Since the setup is not using a magnetic field, the lepton charge cannot be measured directly. The criterion to select a pair is by fixing an appropriate coincidence windows.

An HPGe detector is used to detect γ-rays at 477.61 keV from the $^7Li\,(p, p'\gamma)$ reaction, in order to monitor the amount of Li in the target and the reaction rate.

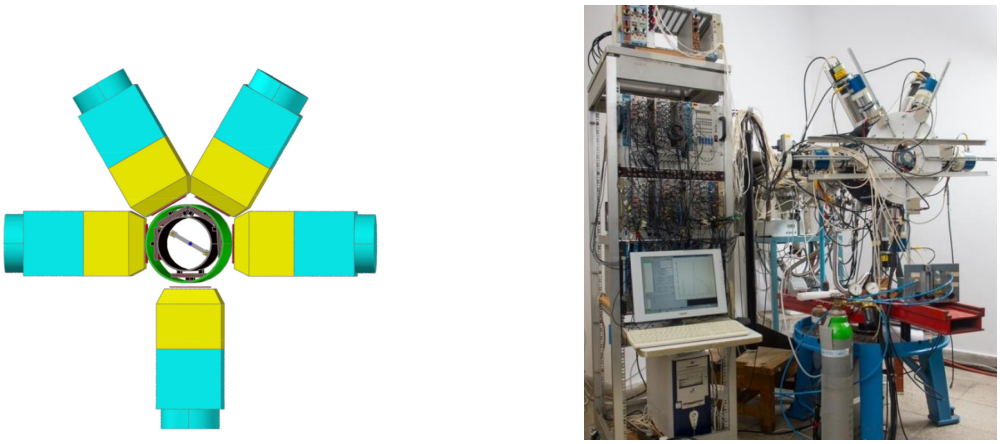

(a) (b)

Figure 2.3: (**a**) Atomki spectrometer representation: the carbon beam pipe is black, the MWPCs are grey, the plastic ΔE and E detector are respectively red and yellow, and the PMT are light-blue. [10] (**b**) Picture of Atomki's experimental setup. [10]

A Monte Carlo simulation of the setup is reported in reference [10] where the GEANT3 simulation code was used to estimate the detector response.
For different transition energies, both electrons and positrons are emitted isotropically, as shown in the appendix section A.1.
Energy loss effects due to the escape of γ radiation created by bremsstrahlung or annihilation will result in a distortion of the spectra. As an example, figure 2.4a shows the response of the setup to high energy pairs 18.15 MeV with respect to lower energy ones 6 MeV.

The Monte Carlo simulations have been used also to perform an efficiency calibration of the spectrometer, studying its response to isotropic uncorrelated pairs as a function of the correlation angle.
Both the electron and the positron are emitted isotropically, and their correlation angle is computed. The resulting angular correlation gives the experimental response curve. This curve, shown in figure 2.4b, has been used as a correction to the experimental curve obtained when measuring correlated pairs. The agreement with the experimental data is good.
This simulation allows to estimate the angular systematic uncertainties as $\Delta\Theta = 6°$.

The energy calibration of the spectrometer has been performed using the Compton edges of a ^{60}Co source at low energies, and the ones of γ transitions from

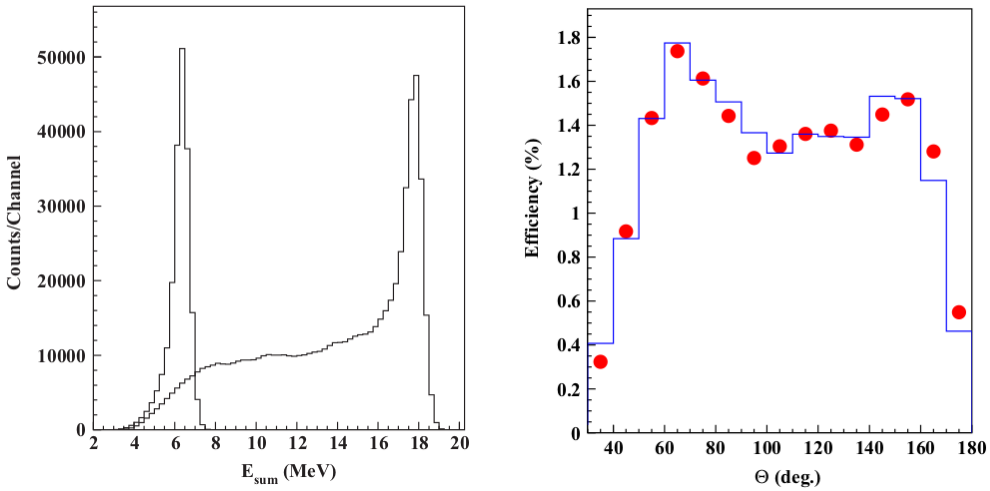

(a) (b)

Figure 2.4: (**a**) Simulated response of the setup when measuring pairs produced in 6 MeV and 18 MeV transitions. [10] (**b**) Response as a function of the correlation angle for isotropic e^+e^- pairs in Monte Carlo simulation (histogram) and experimental data (dots). [10]

proton captures at high energies.
Then, the sum energy spectra have been verified in the $^{16}O\,(6.05\text{ MeV}, 0^-) \rightarrow ^{16}O\,(g.s.)$ transition from the $^{19}F\,(p, \alpha e^+e^-)^{16}\,O$ reaction, and the $^{8}Be\,(17.64\text{ MeV}\,; 1^+) \rightarrow {}^{8}Be\,(g.s.)$ and $^{8}Be\,(17.64\text{ MeV}\,; 1^+) \rightarrow {}^{8}Be\,(3.03\text{ MeV}, 2^+)$ transitions from the $^{7}Li\,(p, e^+e^-)^{8}\,Be$ reaction, shown in figure 2.5.

2.1.3 Experimental results

As seen in section 1.3, the correlation angle distribution is expected show a maximum at 0° and to rapidly decrease at increasing angular values, as seen in figure 1.6. A similar behavior is expected for the invariant mass distribution.
The Monte Carlo simulations that have been compared to the experimental data took into account this distributions and the experimental background measured before and after the experiment, given by γ radiations, external pair creation and multiple lepton scattering.

For the 17.6 MeV $M1$ transition a slight deviation from the simulated angular correlation curve has been observed, but it doesn't present any structure [1]: it has been explained adding an E1 background component originated by non-resonant proton capture. The contribution of the direct proton capture is due to the target thickness: if the energy lost by the proton beam in the target is larger than the

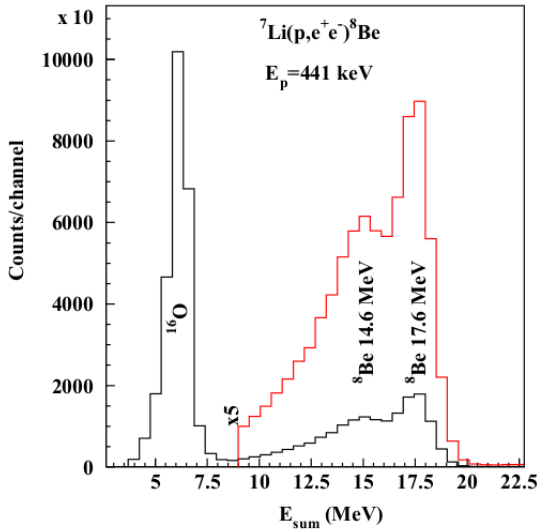

Figure 2.5: Total energy spectrum reconstructed as sum of the energy deposited in the telescopes by the pairs. The red histogram is multiplied by a factor 5 with respect to the black one. [10]

width of the 0.4414 MeV resonance used to populate the 17.6 MeV state in ^8Be, then the capture becomes non-resonant.
As one can notice in figure 2.6, the combined $M1 + 1.4\%E1$ IPCC transitions (dashed line) are in better agreement with the experimental data compared to a pure $M1$ transition (full line).

On the other hand, the angular correlation distribution for the 18.15 MeV $M1$ transition presents a deviation from the simulation that could not be explained by any background component.
The spectra presented were obtained by selecting symmetric pairs, namely the ones satisfying the relation $|y| \leq 0.5$, where $y = (E^- - E^+) / (E^- + E^+)$ and E^- and E^+ are the electron and positron kinetic energies.
By selecting the sum energy in the region around $15 - 18$ MeV a deviation from the simulations appears in the angular correlation distribution in the 140° region, and this deviation becomes even more evident by narrowing the accepted energies around 18 MeV, as shown in figure 2.7.
This excess could not be explained by target's impurities, because the γ spectrum doesn't present peaks above 11 MeV. Moreover, mixing $E0$ components in the simulations doesn't improve the agreement, so neither the $E0$ transition from the 20.2 MeV 0^+ state could explain this excess.

The 18.15 MeV transition has a 8:1 forward-backward γ emission anisotropy,

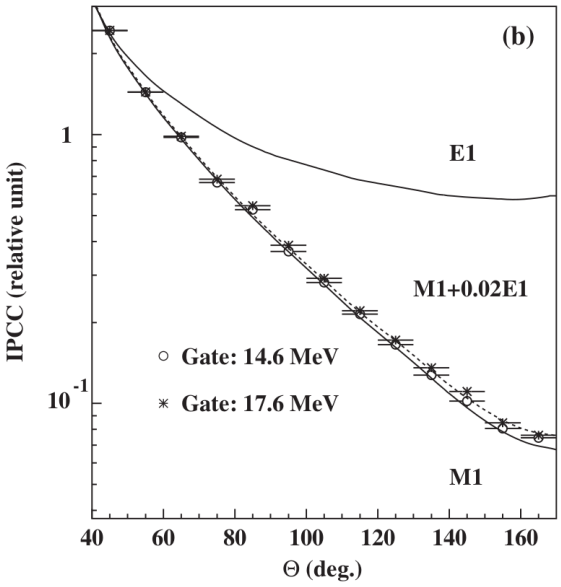

Figure 2.6: Angular pairs correlation in the 17.6 MeV resonance compared with the simulations assuming a pure $M1$ transition (full line) and a mixed $M1 + 1.4\%E1$ transition (dashed curve). [1]

caused by the interference of the $E1$ amplitude given by the non-resonant capture with the two $M1$ amplitudes of the resonances. In order to verify that this anisotropy doesn't affect the angular correlation distribution, several measurement at different beam energies have been performed.
In figure 2.8 it is possible to see that the anomalous excess is present if the proton bombarding energy is near the resonance, but disappears when the bombarding energy leaves the resonance. The results show that the measured deviation from the simulations are in agreement with the resonance shape, but not with the anisotropy shape: indeed, the γ background for proton energies outside the resonance doesn't change with respect to the one for the resonant proton bombarding energy, but no anomalies are observed outside the resonance.

In 2019 the same experiment has been repeated using an improved setup, that will be described in paragraph 2.2.1, basically corroborating the findings presented in this paragraph. [2].

As a conclusion, the authors claimed that, to the best of their knowledge the observed anomaly cannot be explained in terms of conventional nuclear physics models. However, a possible interpretation is proposed in reference [1], namely the hypothetical existence of a new neutral light boson decaying in leptonic pairs.

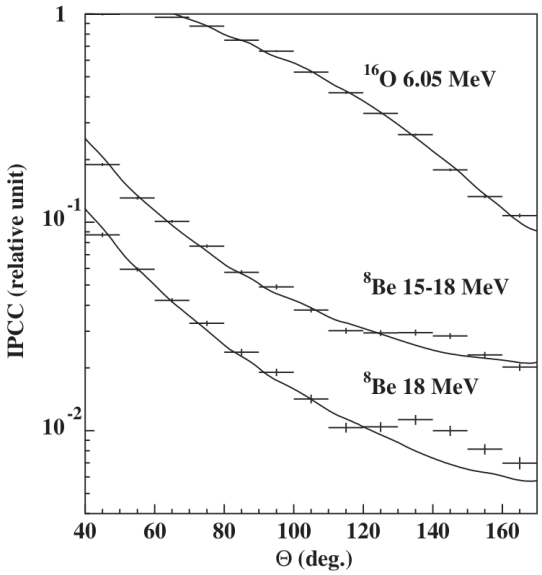

Figure 2.7: Angular correlation distribution simulated (full line) and measured (dots) in the 6.05 MeV $E0$ transition of $^{16}O^*$ (due to $^{19}F\,(p, \alpha e^+e^-)^{16}\,O$ reaction on target contamination) and in the 18.15 MeV $M1$ transition of $^8Be^*$, gating in a region around $15 - 18$ MeV and in another one more narrow near 18 MeV. [1]

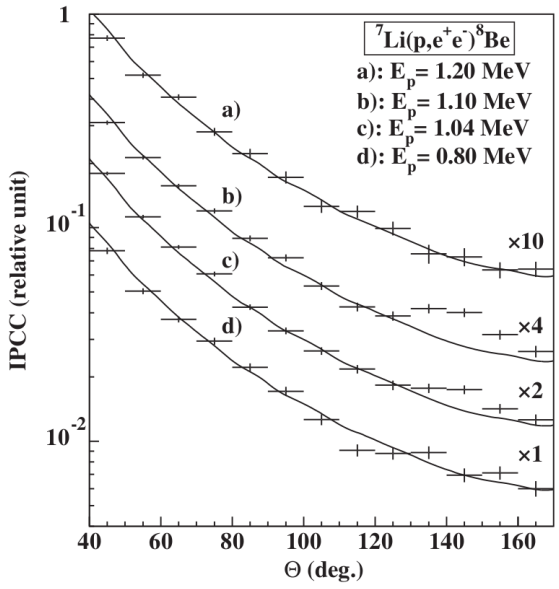

Figure 2.8: Angular correlation distribution simulated (full line) and measured (crosses) in the $^7Li\,(p, e^+e^-)^8\,Be$ reaction for several proton energies. [1]

Results interpretation

The e^+e^- decay of a light neutral boson emitted isotropically from the target has been added to the simulation of the common IPC emission of leptonic pairs.
The simulations have been performed setting several possible values for the boson masses, as shown in figure 2.9. It is possible to notice the good agreement between the experimental data related to symmetric pairs ($|y| \leq 0.5$) and the simulation performed assuming a boson mass of $m_0c^2 = 16.70 \pm 0.35$MeV, which had resulted from the best fit of the invariant mass spectrum. The boson to γ branching ratio best fit value results to be 5×10^{-6}, leading to a boson-decay width $\Gamma_X = 1.2 \times 10^{-5}$eV.
Moreover, according to the calculations, for the asymmetric pairs ($0.5 \leq |y| \leq 1.0$) boson-related effects on the distributions are not expected, indeed in figure 2.9 the experimental data related to these pairs don't deviate from the normal IPC simulated curve.

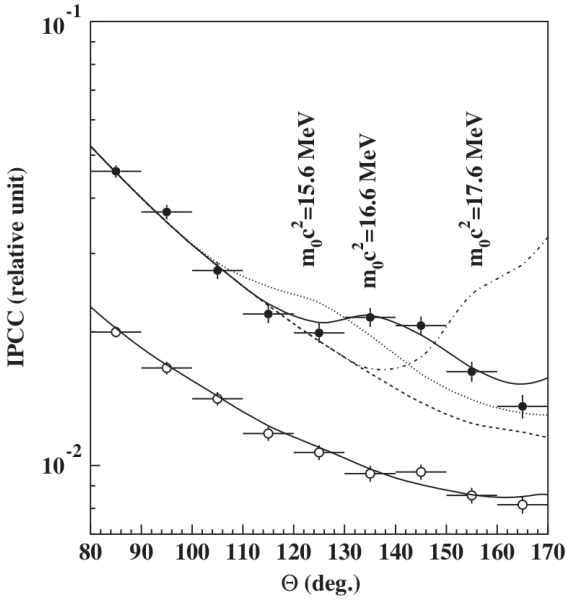

Figure 2.9: Experimental angular correlation measurement with $|y| \leq 0.5$ (full dots) and $0.5 \leq |y| \leq 1.0$ (empty dots), and simulated curves taking into account just normal IPC (grey full line) or adding a boson assuming several possible masses (black full line and dashed lines). [1]

As mentioned in paragraph 2.1.2), the systematic uncertainty on the angular position is evaluated as $\Delta\Theta = 6°$, which in turn is translates to a boson mass systematic uncertainty of 0.5 MeV.
Indeed, the invariant mass distribution has been calculated from the measured

energies and correlation angles as:

$$m_{boson}c^2 = \sqrt{1-y^2}E\sin\frac{\theta}{2} + 2m_e^2\left(1+\frac{1+y^2}{1-y^2}\cos\theta\right) \tag{2.1}$$

where $E = E^+ + E^- + 1.022$ MeV, and y are defined as before.
The final estimation of the boson mass is thus $m_0c^2 = 16.70 \pm 0.35 \pm 0.5$ MeV.

The agreement between the experimental invariant mass distribution and the calculated one assuming a decay of a 1^+ boson with mass 16.6 MeV added to a mixed normal IPC emission is shown in figure 2.10.

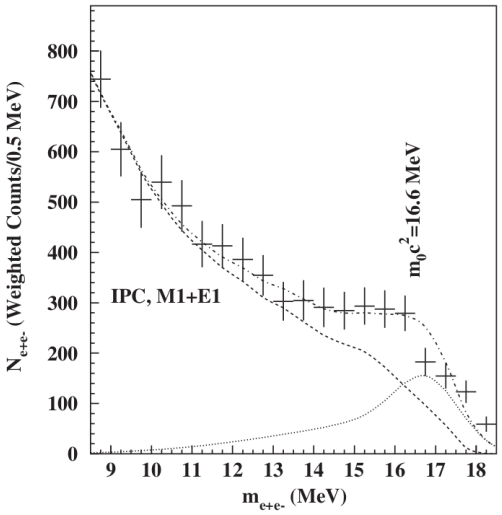

Figure 2.10: Simulated invariant mass distribution assuming a $M1 + 23\%E1$ IPC transition (dashed lines), a decay of a 16.6 MeV boson (dotted line) and the sum of the two previous distributions (dashed-dotted line), compared to the experimental data (crosses). [1]

2.2 $^4He^*$ decay and observed anomaly

In order to confirm the existence of the hypothetical new particle, that from now will be referred to as "X17", the Atomki group looked for its creation and decay in the $^4He\,(21.01\text{ MeV}, 0^-) \rightarrow^4 He\,(g.s.)$ transition, as reported in a recent publication [2].

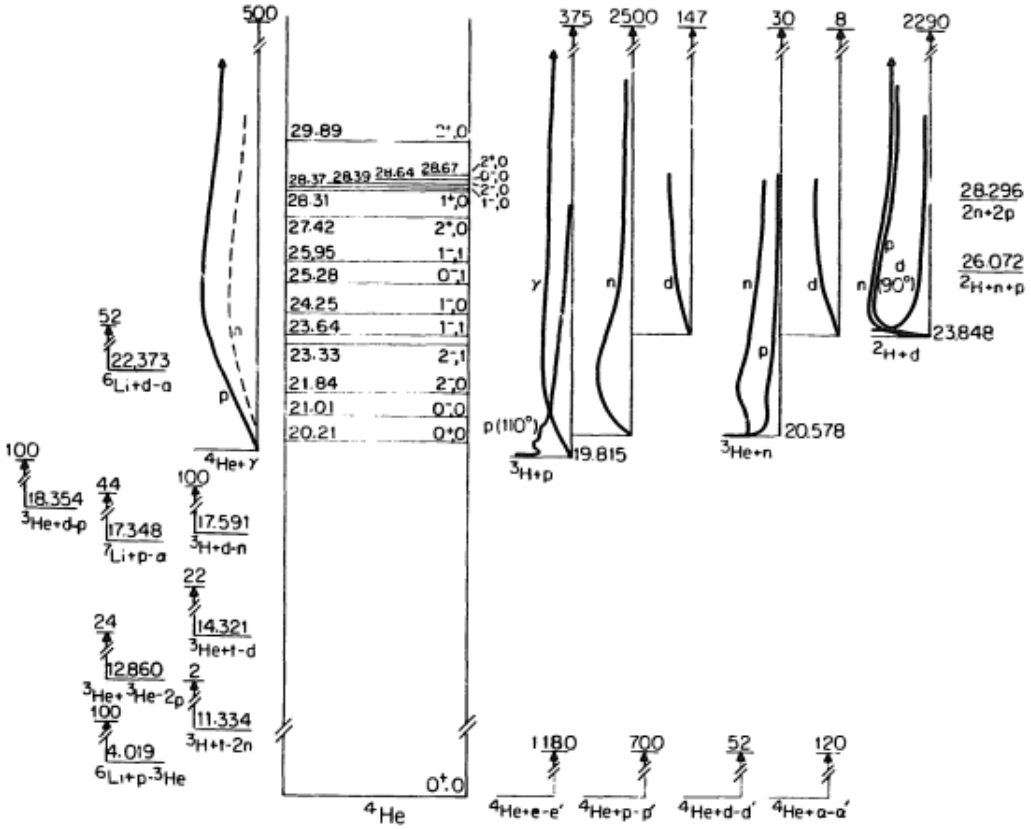

Figure 2.11: Level scheme of ^4He. [21]

2.2.1 Experiment description

The 21.01 MeV 0^- second excited state of ^4He is populated through the $^3H\,(p,\gamma)^4\,He$ reaction at proton bombarding energy $E_p = 900$ keV. This state is wide ($\Gamma = 0.84$ MeV) and it overlaps with the first excited state (0^+, 20.21 MeV, $\Gamma = 0.50$ MeV). The level scheme of ^4He is shown in figure 2.11.
With the bombarding energy used the ^4He is excited at an energy $E_x = 20.49$ MeV, so both the states are populated; however, the pair production rate given by the lower energy transition is less relevant.

A proton beam with a current of 1.0 μA impinged on a ^3H target, that is absorbed in a 3 mg/cm^2 thick Ti layer, that in turn is evaporated on a 0.4 mm thick Mo disc.
The ^3H density is 2.66×10^{20} $atoms/\text{cm}^2$, and in order to prevent its evaporation the disk is cooled down at N_2 temperature.
As for the previous experiment, the experiment was performed at the Atomki

laboratory in Debrecen, exploiting the 5 MV Van der Graaf accelerator.

Spectrometer improvements

The experimental setup is very similar to the one presented in paragraph 2.1.2, but implements some improvements.
First of all, the number of telescopes has been increased from 5 to 6, and they are placed at azimuthal angles of 0°, 60°, 120°, 180°, 240°, 300°. In this way, the solid angle covered increased, and in general the efficiency distribution as function of the correlation angle is modified.
An important improvement regards the hits positions measurement: the MWPCs have been replaced by a double-sided silicon strip detector (DSSD) array. These silicon strips are 3 mm wide and 500 μm thick.

The efficiency calibration has been performed using the same simulation methods explained in the paragraph 2.1.2.

In order to evaluate correctly the background, it has been measured before and after the experiment, and it has been cut applying the same gate used for the in-beam data.
Cosmic rays angular correlation has been determined for pairs with a energy sum 25 MeV $\leq E_{sum} \leq$ 50 MeV, in order to avoid in-beam effects.
On the other hand, subtracting the external pair creation background not related to cosmic rays is a bit more complicated: two sum total energy spectra have been produced for pairs with an angular correlation of 60° and 120°, and since the X17 boson pairs are expected in the 115° region, the first spectrum has been subtracted by the second one in order to enhance the boson effects.
Moreover, also the background given by the $^4He\,(20.21\text{ MeV}, 0^+) \rightarrow^4 He\,(g.s.)$ $E0$ transition has been taken in account.
In figure 2.12a the simulated background components are shown, and the agreement of their sum with the experimental background is evident.

2.2.2 Experimental results

Once the background is rescaled to fit the experimental angular correlation distribution in the region between 40° and 90°, the presence of a peak at 115° becomes evident.
The complete angular distribution fitting function has been estimated by summing a background component, determined experimentally, and a signal one, simulated by GEANT4.
The significance of the peak appears to be 7.2σ. The best fit value of the boson

mass is $m_X c^2 = 16.84 \pm 0.16$ MeV, and the decay width best fit value results to be $\Gamma_X = 3.9 \times 10^{-5}$eV.

The invariant mass distribution, shown in figure 2.12b, has been calculated using the equation 2.1. Even in its distribution a peak around the 17 MeV mass region is clearly visible, and the agreement with the simulation assuming the X17 decay is evident.
The significance of this peak is 7.1σ, and the mass best fit value is $m_X c^2 = 17.00 \pm 0.13$ MeV.
The systematic uncertainties, given by the uncertainties on the target position, is estimated as 0.20 MeV.

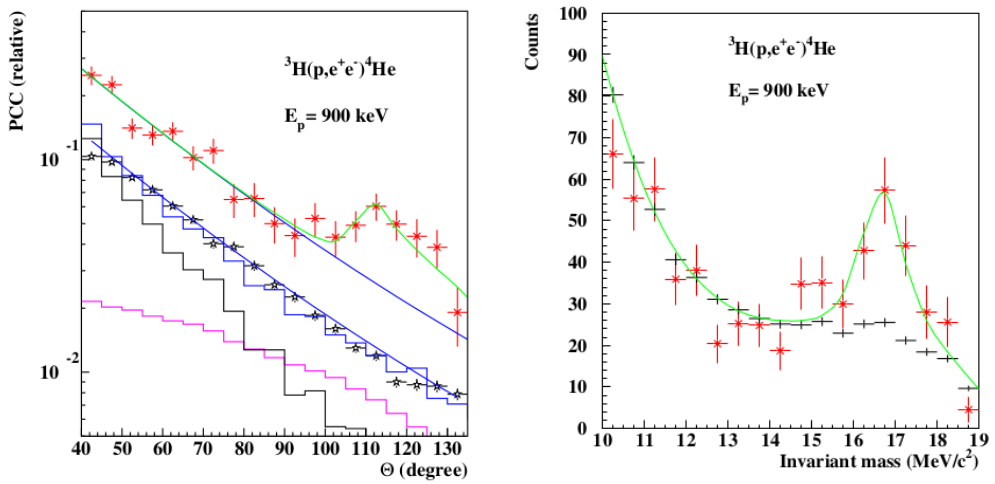

(a) (b)

Figure 2.12: (**a**) Angular pairs correlation in the 20.49 MeV transition and background components (external pair creation, black histogram; pair creation related to the 20.21 MeV transition, magenta histogram) compared with the simulation. [2] (**b**) Invariant mass distribution experimental data (red cross) in the 20.49 MeV transition, compared with the simulated distribution (green line). [2]

The mass values obtained in this experiment and in the previous one are in very good agreement, even if the peaks appearing in the angular correlation distribution are in quite different angular positions because of the different transition energies. The authors of the papers conclude that the new observation is compatible with the previous one.

2.3 Interpretation

The anomalies evidenced in references [1] and [2] and the interpretation proposed, triggered the interest of several research groups that are developing new and dedicated frameworks on this topic.

As already proposed by the Atomki group, the observed anomalies could be explained by the introduction of a light vector boson. The possibility of a fifth fundamental force has been discussed for a long time and this result promoted a renewed interest on the topic.

However, it could be possible also that the anomaly is due to yet-unidentified nuclear effects, and it would be explained in a more conventional nuclear physics framework, by improving the nuclear physics modeling of IPC, studying its anisotropy and multipoles interferences.

In this section both the interpretations will be presented. However, with the current knowledge none of them can be ruled out, thus further analysis and new investigations are needed.

2.3.1 Interpretations within nuclear physics framework

X. Zhang and G. A. Miller examined a possible explanation of the ^8Be anomaly in a conventional nuclear physics framework [18]: the work focused on the improvement of the nuclear physics modeling of the considered reaction by studying the pair emission anisotropy and the interference between multipoles.
The authors claimed that the physics modeling of the reaction used in the simulations presented in paragraph 2.1.3 is incomplete, indeed one should take into account a preferential direction set up by the initial kinematics and the similar weight of the $E1$ and $M1$ multipolarities.

In the work, an effective field theory model is developed, calibrated to the photon production data and eventually used to predict pair production cross section.

The effective field theory (EFT) model

A first step in modeling the reaction is defining the allowed phase space region. Let's call $\mathbf{p}$, $\mathbf{p}_+$ and $\mathbf{p}_-$ the relative $p - ^7 Li$ momentum and the positron and electron momenta, respectively. Once $\mathbf{p}$ is fixed, the only degree of freedom in photon production is θ, so the degrees of freedom in the pair emission are θ, ϕ, θ_{+-} and the electron energy E_-. So the total pair production cross section is:

$$\sigma_{e^+e^-} = \frac{M\alpha}{p16\pi^3}\int dE_- d\cos\theta_{+-} d\cos\theta d\cos\phi \frac{\mathbf{p}_+\mathbf{p}_-}{8}\sum_{spins}|\mathcal{M}_{e^+e^-}|^2 \tag{2.2}$$

and by computing $d\sigma/dM_{+-}$ it results that the allowed phase space is

$$4m_e^2 \leq M_{+-}^2 \leq \omega^2\left(1-\cos\theta_{+-}\right)/2 \tag{2.3}$$

as shown in figure 2.13.

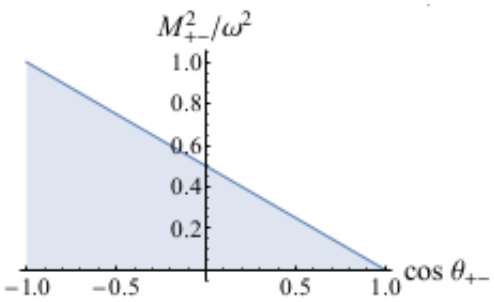

Figure 2.13: Allowed phase space region for the e^+e^- pair production. [18]

In order to model the reaction another important element is the electromagnetic matrix element, containing different components $U_{\lambda SL}$ depending on the virtual photon multipolarity λ and on the initial state total spin and angular momentum S and L.
Because of parity conservation, an E1 transition is between the s-wave ($L = 0$) $p-^7Li$ scattering state and the ^8Be ground state, and the only allowed value of S is 0, while for the $M1$ transition $L = 1$ and $S = 1$ or $S = 2$. Considering also the $E2$ components ($L = 1$,$S = 1, 2$), five amplitudes need to be taken into account.
The transitions happen in short distances ($\lesssim$ 5fm), so the reaction could be studied in an EFT framework, using interaction Lagrangians satisfying rotational, Galileian, parity and time reversal invariance.
For the assumptions made until this point, the Lagrangian components considered in the reaction modeling are $\mathcal{L}_0$ (free Lagrangian), $\mathcal{L}_p$ (p-wave interaction between the $p-\ ^7Li$ system and the resonances), $\mathcal{L}_{M_1}$, $\mathcal{L}_{E_1}$ and $\mathcal{L}_{E_2}$ (containing the $M1$, $E1$ and $E2$ transitions).

To correctly calibrate the model, it has been fitted against the photon production data, in particular against the S-factor (i.e., a parameter proportional to $E\cdot\sigma$) and two parameters, a_1 and a_2, defined as functions of the electromagnetic matrix element components $U_{\lambda SL}$.

Once the photon production has been modeled, it is necessary to couple the electromagnetic leptonic and nuclear currents in order to model the pair production. The pair emission anisotropy, due mostly to the $E1-M1$ interference, is not negligible, and it has been included in the model. For this reason, in future experiment, it must be included in analyzing the nuclear background.

Once the nuclear physics modeling is complete it is possible to verify whether the anomaly observed by Atomki group is due to θ modulation.
The differential cross section $d\sigma/dM_{+-}d\cos\theta$ predicted by this model and expressed as a function of M_{+-} is compared to the corresponding experimental Monte Carlo simulation (described in paragraph 2.1.3), as shown in figure 2.14a. Analogously, as shown in figure 2.14b, this comparison has been done even for $d\sigma/d\theta_{+-}d\cos\theta$.
The agreement between this model prediction and the MC simulation is much better in the M_{+-} distribution than in the θ_{+-} one, probably because the detector efficiency variation is large in the considered θ_{+-} range, but negligible in the M_{+-} one.
However, it is clear that the improved model is not enough to explain the anomaly, so a new term has been added.

Addition of a Form Factor

Zhang and Miller showed how introducing a form factor to the resonance electromagnetic coupling of the $M1$ transition could explain the observed anomaly.
The form factor has been defined using a polynomial parametrization as $f\left(M_{+-}^2\right) \equiv 1 + f_1 r + f_2 r^2 + f_3 r^3$, with $r \equiv M_{+-}^2/\Lambda^2$, where $\Lambda = 20$ MeV.
The form factor parameters have been extracted by fitting the ratio

$$\frac{d\sigma/dM_{+-}d\cos\theta|_{\theta=90°,withFF}}{\mathcal{N}_1 d\sigma/dM_{+-}|_{withoutFF}} \tag{2.4}$$

where $\mathcal{N}_1$ is a normalization factor, against the ratio $data/MCsimulation$: in this way the effect of missing detector efficiency, seen in figure 2.14 in the disagreement between the improved model prediction and the MC simulations, is minimized, assuming that $d\sigma/dM_{+-}$ calculated without form factor should be the closest to MC simulation.
Given the obtained form factor parameters, the corresponding θ_{+-} distribution is calculated.
In figure 2.15 it is possible to observe in both the distributions that adding a form factor allows a qualitative fit of the invariant mass distribution, while the angular correlation shape is not reproduced.

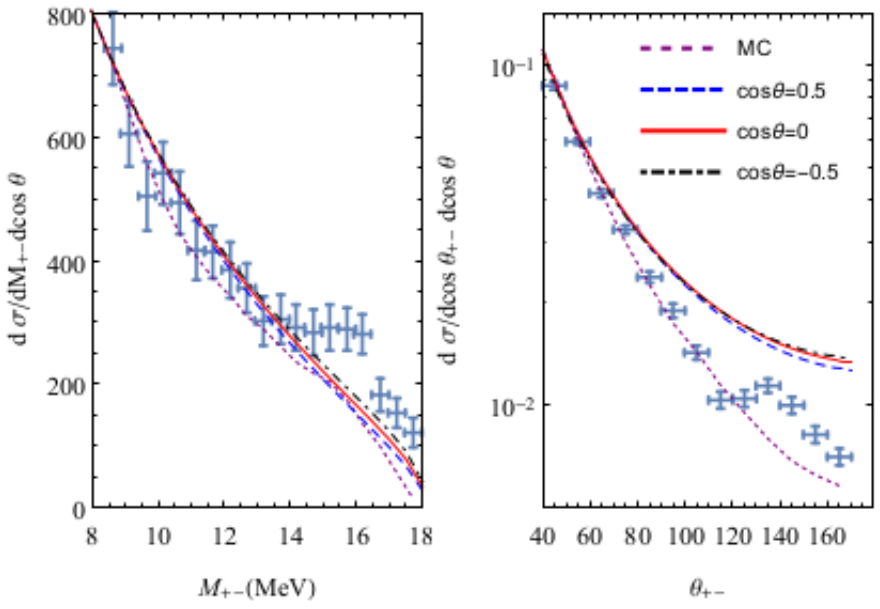

(a) (b)

Figure 2.14: (**a**) Differential cross section against M_{+-} predicted by the model at different values of $\cos\theta$ (blue, red and black curves) compared with the MC simulation (purple line) presented in 2.1.3 [1] and the experimental data (crosses). [18] (**b**) Differential cross section against θ_{+-} predicted by the model at different values of $\cos\theta$ (blue, red and black curves) compared with the MC simulation (purple line) presented in 2.1.3 [1] and the experimental data (crosses). [18]

Summarizing, the nuclear physics modeling for leptonic pair production has been improved including the interferences between $E1$, $E2$ and $M1$ multipoles, taking into account the angular dependencies and anisotropies, and introducing constraints given by the photon production kinematics.
Both the interference and the anisotropy are currently neglected in the analysis, but will be necessary to improve the constraints on parameters related to an hypothetical new physics.
Moreover, it has been found that introducing a form factor to the $M1$ transition could explain the shape of the experimental data in the M_{+-} distribution, but not in the correlation angle θ_{+-} one.
Therefore this work is not conclusive, and different hypothesis could not be ruled out.

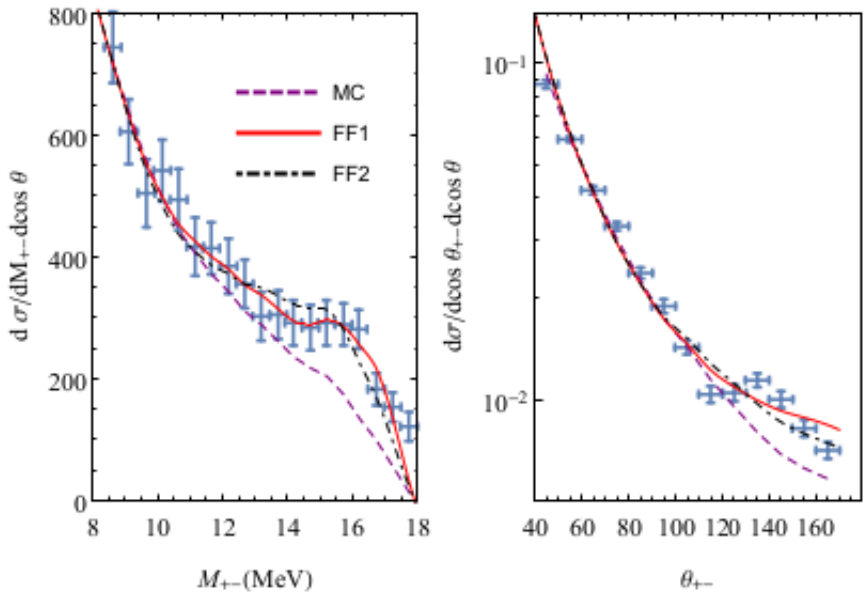

Figure 2.15: Cross section distributions against M_{+-} and θ_{+-} predicted by the model with the addition of a form factor compared with the MC simulations and the experimental data. [18]

2.3.2 A fifth fundamental force?

A different approach is developed by J.L. Feng and collaborators that investigate the hypothesis of the existence of a so-called protophobic gauge boson [16, 17].
In particular, studying the constraint imposed by the observed pair emission, they defined some characteristics that must describe this boson.

^8Be experiment constraints

A priori the X17 boson could be a scalar, pseudoscalar, vector, axial or spin-2 particle.
The scalar possibility is excluded by parity conservation: indeed, the transition would be a $1^+ \to 0^+0^+$ transition, and the angular momentum conservation would require $L = 1$, but parity conservation would require $1 = (-1)^L$, so $L = 2n$.
A pseudoscalar particle is allowed, but constrained by experiments: for the expected mass, all coupling values in a very wide region are excluded.

Thus, Feng's work focuses on the gauge vector boson possibility.
It has been considered a massive spin-1 abelian gauge boson X that couples non-chirally to Standard Model fermions with charges ϵ_f.
The Lagrangian will be:

$$\mathcal{L} = -\frac{1}{4}X_{\mu\nu}X^{\mu\nu} + \frac{1}{2}m_X^2 X_\mu X^\mu - X_\mu J^\mu \tag{2.5}$$

where $J_\mu = e\epsilon_p \overline{p}\gamma_\mu p + e\epsilon_n \overline{n}\gamma_\mu n$, with $\epsilon_p = 2\epsilon_u + \epsilon_d$ and $\epsilon_n = \epsilon_u + 2\epsilon_d$, considering the quarks composing protons and neutrons.

First at all, it is necessary to determine the charges values to fit the signal observed in the ^8Be decay.
The effective interaction Lagrangian is

$$\mathcal{L}_{int} = \frac{1}{\Lambda}\epsilon^{\mu\nu\alpha\beta}\left(\partial_\mu^8 Be_\nu^* - \partial_\nu^8 Be_\mu^*\right) X_{\alpha\beta}^8 Be \tag{2.6}$$

(where Λ is a scaling factor) and computing the S-matrix element $\langle {}^8BeX|\mathcal{L}_{int}|{}^8Be^*\rangle$ describing the gauge boson creation, the decay width results

$$\Gamma\left({}^8Be^* \to^8 BeX\right) = \frac{(e/2)^2\left(\epsilon_p + \epsilon_n\right)^2}{3\pi\Lambda^2}|\mathcal{M}|^2|\vec{p_X}|^3 \tag{2.7}$$

with $\mathcal{M} = \langle {}^8BeX|(\overline{p}\gamma_\mu p + e\epsilon_n\overline{n}\gamma_\mu n)|{}^8Be^*\rangle$.
Comparing this equation with the experimental decay width $\Gamma_X = 1.2 \times 10^{-5}$eV (2.1.3), the charges values need to satisfy $|\epsilon_p + \epsilon_n| \sim 0.011$ in order to make the two values agree, that correspond to $|\epsilon_u + \epsilon_d| = 3.7 \times 10^{-3}$.

Although it is produced through hadronic couplings, it can only decay to e^+e^-, $\nu\overline{\nu}$ or $\gamma\gamma\gamma$. The decay in neutrinos and photons are assumed to be negligible. Considering the e^+e^- decay width

$$\Gamma\left(X \to e^+e^-\right) = \epsilon_e^2\alpha\frac{m_X^2 + 2m_e^2}{3m_X}\sqrt{1 - 4m_e^2/m_X^2} \tag{2.8}$$

and considering that the X boson and the $^8Be^*$ nucleus velocities in the lab frame are respectively $v_X \sim 0.35c$ and $v_{Be} \sim 0.017c$, the decay length results to be $L \sim \epsilon_e^{-2} \cdot 1.8 \times 10^{-12}$ m. Imposing that the boson decays promptly inside the target, in order to avoid angular distribution distortions, it results $|\epsilon_e| \gtrsim 1.3\times10^{-4}$.

Other experimental constraints

Several experimental constraints on a possible X boson couplings values with such a mass have been given other than the ones given by Atomki experiment.

Let's begin from hadronic couplings bounds, shown in figure 2.16a.

The NA48/2 experiment put a bound on $\pi^0 \to X\gamma$ decay width that results to be, for a general gauge boson, $|2\epsilon_u + \epsilon_d| < \epsilon_{max} = 8 \times 10^{-4}$. This bound excludes the possibility to explain the ^8Be anomaly with the introduction of a dark photon, because its coupling charge would be $\epsilon \sim 0.011$, that would be bigger than ϵ_{max}. Another boundary condition can be obtained by the Yukawa potentials induced by the boson in neutron-nucleus scattering: from the study of the scattering $n - Pb$ it appears that $|\epsilon_n| < 2.5 \times 10^{-2}$ is required.

Several experiments provide a boundary for the leptonic coupling, shown in figure 2.16b.
The anomalous magnetic moment of the electron $(g-2)_e$ constrains $|\epsilon_e| < 1.4 \times 10^{-3}$.
The KLOE-2 experiment looks for e^+e^- emission following the reaction $e^+e^- \to \gamma X$, and it obtains $|\epsilon_e| < 2 \times 10^{-3}$.
Electron beam dump experiments put bounds searching for the X boson radiated from electrons scattering on nuclei, and excluded ϵ_e values in the region between 10^{-8} and 10^{-4}.
Finally, SLAC experiment E141 requires $|\epsilon_e| > 2 \times 10^{-4}$.
Other experiments gives less stringent bounds, as CHARM experiment at CERN.

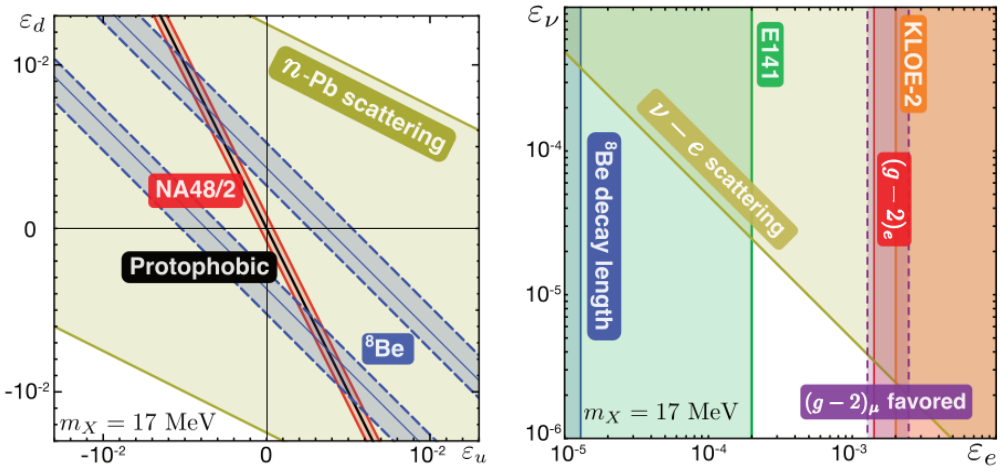

(a) (b)

Figure 2.16: (**a**) Hadronic coupling bounds given by several experiments: values allowed by each experiment stand in the shaded region. [16] (**b**) Leptonic coupling bounds: shaded regions contain the forbidden values. [16]

Given those considerations and experimental constraints, the theoretical model has been developed in a extreme protophobic limit (i.e. $\epsilon_p = 0$). A particle with mass $m_X \approx 17$ MeV in this framework must satisfy the conditions $|\epsilon_n| < 2.5 \times 10^{-2}$

and $2\times10^{-4} < |\epsilon_e| < 1.4\times10^{-3}$, and combining them with first-generation charges it results

$$\epsilon_u = -\frac{1}{3}\epsilon_n \approx \pm 3.7 \times 10^{-3} \tag{2.9}$$

$$\epsilon_d = \frac{2}{3}\epsilon_n \approx \pm 7.4 \times 10^{-3} \tag{2.10}$$

$$2 \times 10^{-4} \lesssim |\epsilon_e| \lesssim 1.4 \times 10^{-3} \tag{2.11}$$

For a better characterization of the phenomenon further data are needed. In particular, a possible approach could be searching for other nuclei that decay with a similar behavior.
Other possibilities to gather new information are the re-analysis of high-energy experiments data sets, the independent measurement of the same phenomenons, and other planned experiments.
Some examples are represented by experiments like: DarkLight [22], HPS [23], LHCb [24], MESA [25], Mu3e [26], VEPP-3 [27], SeaQuest [28] and SHiP [29] that aim at providing new constraints in yet unexplored region of the parameter space (m_X, ϵ_e). In figure 2.17 the regions forbidden by the current constraints are represented by the gray area, while the regions that will be investigated by the future experiments are the colored ones.

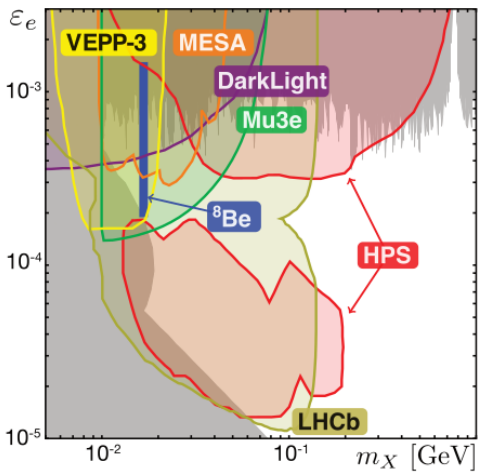

Figure 2.17: Regions in the (m_X, ϵ_e) space excluded by the current constraints (gray) and regions that will be explored in the future experiments (colored regions). [16]

2.3.3 Conclusions and future investigations

The Atomki results proposed in recent literature [1, 2] could potentially have a great impact because of the possible existence of a new light neutral boson.
Different interpretations have been given to explain the anomaly observed. Feng studied more deeply the protophobic boson hypotesis, developing a theoretical framework describing a new interaction mediated by this new particle and constraining the coupling parameters. On the other hand Zhang and Miller proposed an improvement of the nuclear physics modeling of pair emission by including the interference between multipoles and the constraints put in the photon production. Neither of these two hypothesis could be ruled out with the actual knowledge, so new measurement and further investigation are needed.
As previously mentioned, a possible approach for extending the knowledge and understanding of the phenomenon is searching for a similar behavior in other nuclei, for example in ^{12}C as proposed by Feng [30].

It is worth mentioning that, very recently, other theoretical efforts have been put in trying to develop other models. Among those, the work by Viviani and collaborators presents a Chiral Effective Field theory approach including both electromagnetic contribution as well as the nuclear strong-interaction dynamics [31]. The authors conclude with precise angular distribution predictions for different possible features of the X17 particle in the case of ^4He, to be compared with new experimental results. Other ideas have been suggested by Koch [32] that investigates the possible competition of the X17 boson production with a double γ-ray emission. The computation is carried out for the ^8Be case. Despite a fair agreement in the invariant mass reproduction, the computed cross sections are not compatible with the measured ones.

From the experimental point of view, an independent measurement of the observed anomaly is needed. This thesis work focuses on the development of a setup dedicated to the detailed study of the 8Be case. Some critical aspects of the earlier experiments have been analyzed:

- unambiguous electron-positron discrimination is not possible in the Atomki setup;
- energy and angular resolution can be improved;
- background should be minimized and well characterized;
- target purity and stability should be carefully controlled.

The first hypothesis for the setup is a pair spectrometer similar to the one used in the previous experiments [2, 10].

The target is surrounded by plastic $\Delta E - E$ telescopes used both for the energy measurement and the position reconstruction. All the detectors are placed inside a vacuum chamber in order to minimize the background by reducing the amount of material close to the target.
The telescopes will be readout by Silicon PhotoMultipliers (SiPMs).
This pair spectrometer will be described in detail in chapter 3.

The proposed setup does not allow to solve the electron-positron discrimination issue. The only possibility to reach this goal is to introduce a magnetic field that bends the electron and positron trajectories in opposite directions. However, the introduction of a magnetic field carries some issues on the correlation angle estimation and requires the implementation of a tracking detector. The development of such a complex device goes beyond the scope of this thesis work but it is worth mentioning that a Time Projection Chamber coupled to an electromagnetic calorimeter in a magnetic field could be optimal to study the $^{8}Be^{*}$ as well as the $^{12}C^{*}$ case or other cases of interest. The design of the calorimeter described in the following chapters already takes into account the possible coupling of the device with a gaseous detector in a magnetic field.

3

Design of a new setup for e^+e^- pairs spectroscopy

The Atomki results and the related interpretations have potentially a great impact, since they could lead to the introduction of a new vector boson mediating an unknown fundamental force, possibly related to the dark sector searches.
These results triggered a renewed interest in the spectroscopy of light ions by Internal Pair Creation. At this purpose, a new experimental setup is being developed at the INFN Legnaro National Laboratories (Legnaro, Padova, Italy). The first goal is to provide an independent replica of the Hungarian experiment.
The current layout is constituted by an array of $\Delta E - E$ organic scintillator telescopes, gathered in groups of four, whose dimensions have been optimized with the aim of improving the angular resolution. The telescopes are read out by Silicon PhotoMultipliers (SiPMs), allowing the future capability of coupling to a magnetic field. The full detector will be placed inside a vacuum scattering chamber, in order to minimize the material budget between the target and the detectors. The first two layers of the telescopes, composed by two layers of thin of orthogonal bars, will be exploited for the particles tracking. The same layer will also provide the ΔE deposited energy information for particle identification. The bars are read out by an array of SiPMs, for which an innovative readout scheme is proposed.

In this chapter the description of the simulation work related to the proposed setup will be reported.

3.1 Interaction of electrons and photons with matter

This thesis work focuses on the detection of electrons, positrons and gamma-rays. Their interaction processes with matter depend on the type of radiation, its energy and the type of detection medium. The relevant features of the different processes are summarized in the following paragraphs.

3.1.1 Electrons and positrons interactions

The interaction of electrons and positrons is heavily dependent on the particle's energy. At low energies (i.e. $E \lesssim 100$ MeV in organic materials) the dominant mechanism is ionization, though for $E \lesssim 10$ MeV there is also a small contribution of Møller scattering (for e^-), Bhabha scattering and annihilation (for e^+). At energies higher than 100 MeV (in organic materials) the dominant interaction is Bremsstrahlung, although a not negligible contribution of the ionization still remains. The following ones are of particular interest for the present work.

Ionization: if the incoming electron gives enough energy to an atom, it could eject an atomic electron, ionizing the atom.
The energy of the emitted electron depends on the incoming electron energy and on the binding energy. If the emitted electron has enough energy it could eject other atomic electrons. [33].

Bremsstrahlung: it's the emission of electromagnetic radiation due to the acceleration of charged particles inside the matter; each charged particle emits this kind of radiation if it's accelerated or decelerated inside a material, with an intensity inversely proportional to its invariant mass.
Considering an electron accelerated from rest with a potential V, the maximum energy that could be emitted by Bremsstrahlung is $E_{brem} = eV$, so there will be a threshold wavelength $\lambda_{min} = \frac{hc}{eV}$ of the emitted photons [33].

Annihilation: in this process an incoming positron annihilates with an electron and creates at least two photons with 511 keV energy each, emitted back to back because of the energy and momentum conservation.
The cross section of this process increases at decreasing energies of the incoming particles, but it is not very high also at low energies. Other particles besides the photons could be produced if the invariant mass of the incoming particles allows it.

Because of their very low masses, electrons and positrons reach velocities close to the speed of light even at low energies ($\beta = 0.86c$ at 0.5 MeV), so relativistic effects should be taken into account. Annihilation is relevant for almost stopped

positrons, ionization is almost constant with energy, while Bremsstrahlung increases rapidly with the particle's energy. The two latter effects are the dominant ones.

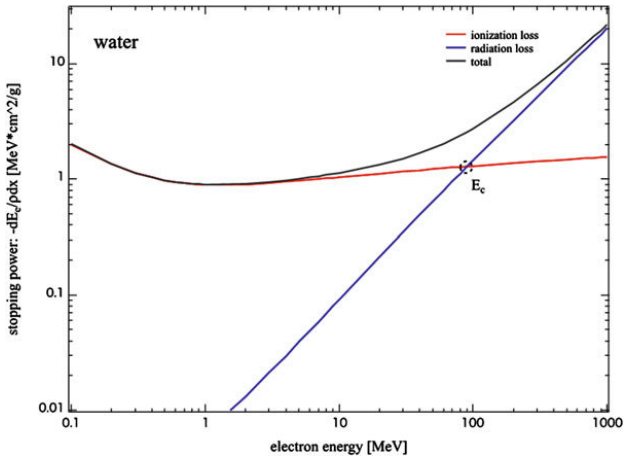

Figure 3.1: Dominant interactions in water as a function of the electron energy. [34]

Therefore, the *stopping power* computation will include a contribution related to collisions, due to ionization, and one related to radiation, due to Bremsstrahlung. The two components, for electrons of energy E and velocity v, are given by:

$$\left[-\frac{dE}{dx}\right]_{coll} \approx \frac{2\pi Z e^4 \rho}{m_e v^2}\left[\ln\left(\frac{m_e v^2 E}{2I^2\left(1-\beta^2\right)}\right) - \ln 2\left(2\sqrt{1-\beta^2}-1+\beta^2\right) + \left(1-\beta^2\right) + \frac{1}{8}\left(1-\sqrt{1-\beta^2}\right)^2\right] \tag{3.1}$$

$$\left[-\frac{dE}{dx}\right]_{rad} \approx \frac{Z\left(Z+1\right)e^4 \rho E}{137 m_e^2 c^4}\left[4\ln\left(\frac{2E}{m_e c^2}-\frac{4}{3}\right)\right] \tag{3.2}$$

where Z is the atomic number of the material, ρ is its density and I its ionization potential.
The ionization component includes other second order contributions if the incoming particle is a positron, that could be neglected.

As shown in figure 3.1, the energy loss due to collisions is proportional to $\ln E$, while the one related to radiation is proportional to E. The point at which Bremsstrahlung starts dominating over ionization is called *critical energy*.
A simplified useful formula to estimate the ratio between the two components is

$$\frac{S_{rad}}{S_{coll}} \approx \frac{\left(Z+1.2\right)E}{800} \tag{3.3}$$

and the critical energy is reached at

$$E_c \approx \frac{800}{Z + 1.2} \text{ MeV} \tag{3.4}$$

It is worth noticing that in the energy region of interest for the experiment, namely the 1−20 MeV range, the Bremsstrahlung process is suppressed, but not negligible.

The positrons cross sections are slightly different because of the abundance of electrons they could encounter in their track and the annihilation process; although, this process has low probability at high energies, so in a first approximation it would interest the positrons just once they released almost all their energy via ionization and bremsstrahlung.

3.1.2 Photon interactions

The behavior of photons inside matter is completely different from the one of charged particles. The absence of a charge makes the inelastic collisions with atomic electrons impossible.
For the electromagnetic radiation, the most important processes are: photoelectric effect, Compton scattering and pair production. Their main features are summarized in the following:

photoelectric effect: the photon is absorbed by an inner shell electron of an atom, transferring to the electron all of its energy.
The electron is then ejected from the atom with kinetic energy $E_{e^-} = E_\gamma - B$, where B is the binding energy of the shell; thus, since the binding energy of the shell is fixed, a discrete peak (*photopeak*) in the measured energy distribution can be expected.
This process is more probable for low energy photons, high atomic number of the material and high density. The probability of photoelectric absorption of gamma-rays is proportional to $Z^{4.5}/E^3$.

Compton scattering: a photon is absorbed by a weakly bound outer shell electron, with a negligible binding energy; a new photon with lower energy and different direction is produced. This process could be effectively considered as a photon-electron elastic scattering.
This process is more probable for intermediate and high photon energies, and for low atomic number of the material.

pair production: it is the decay of the photon in a particle and its antiparticle; this could happen only if the photon has an energy at least equal to the sum of the two particles masses in their rest frame.

Because of the momentum conservation it could happen only if the photon is close to another particle to interact with, so only inside a material.
The threshold energy to produce, in example, e^+e^- pairs, is

$$E_{\gamma,min} = 2m_ec^2 + \frac{2m_e^2c^2}{m_{nucleus}} = 2m_ec^2\left[1 + \frac{m_e}{m_{nucleus}}\right] \tag{3.5}$$

and since $m_{nucleus} >> m_e$ the threshold is $E_{\gamma,min} \approx 2m_ec^2$ [33].
The cross section of this process is proportional to Z^2 and increases with the photon energy.

A summary of the interactions probabilities is shown in the figure 3.2.

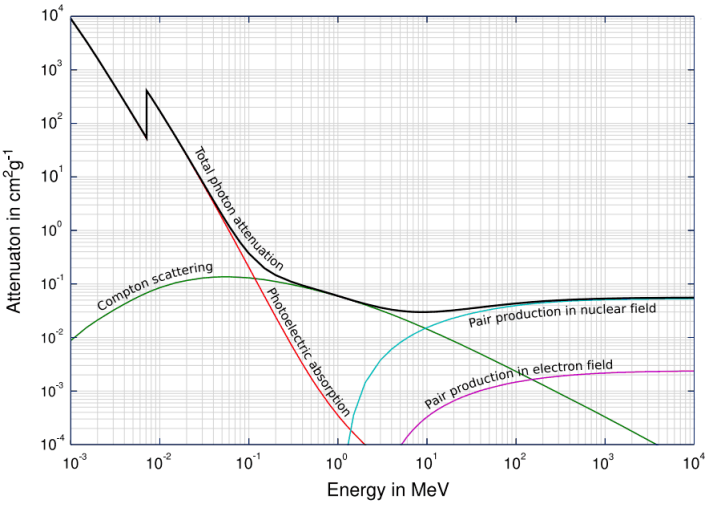

Figure 3.2: Probabilities of the different types of photon interaction with matter in function of the photon energy. [35]

Plastic scintillators will be used in the experiment. Few MeV gamma-rays will be used for calibration exploiting the Compton scattering process. Moreover, the main background during the experiments is expected to be due to gamma radiation in the same energy region. Therefore, the Compton effect is the most probable interaction mechanism to be taken into account and a more detailed description of the process is required.
From basic relativistic kinematics it is possible to predict the energy of the scattered gamma ray E'_γ as a function of the deflection angle θ, the mass of the electron m_e and the energy of the incoming gamma ray E_γ:

$$E'_\gamma = \frac{E_\gamma}{1 + \frac{E_\gamma}{m_ec^2}(1 - \cos\theta)} \tag{3.6}$$

and consequently, the energy of the emitted electron is:

$$E_{e^-} = E_\gamma - \frac{E_\gamma}{1 + \frac{E_\gamma}{m_{e^-}}(1 - \cos\theta)} \tag{3.7}$$

The maximum electron energy achievable, that is the energy obtained with $\theta = 180°$, defines the so called *Compton edge*.

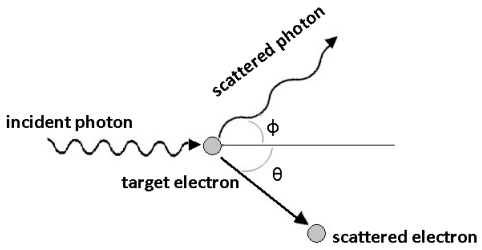

Figure 3.3: Graphic representation of the Compton scattering. [36]

Using tree level quantum electrodynamics it is possible to compute the differential cross section of the process, giving the famous Klein-Nishina formula:

$$\frac{\mathrm{d}\sigma}{\mathrm{d}\Omega} = \frac{r_e^2}{2}\left(\frac{E'_\gamma}{E_\gamma}\right)^2\left(\frac{E'_\gamma}{E_\gamma} + \frac{E_\gamma}{E'_\gamma} - \sin^2\theta\right) \tag{3.8}$$

where r_e is the classical electron radius.
From this formula is clear that the forward emission of the new photon is the most probable.

3.2 Previous results and proposed setup design

In analogy with previous experiments [10], an array of plastic scintillator telescopes will be used to detect electrons and positrons.
In particular, the scintillating material chosen is EJ200 [37], commonly used in the detection of electrons. It is characterized by a good transparency to visible light, with an emission spectrum compatible with the most common photodetectors. The intrinsic light yield is large (10^4 *photons*/MeV) and the costs are affordable.

Following previous simulation results [38], the design of the setup has been defined. The aim of the simulation study was the optimization of the dimensions of the calorimeters used to detect electrons and positrons, with the additional goal of reducing systematic errors.

3.2.1 Calorimeters dimensioning

In a previous work [38], I had estimated the optimal dimensions of the plastic scintillator (EJ200) calorimeters that will be used as second layers of $\Delta E - E$ telescopes. The specification was to completely contain electron/positron trajectories or electromagnetic showers produced by leptons entering the detector with an energy of $E \leq 10$ MeV.

The behavior of electrons and positrons which hit orthogonally a face of the calorimeter has been simulated using PENELOPE code [39].
By looking at the positions where the simulated particles are absorbed it is possible to estimate the minimal dimensions needed to measure the total particle's energy. In figure 3.4 the absorption position in the parallel and orthogonal direction with respect to the particle's momentum direction is shown for several emission energies. It is possible to see that, at these energy scales, electron and positron ranges are compatible both in the parallel and in the orthogonal direction with respect to the momentum direction of the particles.
These results show that the minimal dimensions to stop completely e^- or e^+ at 10 MeV are slightly more than 6 cm in the parallel direction, and about 5 cm in the orthogonal one.

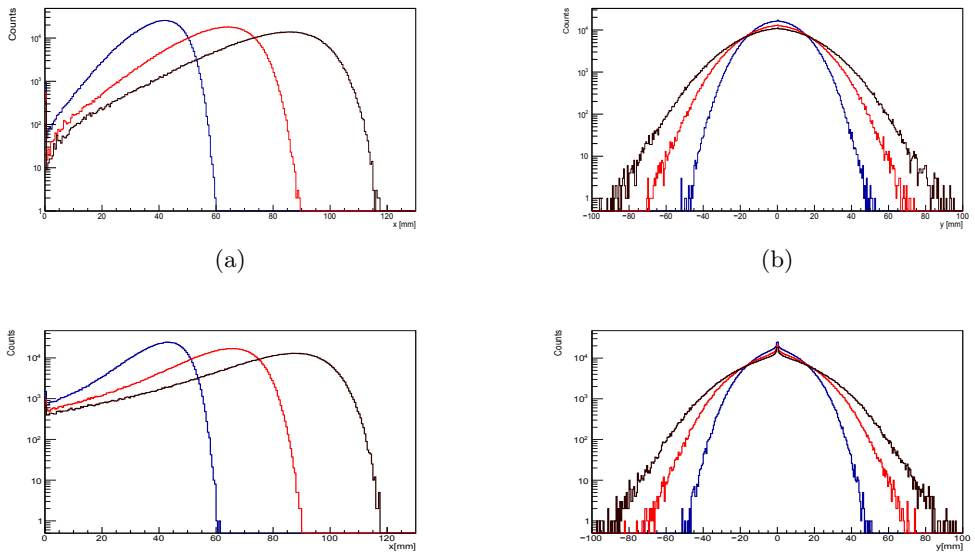

(a) (b) (c) (d)

Figure 3.4: Absorption position of electrons ((**a**), (**b**)) and positrons ((**c**), (**d**)), with a logarithmic scale on the counts, at different emission energies: 10 MeV (blue), 15 MeV (red), 20 MeV (brown). [38]

These results led to the request of using a cubic scintillator of side 10 cm. From the practical point of view, handling a scintillator of these dimensions given the physical constraints of the setup turns out to be complicated. Therefore, it was decided to use smaller calorimeters with dimensions 5 cm $\times$ 5 cm $\times$ 10 cm arranged in groups of four in a *clover* configuration. The deposited energy will be read out independently and properly sum in the analysis, provided that a strict coincidence gate is applied.

3.2.2 Beam pipe effects on systematic error

In the setup described in paragraph 2.1.2 [10] a Carbon beam pipe is used to keep under vacuum the beam and the ^7Li target. The detectors are outside this beam pipe.
A simulation of this setup has been performed, for several particle energies and pipe thickness, in order to estimate the effect of the Carbon on the angular resolution. By looking at the entry position in the scintillator of the particles, emitted orthogonally with respect to the scintillator front face, after they passed throughout the pipe, it is possible to estimate the angular systematic error given by the scattering on the Carbon.

The results, reported in the table 3.1, showed that the error due to the pipe is not negligible, specially for energies lower than 10 MeV. Thus it has been decided to use a large scattering chamber capable of containing the detectors, that should now operate in vacuum. This allows to minimize the material budget between the target and the sensitive part of the detectors.

Thickness [mm]	Energies [MeV]		
	10	15	20
0.7	8°	5.5°	3.5°
1	9°	6.8°	4.5°
1.5	11°	8°	5.5°

Table 3.1: Width of angular distribution of particles which has passed through the pipe.

3.2.3 Position measurement

The use of Multi Wire Proportional Chambers (MWPC) to measure the particles entry position in the detectors, adopted by the Atomki group [10] becomes more complicated when the detectors are placed in vacuum. In general, the management of several gas detectors in a very compact geometry carries practical complications

that can be avoided by using other techniques for the particle's tracking. One possible solution would be to use the first layer of the $\Delta E - E$ telescopes to reconstruct the particles positions by exploiting imaging methods.
The response of a thin layer of scintillator to electrons passing through it in a grid of several positions has been simulated in order to verify the possibility of adopting this solution. As shown in figure 3.5, the small amount of scintillation photons produced compared to the large area of the detector does not allow to reach the resolution needed and the imaging method is not applicable.

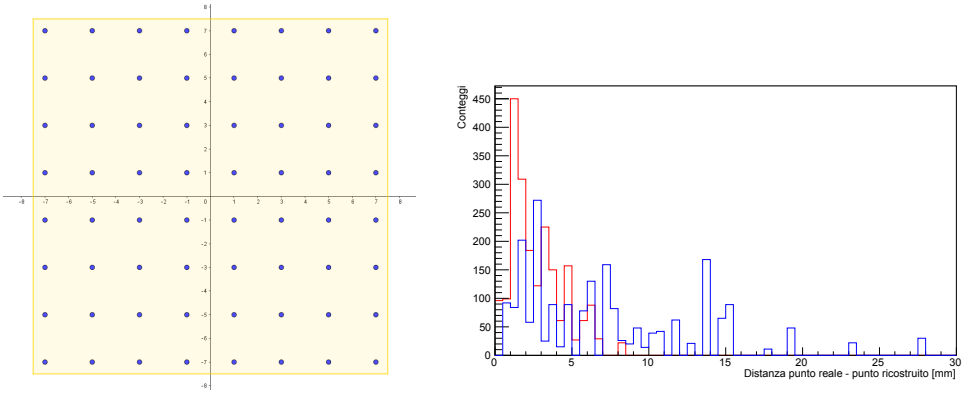

(a) (b)

Figure 3.5: (**a**) Particles emission positions grid. [38] (**b**) Reconstruction resolution when reading the scintillator with an array of square detectors of side 1 mm (blue) and 2 mm (red). [38]

These results led to the decision of using two segmented layers of thin plastic scintillator, each composed by an array of 10 bars. The bars of these two layers are orthogonal to each other: in this way, the first half of the ΔE layer gives one coordinate of the entry position, and the second half of the layer gives the orthogonal direction coordinate.

3.2.4 Proposed setup

Summarizing, the issues and possible solutions explained above led to the current setup design.

The building block of the setup is the plastic scintillator $\Delta E - E$ telescope shown in figure 3.6a. The E layer is constituted by a 5 cm $\times$ 5 cm $\times$ 10 cm EJ200 scintillator [37]. The calorimeter is read by a Silicon PhotoMultipliers (SiPMs), in order to be able to place the detectors inside the scattering chamber.
The ΔE layer is formed by two layers: each layer is composed by 10 EJ200 bars of dimensions 0.5 cm $\times$ 0.5 cm $\times$ 5 cm, read by an array of 2 mm $\times$ 2 mm SiPMs

(figure 3.6b). The signals are read just at the two extremes of the array, to avoid an excessive increase of readout channels: the sum of the signals amplitudes at the two extremes of the line gives the total energy deposited, while the ratio between their difference and their sum makes possible to know which bar has been hit, thus it is possible to know one coordinate of the entry position of the electrons in the telescope.
By placing the bars of the second layer orthogonally on respect of the first one's bars, a grid is obtained, as shown in figure 3.6c, allowing to know both the coordinates of particles entry positions in the telescope.

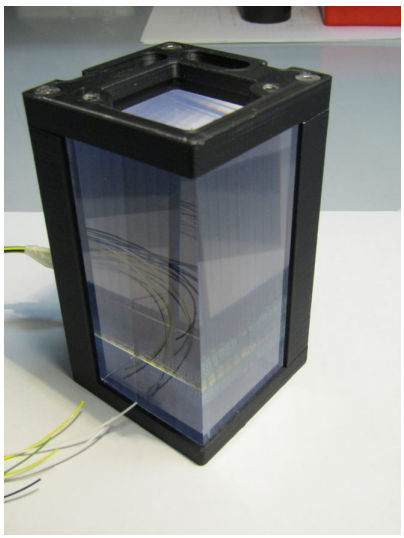

(a)

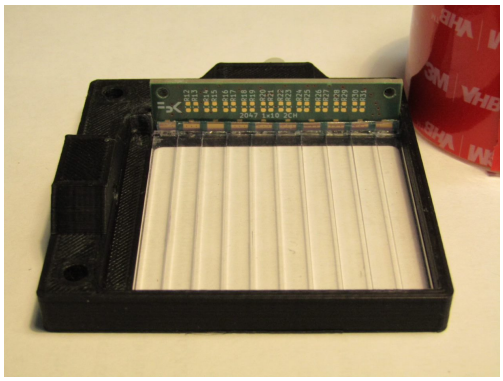

(b)

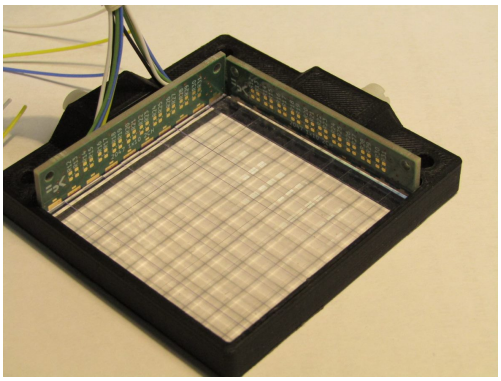

(c)

Figure 3.6: (**a**) $\Delta E - E$ telescope prototype. (**b**) First half of ΔE layer of the telescope composed by 10 bars read by an array of SiPMs. (**c**) Complete ΔE of the telescope, composed by two layers of orthogonal bars, read by 2 arrays of SiPMs.

The upper level in the setup on respect of the telescopes are the clovers, obtained by gathering 4 telescopes. A plastic cage is used to support the telescopes, as shown in figure 3.6, thus there is a cross where the clovers are blind, centered at the contact point of the telescopes, on the side facing the target; although, there are no plastic interfaces between the calorimeters of the same clover, making it equivalent to a unique 10 cm cubic calorimeter.

The clovers are placed at 15 cm from the center of the target, with the ΔE layer facing it. The project plans to produce and use 5 clovers, placed at different angular position in the plane containing the target center orthogonal to the beam direction.

3.3 Simulation

In order to design a new setup to perform independently the measurement a Monte Carlo simulation is needed to know the response of the detectors to the radiation measured.
This thesis work focalizes on a complete simulation of the overall setup, useful to develop the analysis code and to know the setup response expected. The simulations have been performed using GEANT4 simulation software.

3.3.1 GEANT4

GEANT4 [40–42] is a software package to simulate the passage of particles through the matter, firstly developed in 1998 in the context of the RD44 project, a collaboration of CERN and KEK [43]. The reference documentation allows to develop specific implementations for the simulation of customized detectors [44]. Several aspects of a simulation process can be tuned:

- geometry;
- materials;
- fundamental particles;
- generation of primary events;
- tracking of particles;
- particles interactions;
- response of sensitive detector components;
- storage of events and tracks;
- graphic visualization of detectors and particles trajectories;
- capture and analysis of simulation data.

At the base of GEANT4 there is a set of physics models to handle particle interactions with matters at different energies.

GEANT4 is written in C++ and exploit object-oriented methods, which help managing complexity. To build an application the user chooses from among several options and implements the code in user action classes.
The toolkit is composed by several categories, shown in figure 3.7. The categories in the bottom of the scheme are used by the ones above them.
The building blocks are:

- *Global*: system of units, constants, numeric handling and random number generators;
- *Materials* and *Particles*: facilities to describe the physical properties of particles and materials;
- *Geometry*: modules to describe geometrical structures and propagate particles through them;
- *Track*: contains classes for tracks and steps, used by *Processes* category;
- *Processes*: contains implementations of models of physical interactions (i.e. electromagnetic interactions of leptons, photons, hadrons and ions, and hadronic interactions); all processes are invoked by *Tracking* category;
- *Tracking*: manages processes contribution to the evolution of a track state and provide informations on sensitive volumes for hits;
- *Event*: manages events tracks;
- *Run*: manages collections of events sharing a common beam and detector implementation;
- *Readout*: allows the handling of pile-up.

Interface categories connect the described categories to the user.

3.3.2 Simulation description and physics settings

The application developed using GEANT4 describes the overall setup, and it will be used to predict the response of the complete setup and the expected results related to the pairs production and in particular to the pair production following the reaction ${}^{7}Li\,(p, e^{+}e^{-})^{8}\,Be^{*}$.
However, the application has been written in such a way to be general and to allow to easily tune the number and disposition of the detectors, or the particles emitted and their energy and direction. The simulation was used to: study the differences between the electron and positron spectrum on a single clover; estimate efficiency and acceptance of a single clover; evaluate the response of a setup constituted of 5 clovers, in several angular dispositions, to electrons and positrons emitted isotropically; studying the response of the setup to pairs emitted with the energy spectrum and the correlation angle distribution expected from literature [5].
A general description of the application will be given in the following paragraph, together with its general settings.

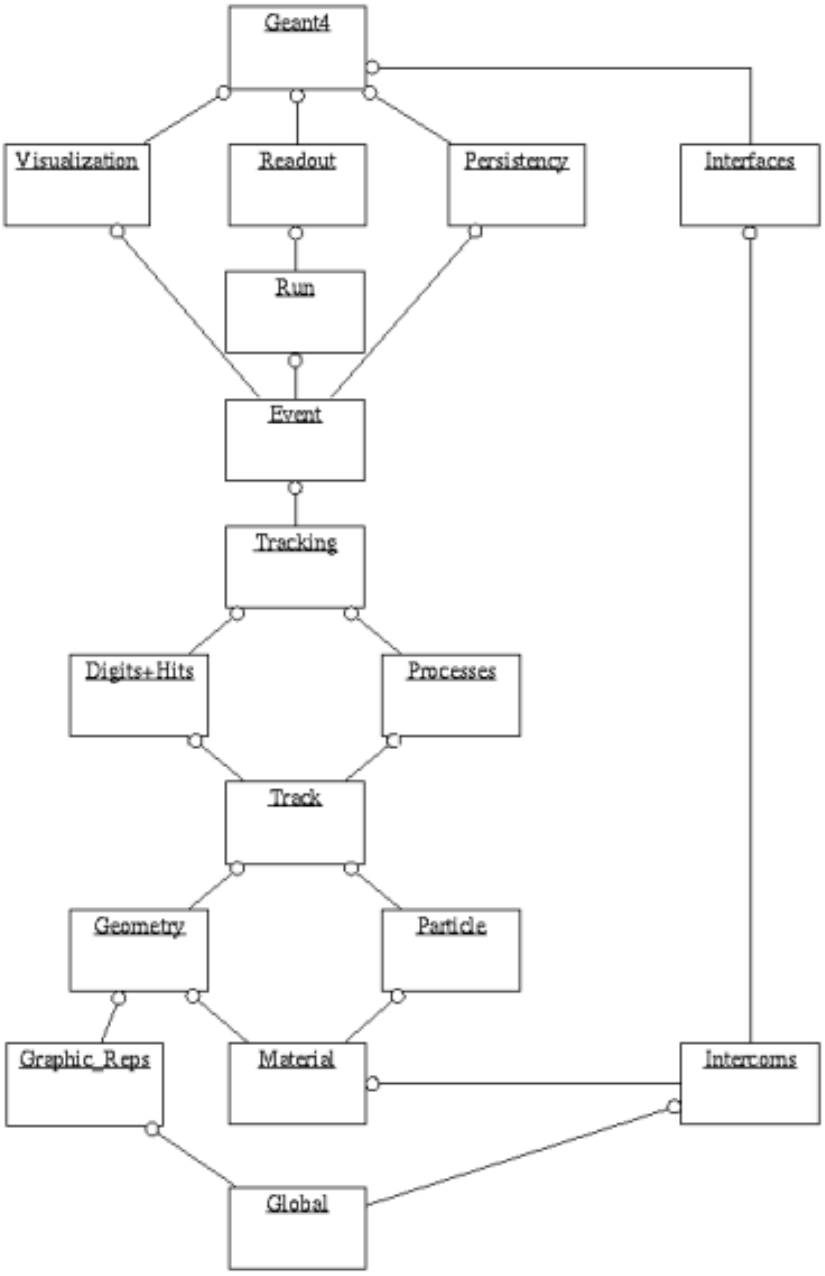

Figure 3.7: GEANT4 class categories. [40]

Physics list

Physical processes are described by different models depending on the energies and kind of particles involved; it is necessary to select the best physics model

to describe the processes of interest for the specific case that must be simulated. Moreover, in some cases, the user may want a faster and less-detailed application and rarely an application needs do compute all the physics processes at the same time. For those reasons, GEANT4 does not provide a complete set of physical processes, but chooses to provide many physics models, the appropriate selection has to be made by the application developer. The different models are described inside the *Physics lists*: these are the classes which collect all the particles, physics processes and production threshold needed for the application, and tell the run manager how and when to invoke physics. Users could include predefined lists, or build their own one by selecting directly the processes instead of the models.
The *Physics list* defines the list of particles included, the interactions included, and the energy cuts for secondary production.

The list used in this application is FTFP_BERT_PEN, that is a model based on the FRITIOF description of string excitation and fragmentation [44], which use a standard electromagnetic description for energies between 1keV and 1PeV and includes PENELOPE, the simulation code used in the previous simulation described in section 3.2.

Particle emission

GEANT4 provides the *G4ParticleDefinition* class to represent particles. A derived class is then implemented for the specific particle types and the user could also create his own particle class.
The most important particles for the application described in this thesis are electrons, positrons, γ rays.

In the simulation it is important to distinguish between primary and secondary particles: the former are the particles emitted at the beginning of each event, while the latter are the ones produced by the collisions between the primary particles and the materials particles.
In the application described here, the primary particles are electrons and positrons, emitted exploiting G4ParticleGun method [44]. For each particle emitted it is necessary to select the initial position, the initial momentum direction and the initial total energy.

At the beginning of each event both the electron and the positron are emitted, with different direction and energy settings depending on the specific goal of the simulation.
The initial position, shared by the two particles of each pair, is uniformly distributed in a parallelepiped of dimensions 1 mm $\times$ 1 mm $\times$ 0.0035 mm center in the origin.

Geometry settings

The setup geometry is a fundamental element of the simulation, both for detector definition and for other solid bodies definition (i.e. the target, the plastic supporting the telescopes, the scattering chamber walls, etc.).

The geometrical representation of all these elements focuses on the definition of solid models and their spatial position, as well as their logical relations to one another, such as in the case of containment.
The concept of *Logical Volume* describes bodies element properties. The concept of *Physical Volume* allows to manage the spatial positioning of the volume and its logical relations with other volumes. Finally, the concept of *Solid* is used to manage the volume solid modeling.

As explained in paragraph 3.2.4, the building block of the setup is the plastic scintillator $\Delta E - E$ telescope, and 4 telescopes are gathered in a clover detector. A clover detector with the geometrical characteristics described in paragraph 3.2.4 has been defined, made up of G4_PLASTIC_SC_VINYLTOLUENE, that is the most common plastic scintillators material, properly representing EJ200. Each component of the telescopes has been defined singularly, and then the clover has been assembled using G4AssemblyVolumes methods [44].
In figure 3.8 an example of a simulated telescope and of a simulated clover are shown.

Using the MakeImprint function [44], the assembled clovers are physically placed in the selected spatial position. In the simulation of the complete setup, they have been placed in a plane orthogonal to the beam direction (z axis direction), at a distance $d\,(Source, Det) = 15$ cm and relative angle positions of 0°, 45°, 105°, 155° and 245°. The setup simulated in this arrangement is shown in figure 3.9b. This particular geometry has been chosen in order to break the symmetry present in the setups used by Atomki group in their experiments [10], presented in paragraphs 2.1.2 and 2.2.1.
It has been performed also a simulation, shown in figure 3.9a, using the angular disposition 0°, 60°, 120°, 180° and 270°, characterizing the Hungarian group experiment.

Hits and sensitive detectors

Once the geometry and the physics are defined, it is necessary to collect and save detector responses. This fundamental step of a simulation is provided through G4Hit and G4SensitiveDetector classes [44].

A *hit* is a picture of the physical interaction of a particle track with a sensitive re-

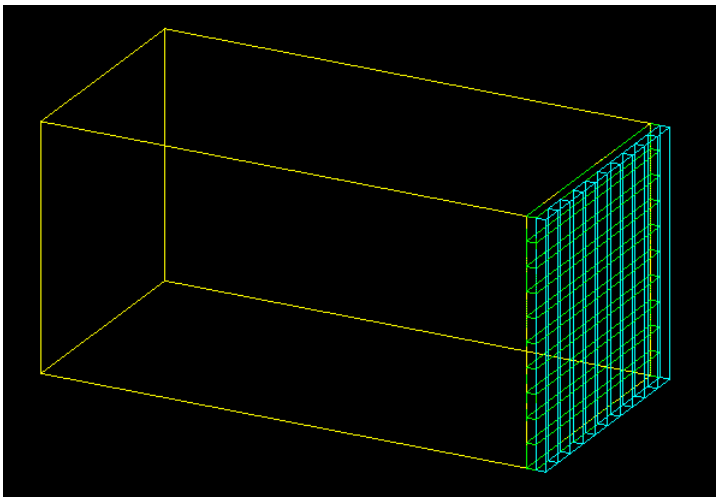

(a)

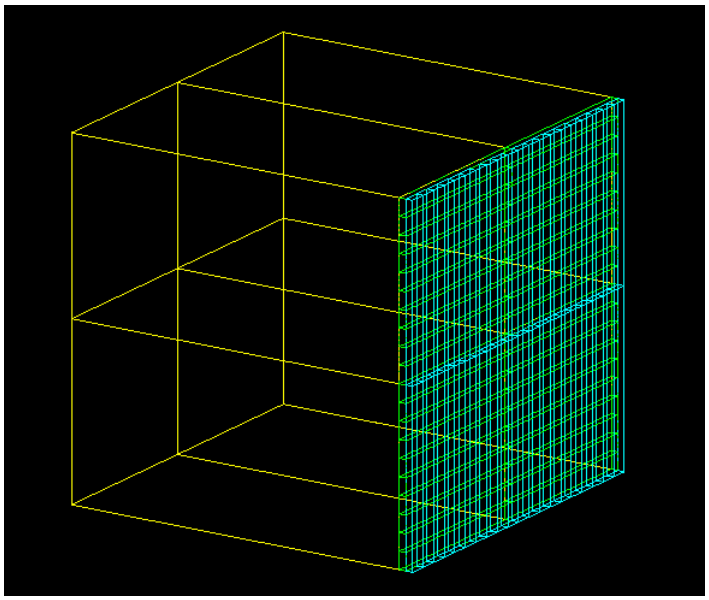

(b)

Figure 3.8: Example of a simulated telescope (**a**) and clover (**b**).

gion of a detector. In a *hit* it is possible to store information associated to G4Step object, describing the step of the particle after each interaction; the stored information could be the energy deposited in the step, as in the case of the application described in this thesis, but also geometrical or timing information.

G4VSensitiveDetector is a class representing a detector. The principal task of a sensitive detector is the construction of *hit* objects using information from steps

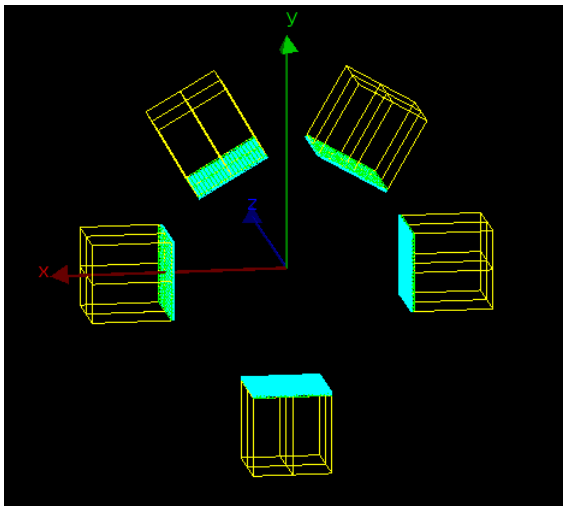

(a)

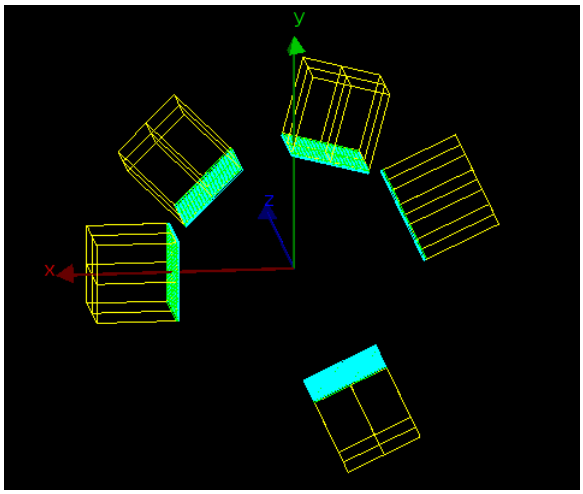

(b)

Figure 3.9: Simulated spectrometer with relative angular disposition $0° - 60° - 120° - 180° - 270°$ (**a**), similar to the setup used in the Atomki experiment, and $0° - 45° - 105° - 155° - 245°$ (**b**), that is one of the new configurations proposed.

along a particle track.

In the application here described, three different kinds of sensitive detectors have been defined, and thus three different *hit* collections: a first group of sensitive detectors are the calorimeters, a second one are the horizontal bars of the telescope ΔE layer, and the last one the vertical bars, always part of that layer.
This division has been done to distinguish in a neater way the detectors, although the information scored in the *hit* are common, namely for each step only the

deposited energy is collected.

Output settings

Finally, in order to interact with the simulation, it is necessary to save in an output file all the information collected in the *hits*.
There are different output formats available (ROOT, HDF5, AIDA XML and CSV), but the Analysis Manager classes provide a uniform interface to be used in GEANT4.
G4AnalysisManager class allows to save as output both histograms and ntuples.

The Ntuples saved for the emission geometry debug contain the event identification number, the electron emission vector Cartesian and spherical coordinates, the positron emission vector Cartesian and spherical coordinates and the correlation angle between the two vectors.

Conversely, the Ntuples saved for the proper simulation store the event ID number, the clover ID number, the telescope ID number, the detector ID (namely, calorimeter, horizontal bars and vertical bars) and the detector ID number (i.e., fixed the clover, the telescope and the kind of detector, this ID number identifies which specific component has been hit), and the total deposited energy in the identified detector.

3.3.3 Reconstruction code

In order to reconstruct the positions of the detected particles and the correlation angle distribution, an analysis code written in ROOT has been developed. The code is meant to analyze both pair detection events and single particle detection events.
The outputs of the simulation have been used to test and debug the analysis code.

Single particle detection

At first, the single particle events detection will be described. A single clover will be considered.

The total energy measured is given by the sum of the energy deposited in each telescope ($E + \Delta E$ layers). The $\Delta E - E$ correlation spectrum is given by summing the energy deposited in the bars of the four telescopes to obtain the ΔE measurement, and the sum of the energy deposited in the calorimeters to obtain the E measurement. The result is shown in figure 3.10, showing the $\Delta E - E$ correlation spectra of electrons and positrons emitted with energy 8 MeV. This

would be important to perform graphical cut on E and ΔE in the following analysis regarding the detection of pairs.
Most of the events are placed in the line characterized by a constant sum $E+\Delta E$, as expected, and in particular among these events, most of them are collocated in the region of this line with higher E value and lower ΔE value. The spectra related to positrons differ from the electrons ones because of the additional energy given by the annihilation of the positrons once they stopped inside the calorimeter: indeed, most of the events are placed in the line where $E+\Delta E$ is constant, as for the electrons, but a certain amount of events is located also in a region where this sum is higher.

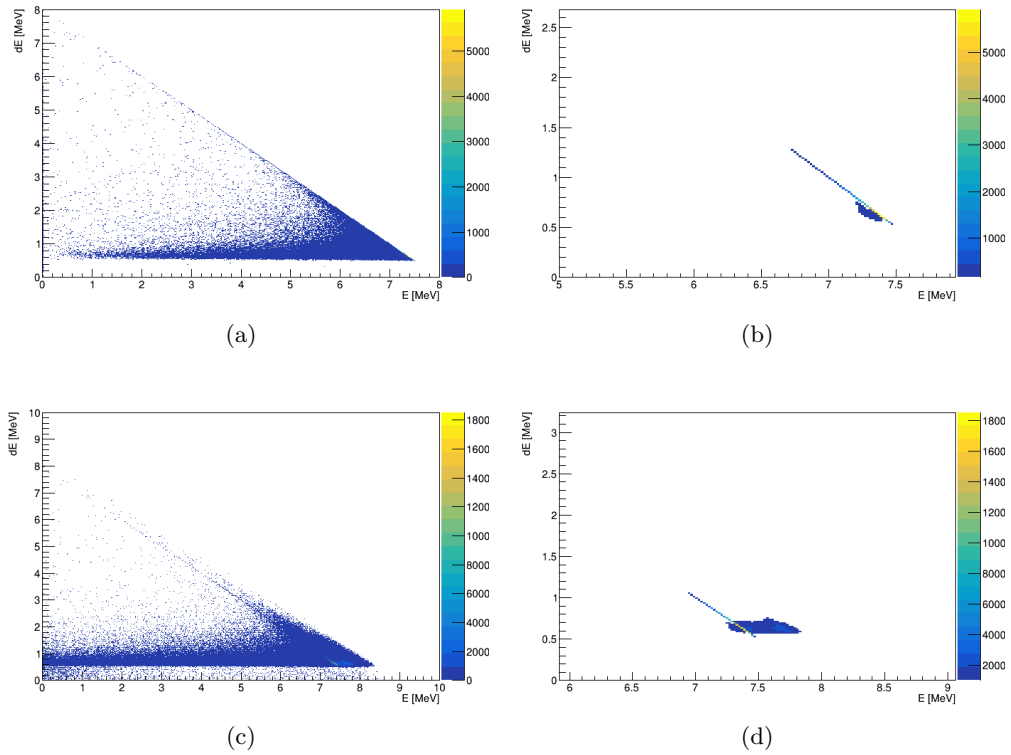

Figure 3.10: Correlation $\Delta E - E$ spectra of electrons ((**a**) and (**b**)) and positrons ((**c**) and (**d**)) emitted at 8 MeV, showing all the events ((**a**) and (**c**)) or highlighting the most populated regions setting a minimum number of events to plot ((**b**) and (**d**)).

A fundamental aspect of the analysis is the reconstruction of the particle positions. Calling the positions coordinates x and y, each particle would deposit a certain amount of energy ΔE_x in the first layer of bars (X bars) composing the ΔE layers of the telescopes, and a certain amount ΔE_y in the second layer of bars (Y bars).

If all of the ΔE_x energy deposited in the X bars has been deposited in a single bar of that layer, the entry x coordinate is clearly defined, since it is clear which is the bar crossed by the particle. It would be analogous for the y coordinate.
However, it is likely for a particle to deposit energy in neighboring bars on different layers. Therefore, it is necessary to develop a method to reconstruct the entry position also for events with energy read in more bars in one or both the ΔE layers. Moreover, this method would take into account also the possibility of pile-up events and discard them.

The method consists in a set of rules that have been selected to discriminate the good events and the pile up events, and to define a position once the event has been considered as a good event:

- if no bars detected energy, i.e. if the particle entered from the side of the clover like in the example shown in figure 3.11, the event is discarded;
- if a particle hit just one bar for each layers the event is good, and the position is directly given by the X and Y bars hit;
- if the energy has been deposited in more than one bar at least in one layer, the event is considered good if:
  - **I** all the bars detecting energy are adjacent;
  - **II** if more than 3 bars detecting energy, the sum of the 3 largest energies is greater than 98% of the total energy deposited in that layer;
  - **III** if more than 3 bars detected energy, the 3 with largest energy are adjacent and the one detecting the largest energy is between the other two bars.
- if the energy has been deposited in more than one bar at least in one layer and the conditions **I**, **II** and **III** are respected, the entry coordinate related to that layer is given by an average of the two or three bars selected, weighted on the energy measured by each of those bars.

Finally, some energy cuts given by the previous $\Delta E - E$ correlation spectrum are applied in order to remove events that are not in the electron or positron energy regions.

These conditions require that most of the energy deposited in a layer is concentrated in a single bar or in the closest ones. This method fails in recognizing events where several hits on nearby scintillator strips where produced but globally, the reconstruction efficiency of good events is of almost 95%.
At the same time, this is a very good method to remove pile-up events, given by

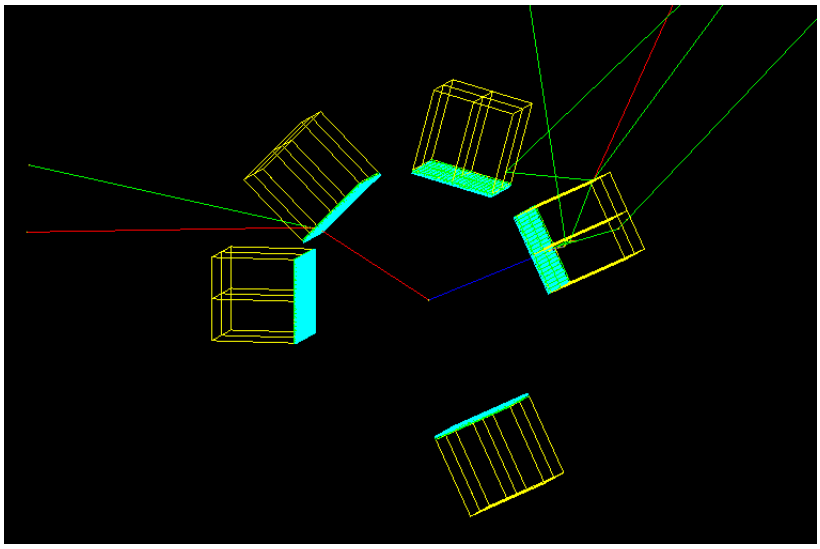

Figure 3.11: Example of a simulated pair event: the simulation code will save the energy deposited by the electron (red), the positron (blue) and the γ-rays (green) in the clover on the left and on the right, since all the requests to consider the observed event a good one are satisfied. However, for example, the energy released by the γ ray on the upper clover will not be saved, because the radiation is not entering passing through the ΔE layer, so this request is not satisfied.

two particles entering in the same clover. So, the result obtained is a good balance between reconstruction capability and background reduction.

Moreover, requiring a triple coincidence in the three layers of the telescope reduces a lot the background. Indeed, the major background source are the γ-rays emitted by the excited states of ^8Be populated with the $^7Li\,(p,\gamma)^8\,Be$ reaction, in particular the ones emitted by the 18.15 MeV resonant state.
As seen in paragraph 3.1.2, the γ-rays interact with plastic detectors mainly by Compton scattering, and with a relatively low cross section. Therefore, requiring a triple coincidence in all the telescope layers would lower even more the probability of detecting a γ-rays, although it won't be null.
In order to estimate the background rate given by this contribution, 1 million 18.15 MeV γ-rays emitted orthogonally in the center of the clover frontal face have been simulated: as shown in figure 3.12, representing the measured energy spectrum, just 569 have been detected. So the γ detection efficiency is of the order of $\epsilon_\gamma \sim 6 \times 10^{-4}$.

Thus, an approximate estimation of the signal to noise ratio, that is the ratio

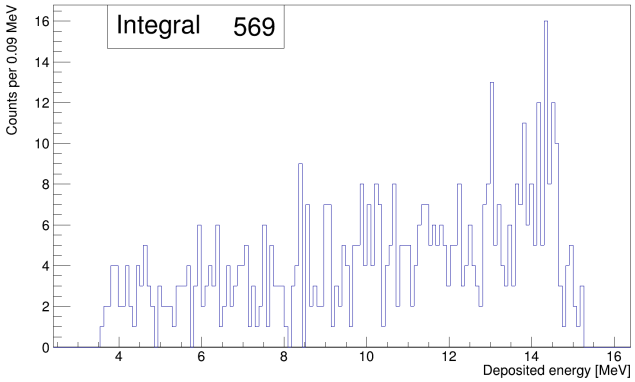

Figure 3.12: Measured energy spectrum of γ-rays emitted at 18.15 MeV orthogonally to the clover frontal face.

between the number of e^+e^- and γ pairs detected, respectively $N_{e^+e^-}$ and N_γ, is:

$$R = \frac{N_{e^+e^-}}{N_\gamma} = \frac{\epsilon^2_{e^+e^-}}{\epsilon^2_\gamma} \cdot \beta \tag{3.9}$$

where $\epsilon_{e^+e^-}$ and ϵ_γ are the intrinsic detection efficiency of electrons (or positrons) and γ-rays in a single clover, and β is the IPCC defined in the equation 1.21. Both the efficiencies are squared, since a coincidence between two clovers is needed. The geometric acceptance is not taken into account because it's equal for both the leptons and the γ-rays.
By inserting in this expression $\epsilon_{e^+e^-} \sim 0.95$, $\epsilon_\gamma \sim 6 \times 10^{-4}$ and $\beta \sim 5 \times 10^{-6}$, it results $R \sim 13$.

This result could not grant a perfect discrimination between the signal and the background, but it still allows to easily have control over the background.
Moreover, adding energy cuts the obtained results improved a lot.

Pairs detection

Once the position and energy reconstruction is defined for the single particle detection with a single clover, it is necessary to reconstruct the correlation angle and the invariant mass of the pairs detected.

At first, a cut is imposed in the total energy measured for each pairs, in order to be sure that a pair is related to the transition we are interested in.
Moreover, an event is discarded also if more than two clover are related to events that have been considered good in the previous analysis.

If the pair event is not discarded, the directions of the two particles with respect to the laboratory frame is computed: given the position vector of the center of the hit clover frontal face $\vec{v}_{det}$ in the laboratory frame, and the entry position in the clover frame $\vec{v}'_{in}$, obtained in the previous analysis, the direction of a particle is $\vec{v}_p = \vec{v}_{det} + \vec{v}_{in}$, where $\vec{v}_{in}$ is the transformation of $\vec{v}'_{in}$ in the laboratory frame. Once the directions of both particles have been reconstructed the correlation angle computation is direct.

3.3.4 Energy detection efficiency and resolution

As first step, the application built has been used to estimate particle detection efficiency and resolution as functions of the emission energy of the particle itself.

In order to perform this estimation, at first a single telescope and then a single clover detector have been built in the simulation, to avoid possible back-scattering contribution given by the presence of other materials.
Only a particle has been emitted at the beginning of each event instead of emitting both the electron and the positron. Different simulations have been performed for electrons and positrons.
The particle emission direction has been fixed to enter the detector very close to the center (it doesn't enter precisely on the center of the detector because of the initial position uniform distribution described in paragraph 3.3.2).
Several simulation have been performed varying the emission energy from 2 MeV to 18 MeV, each 0.5 MeV, both for the electrons and positrons.

The analysis code is very similar to the one described in the paragraph 3.3.3, although there are no energy or pile-up cuts.

Deposited energy spectrum of electrons and positrons

For each emission energy set, a deposited energy spectrum is obtained, as the ones shown in figure 3.13.

Both the electron and positron deposited energy spectrum present a peak at the emission energy, due to a complete deposit of the initial energy in the calorimeter. In addition, a tail at lower energy is visible in the two distributions. This is given by losses of energy due to a few electron or positron exiting the calorimeter or γ rays emitted by Bremsstrahlung which escaped the detector. Given the calorimeter dimensions it is less probable to observe great losses, so the lower energy tail is way higher at energies close to the emission energy peak (i.e., few energy losses) than at low energies, where greater losses are required. It is worth to notice a pseudo-peak just at the left of the emission energy peak, in the lower

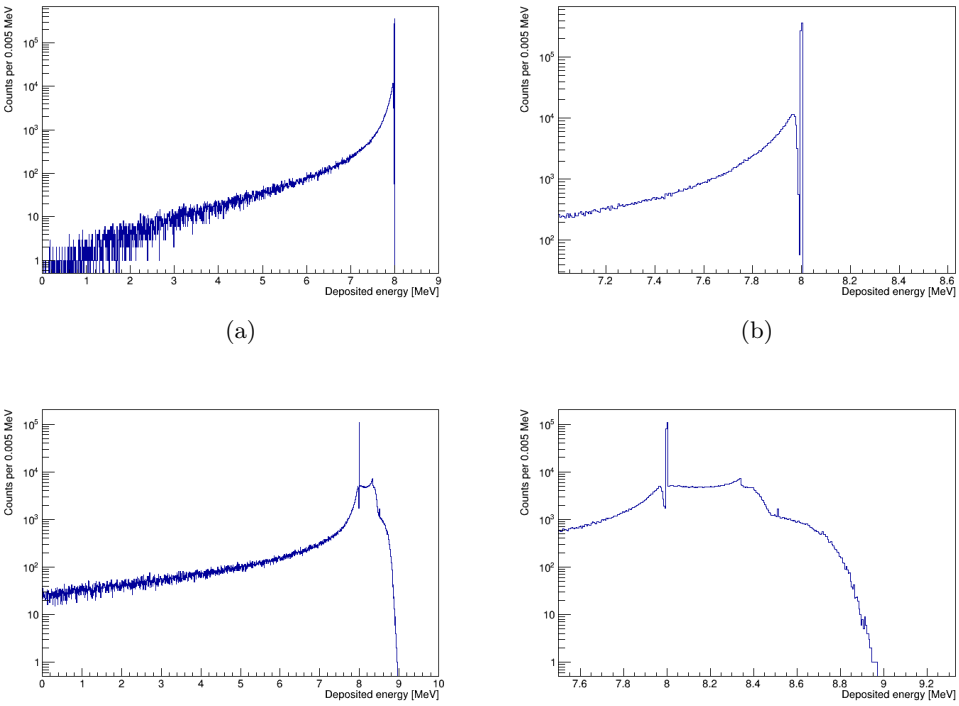

Figure 3.13: Energy deposited in the clovers by electrons ((**a**) and (**b**)) and positrons ((**c**) and (**d**)) represented in logarithmic scale. In the figures (**b**) and (**d**) the spectra regions close to the emission energy peak have been highlighted to better observe the peaks and Compton structures formed.

energy tail: indeed, it has to be considered also that a γ produced with low energy, related to the little losses required to populate the right region of the tail, has a low probability to escape the detector, and it would be measured and the detected energy would be again the emission one. Thus, the lower energy tail would not be given by a simple probability distribution of the energy lost by the particle via Bremsstrahlung or exiting the calorimeter; instead, it would be a convolution between this distribution and the probability of a gamma with a certain energy to escape the detector.

Finally, it is evident the higher energy tail in the positron deposited energy spectrum, not present in the electron one: this additional region of the spectrum is given by the annihilation of the positrons with the atomic electrons of the calorimeter material. A peak is clearly visible at 511 keV above the emission energy peak, due to the detection of one of the two γ rays produced in the annihilation. The

region closer to the emission energy peak, that is given by the Compton scattering of one or both the γ produced, is much more populated than the photo-peak, because at this γ energies the Compton scattering is much more likely than the photoelectric effect. At 340.7 keV it is visible the Compton edge related to the Compton of one γ, as expected.
It is not present a photopeak at 1.022 MeV because the detection of both the γ rays is very unlikely.

To check this interpretation a simulation of two 511 keV γ rays emitted in coincidence inside the calorimeter has been performed. As it could be seen in figure 3.14 the spectrum is exactly the same of the high energy region observed in the positron spectrum.

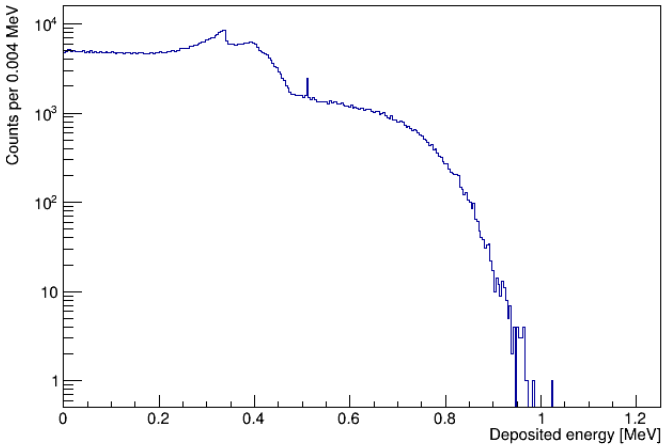

Figure 3.14: Energy deposited in the clover by two γ rays emitted in coincidence from the center of the clover itself, represented in logarithmic scale.

Simulation of the measured energy spectrum

The deposited energy spectrum is not the measured energy one. The measured energy distribution follows a Poisson distribution with expected value N and standard deviation $\sqrt{N}$, where N is the number of photons emitted if an amount of energy E_{dep} is deposited. The number of emitted photons is given by $N = Ly \cdot E_{dep}$, where Ly is the scintillator light yield, as it will be explained in more details in the paragraph 4.1.1.
Thus, in order to obtain the measured energy spectra for several values of the light yield, a Monte Carlo simulation has been performed to convolute the deposited energy spectra with a Poisson distribution.
Let's call a general deposited energy distribution $F_{dep}(E)$, and let's call Ly_{MC}

the light yield value used in the Monte Carlo simulation. A variable $E_{dep}|_{F_{dep}}$ has been randomly selected, following the $F_{dep}(E)$ distribution, and then a random value following the Poisson distribution with parameter $Ly_{MC} \cdot E_{dep}|_{F_{dep}}$ is extracted and saved. This process has been repeated for 1 million times, obtaining in this way the measured energy distribution related to the deposited energy one $F_{dep}(E)$ and the light yield value Ly_{MC}.
In figure 3.15 are shown examples of energy measured spectra for electron and positrons, emitted with energy 9 MeV, obtained with light yield values $Ly = 30.44\ ph/\text{MeV}$ (red histogram), 60 ph/MeV (blue histogram), and 100 ph/MeV (black histogram).

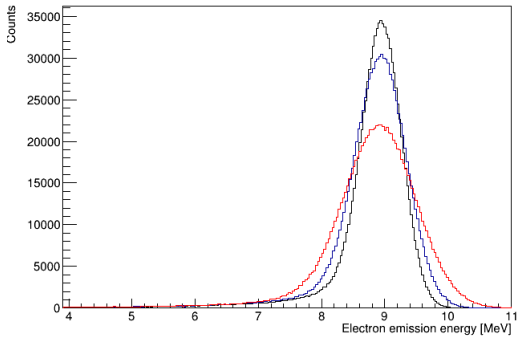

(a)

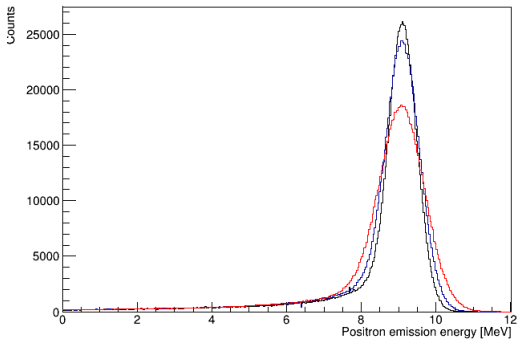

(b)

Figure 3.15: Simulated distribution of the energy that would be measured detecting electrons (**a**) and positrons (**b**) emitted with an energy of 9 MeV, with a light yield $Ly = 30\ ph/\text{MeV}$ (red), 60 ph/MeV (blue) and 100 ph/MeV (black).

In each spectrum, the peak correspondent to the total energy simulated is fitted with a gaussian, and the detection efficiency at that specific energy is calculated as the ratio $\epsilon = \frac{N_{peak}}{N_{sim}}$, where N_{peak} is the integral of the peak within $3\sigma_{peak}$, and

N_{sim} is the number of simulated particles. Moreover, the resolution of the peak is computed as the ratio $R = \frac{\sigma_{peak}}{E_{peak}}$. It has been computed also the difference between the measured energy and the emission one, expressed in percentage with respect to the emission energy.
Then the pairs (E, ϵ) and (E, R) have been plotted to see the efficiency and resolution trends as a function of the emission energy, as it will be shown for each case simulated.

Telescope and clover efficiency

This estimation has been performed for e^- entering orthogonally in a single telescope and then for e^- and e^+ (since in the final configuration the positrons will be detected too) entering orthogonally in a single clover, making it possible to compare the energy detection efficiency of the two detectors, and to estimate the gain granted by the clover configuration.
The trends of efficiencies, resolutions and residuals with respect to the emission energy are shown in figures 3.16 for the telescopes and 3.17 for the clovers. The red crosses are referred to the results obtained with $Ly = 30\ ph$/MeV, the blue circles to the ones obtained with $Ly = 60\ ph$/MeV and the black crosses to the ones with $Ly = 100\ ph$/MeV.

It is clear that the efficiency decreases for increasing values of the emission energy, as expected: indeed, particles with higher energy have an higher probability of reaching the lateral faces of the detector or the regions close to those faces, increasing the energy losses. This is the same reason why the residuals of the measured energy with respect to the emission one increase, in absolute value, as the energy increases. Moreover, the resolution decreases as expected because of the Poisson behavior described before.
It is worth noticing that the efficiency decreases for increasing values of the light yield. This behavior is due to the "enlargement" of the deposited energy spectra given by the Poisson convolution, i.e. the resolution that would be obtained applying the convolution to a δ distribution. Given a deposited energy spectrum for a particle with emission energy E_{emis}, an higher light yield value gives a lower enlargement, so the probability that a random value E_{meas}, extracted from a Poisson distribution centered at an energy $E < E_{emis}$ in the deposited energy distribution, is higher than E_{emis} is low; conversely, if the light yield value is lower, and the distribution is enlarged more by the convolution, this probability would grow, and the high energy tail in the measured energy spectrum would be more populated. Since the efficiency is computed just by integrating the high energy tail, the efficiency would result higher for lower values of light yield.

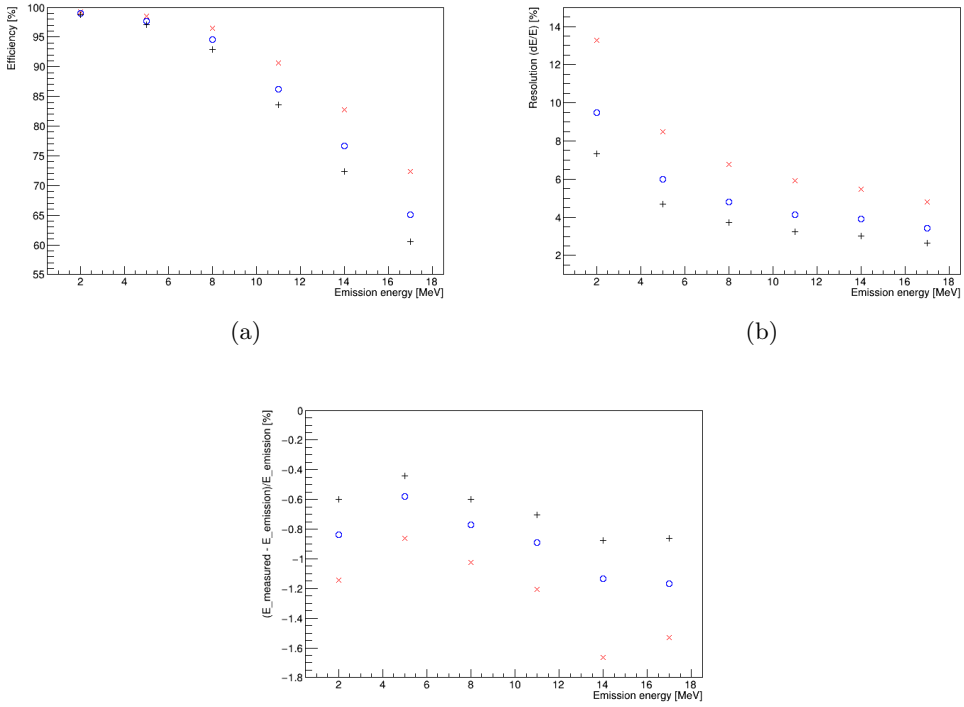

Figure 3.16: Energy detection efficiency (**a**) and resolution (**b**) of a single telescope measuring electrons entering orthogonally in the center of its frontal face, in function of the emission energy of the particles. **c** Percentage difference between the measured energy and the emission one.
Three values of light yield have been used: 30 ph/MeV (red crosses), 60 ph/MeV (blue circles) and 100 ph/MeV (black crosses).

It is noticeable also that the results related to particles emitted with 2 MeV don't follow the trend of the results related to higher emission energies.
Studying the output positions of electron entering in a single telescope, the percentages of particles coming out from the different faces have been estimated, as reported in the figure 3.18.

As shown, particles emitted with 2 MeV don't reach the lateral faces, but most of all come out from the frontal one after back-scattering events, keeping a lot of the starting energy. This is highlighted also by the $\Delta E - E$ spectra, presented in figures 3.19a and 3.19b, showing a lot of events with ΔE higher than E, and by the fact that the peak at the emission energy is present in the ΔE spectrum and not in the E one, as shown in figures 3.19c, 3.19d, 3.19e and 3.19f .

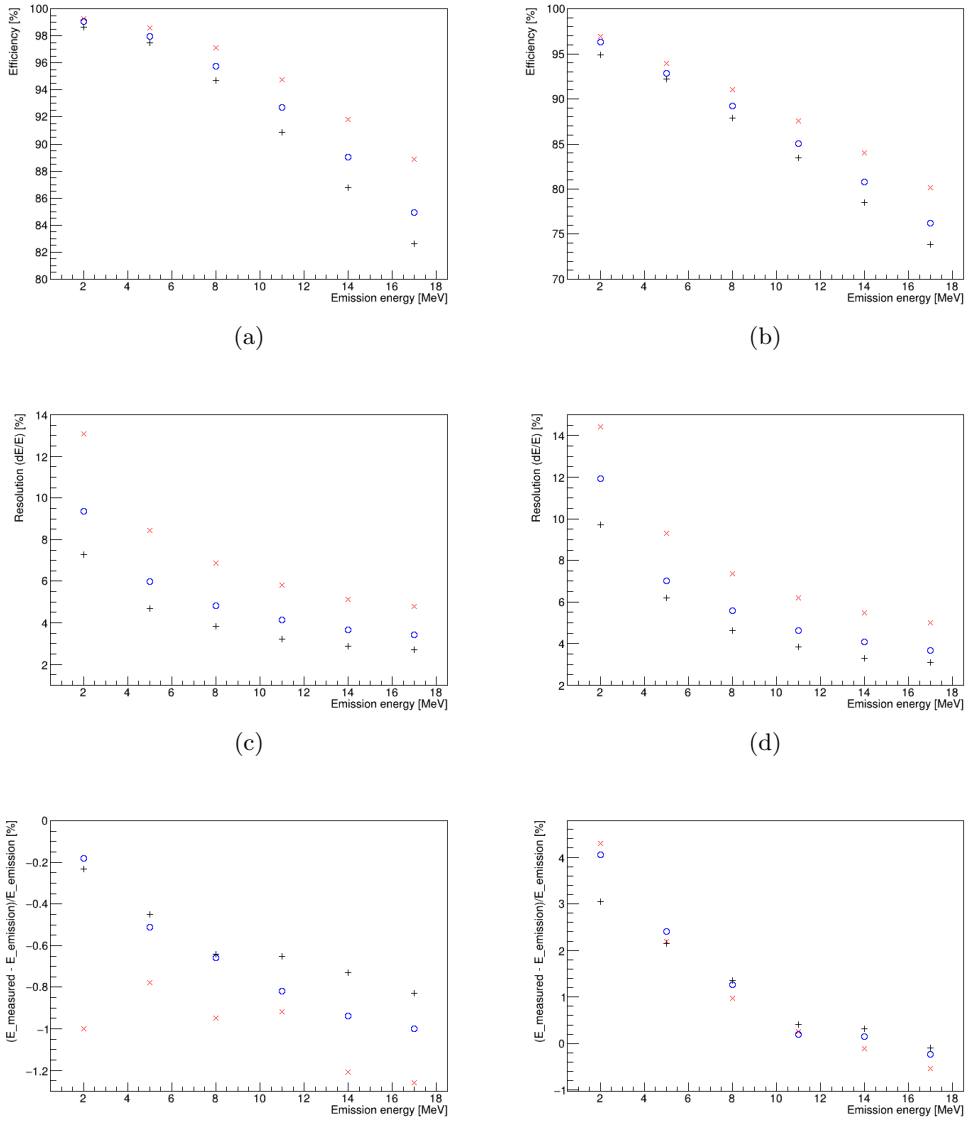

Figure 3.17: Energy detection efficiency (**a**) and resolution (**c**) of a single clover measuring electrons entering orthogonally in the center of its frontal face, in function of the emission energy of the particles. (**e**) Percentage difference between the measured energy and the emission one. The analogue quantities obtained with positrons are represented respectively in the sub-figures (**b**), (**d**) and (**f**).
Three values of light yield have been used: 30 ph/MeV (red crosses), 60 ph/MeV (blue circles) and 100 ph/MeV (black crosses).

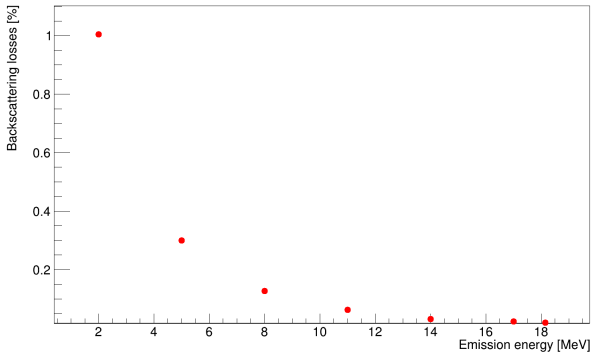

(a)

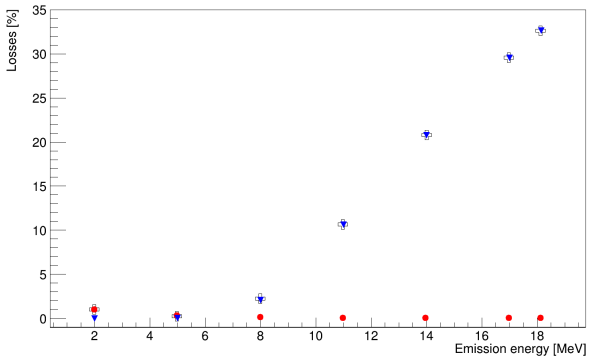

(b)

Figure 3.18: (**a**) Percentage of particle lost from the frontal face, simulating electrons in a single telescope.
(**b**) Comparison of losses from the frontal face (red circles), losses from the lateral faces (blue triangles) and total losses (black crosses), simulating electrons in a single telescope.

Finally, the improvements from the use of a single telescope and the use of a clover, given by the energy recovered in the adjacent telescopes, is clearly visible by looking both at the efficiencies, the resolutions and the residuals trends.
The gain obtained by using a clover instead of a telescope is shown in figure 3.20.

Acceptance effects on the efficiency

After the estimation of the detection efficiency dependence on the energy, a second step is performed: particles are emitted isotropically in the solid angle covering the clover frontal face, in order estimate the single clover acceptance on the detection energy efficiency.

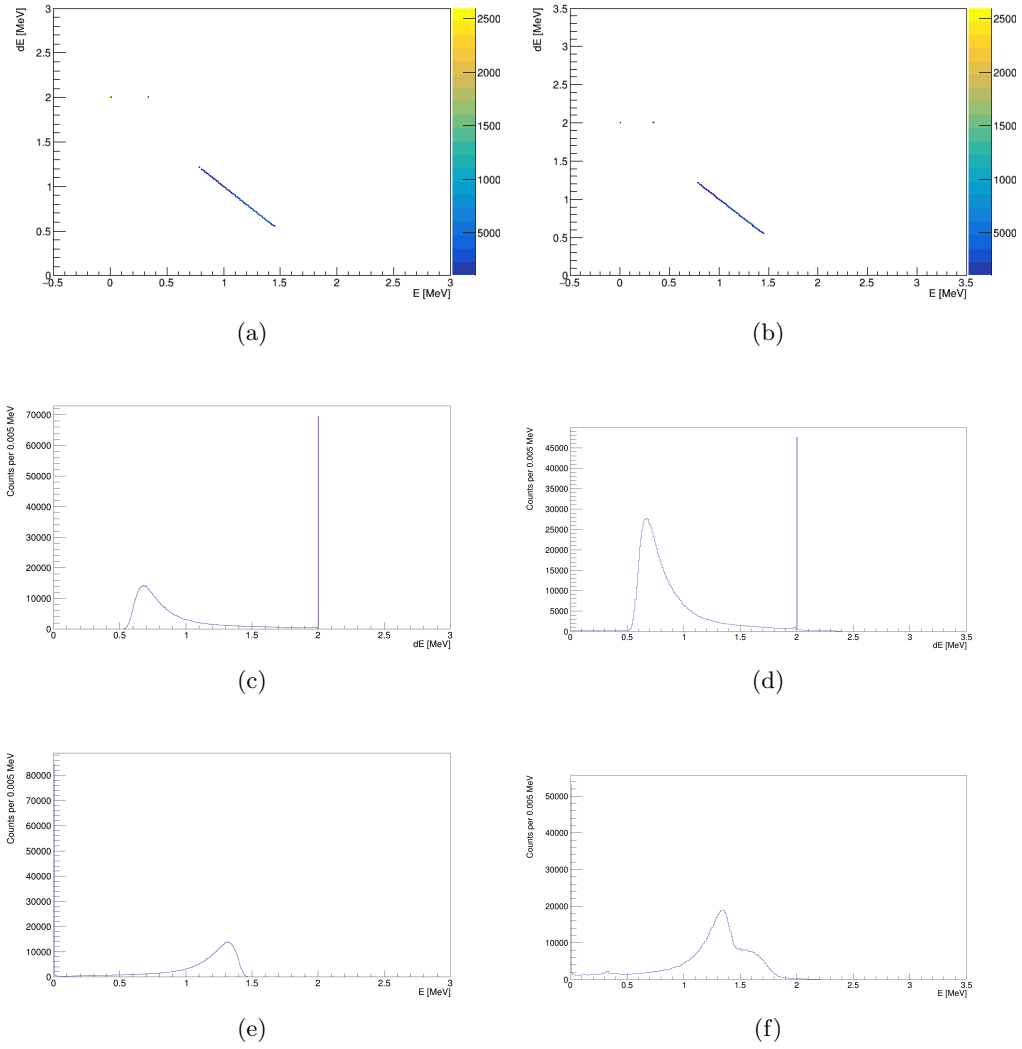

(a) (b)

(c) (d)

(e) (f)

Figure 3.19: Correlation $\Delta E - E$ spectra of electrons (**a**) and positrons (**b**) emitted at 2 MeV, and associated mono-dimensional E and ΔE spectra (respectively (**c**) and (**e**) for e^-, (**d**) and (**f**) for e^+).
In the correlation $\Delta E - E$ spectra a minimum value to plot has been set, in order to highlight the region with most events.

The same peak analysis described before has been performed, and the results are shown in figure 3.21.

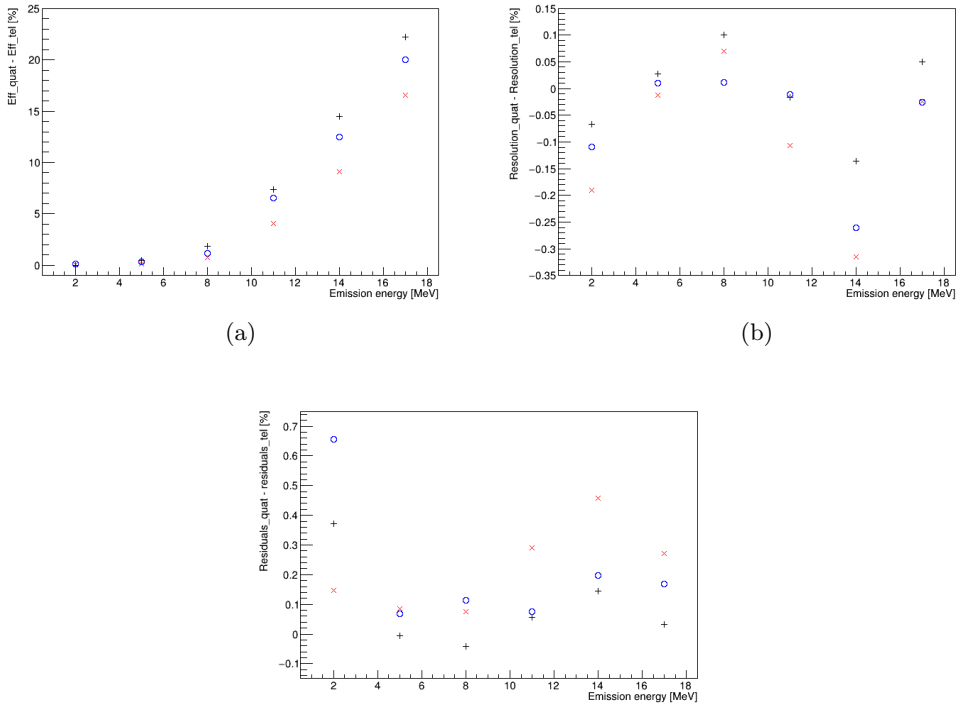

Figure 3.20: Comparison between the single clover and single telescope results: detection energy efficiency (**a**), energy resolution (**b**) and difference between the measured energy and the emission one (**c**).
All the plots represents the gain granted by the clover with respect of the telescope, expressed in percentage of the results obtained with a single telescope.

3.3.5 Correlation angle

Since the anomaly observed in Atomki's experiments described in the sections 2.1 and 2.2 is strictly related to the correlation angle between electron and positron, a fundamental task of the simulation is the study of the overall setup response as a function of the correlation angle itself.

The simulation have been performed with several setup disposition, namely changing the number of clovers and the relative angles between them, in order to find the disposition that breaks better the symmetry and gives a smoother efficiency distribution on respect to the correlation angle.
In this work the disposition resembling the previous experiments one will be presented, together with an example of the other dispositions tested.

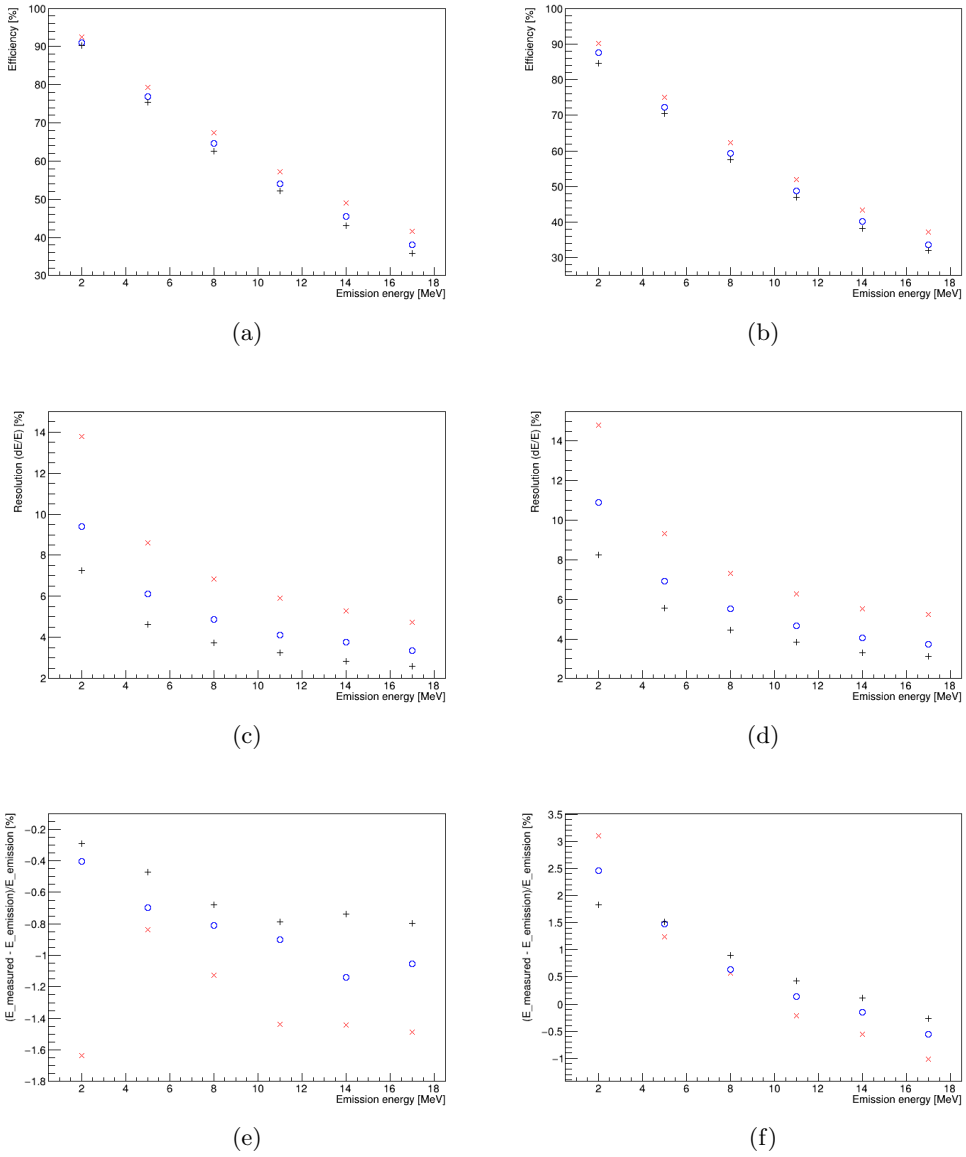

Figure 3.21: Efficiency distribution of the detection energy in function of the emission energy of electron and positrons (respectively (**a**) and (**b**)), energy resolution in function of the emission energy ((**c**) and (**d**)), and percentage difference between the detected energy and the emission energy ((**e**) and (**f**)) for different light yield values: 30 MeV (red crosses), 60 MeV (blue circles) and 100 MeV (black crosses). The electrons and positrons are emitted isotropically in the solid angle covered by the clover.

As first step, the physics expected for IPC in $^{8}Be*$ and $^{4}He*$ decays have not been taken into account. Both electrons and positron have been emitted isotropically, with the electron energy uniformly distributed in $\frac{1}{4} \times 18.15$ MeV and $\frac{3}{4} \times 18.15$ MeV, and the positron energy fixed with the energy conservation, in order to obtain an asymmetry value $-0.5 \leq y \leq 0.5$ as the one selected in the previous experiments [1]; a correlation angle distribution has been obtained as explained in paragraph 3.3.3.
The resulting distribution is shown in figure 3.22.

It is worth noticing that the distribution obtained with the clover placed at angles 0°, 60°, 120°, 180° and 270° is very similar to the one obtained by Atomki's group with the same disposition, reported in figure 2.4b [10].
The expected maximum acceptance for the detection of a single particle is:

$$\epsilon_{max} = 5 \cdot \frac{A_{quat}}{4\pi \cdot d^2(Source, Det)} \tag{3.10}$$

where $A_{quat} = 100$ cm^2 is the clovers frontal faces area, $d(Source, Det) = 15$ cm is the distance between the source and the center of the clovers frontal faces, and the factor 5 is given by the number of clovers.
Therefore, the pair maximum acceptance is

$$\epsilon_{max}^{pair} = \frac{4}{5} \cdot \epsilon_{max}^2 \tag{3.11}$$

because once the first particle has been detected in a clover the second one could be detected in one of the other four clovers.
By inserting the values, it results $\epsilon_{max}^{pair} \sim 2.5\%$: thus, since the intrinsic efficiency of the detectors need to be taken into account, the integral acceptance obtained in the simulation, that is $\epsilon^{pair} = 1.18\%$, is a sensible value.

3.3.6 Future improvements

The described simulation code is now ready to be completed with more realistic details and for the coupling with realistic event generators. The first step will be the addition of the physics settings related to the internal pair creation, in particular:

- energy distribution of electrons and positrons emitted by IPC;
- differential cross section and expected angular distribution of the emitted pairs;
- expected correlation angle distribution, that will be simulated by generating

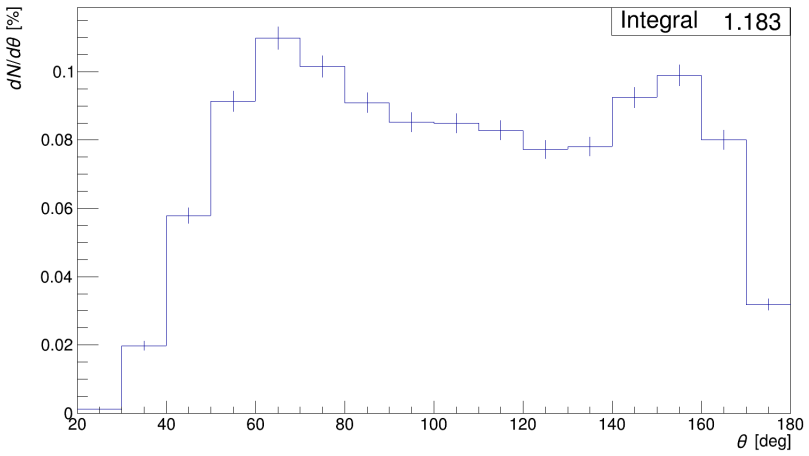

(a)

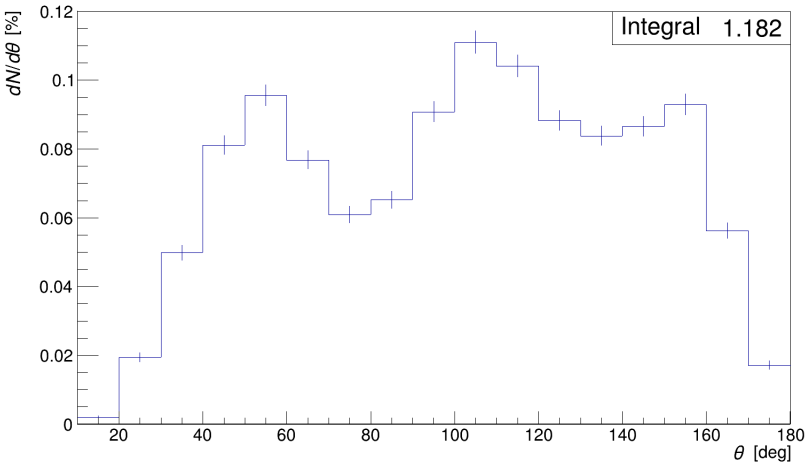

(b)

Figure 3.22: Detection efficiency distribution as a function of the correlation angle between e^+ and e^- for: (**a**) detector placed at angles 0°, 60°, 120°, 180° and 270° (equal to the Atomki experiment disposition) and (**b**) 0°, 45°, 105°, 155° and 245°.

correlated pair following the distribution presented in paragraph 1.3.2, using the method explained in the appendix section A.2;

- expected invariant mass distribution of the pairs.

Then, it will be necessary to estimate the background effects given by the scattering in the present materials:

- target and target supports;
- detector supports;
- SiPMs;
- scattering chamber.

4

Experimental characterization of the detector prototype

This chapter is dedicated to the characterization of the first detector prototypes, designed according to the simulation outcome. Moreover, a comparison between the calculated and the experimental performances is necessary to validate the simulation work and use it for a detailed analysis of the systematic errors. Eventually, the prediction on the reconstructed invariant mass resolution achievable will be discussed.

4.1 Calorimeter characterization

The first component of the setup to be characterized is the calorimeter used in the E layer of the telescopes. The energy resolution as a function of the used photo-detector will be analyzed. The resolution on the measured energies affects both the reconstructed invariant mass resolution and the low energy cuts which have a direct impact on the overall detection efficiency for the most asymmetric pairs.

4.1.1 Light yield and energy resolution

A physical quantity strictly related to the energy resolution of a scintillator is its light yield, defined as the proportional constant Ly that links the deposited energy E_{dep} to the number

$$N = Ly \cdot E_{dep} \tag{4.1}$$

of optical photons emitted by the scintillator.
Measuring a photo peak at a certain energy E_{meas}, since the decay events follow a Poisson distribution, the mean energy of the peak will be proportional to the number of emitted photons $E_{meas} \propto N$, while the peak standard deviation will be $\sigma = \sqrt{N}$. Defining the resolution as $R = \frac{\Delta E}{E}$, it will result that

$$R = \frac{1}{\sqrt{N}} \tag{4.2}$$

Combining the equations 4.1 and 4.2 the relation between light yield and resolution is given:

$$\frac{1}{R^2} = Ly \cdot E \tag{4.3}$$

Thus, by plotting $\frac{1}{R^2}$ against E for several energies, the points are expected to follow a linear trend, and the light yield is given by the fitting line slope.

4.1.2 Light yield calibration by Compton scattering measurements

The lack of mono-energetic electron sources in the few MeV region makes it impossible to calibrate the detector response using this kind of radiation. The Compton effect, on the other hand, can be exploited to determine precisely the deposited energy inside of the organic scintillator. If a gamma-ray with known energy E_γ undergoes Compton scattering in the sample (i.e. the organic scintillator), the scattered electron will carry a kinetic energy in the range between 0MeV and the maximum Compton energy of the incoming photon. The measurement of the scattered photon energy in an external detector (e.g. an inorganic scintillation crystal or an HPGe detector) allows to obtain the deposited energy by using the conservation of energy of the initial photon.

A γ ray, with energy, doing Compton scattering in the EJ200 scintillator would free an atomic electron, that will release its energy E_{e^-}, the one given by the γ during the scattering, in the scintillator itself. Then the γ, which would be at energy $E'_\gamma = E_{gamma} - E_{e^-}$, would escape the organic scintillator, and eventually detected in the ancillary NaI(Tl) detector.
So to observe the Compton events the two detectors are read in coincidence, and the events that aren't within a time window coincidence of 80 ns are discarded.
An example of the resulting coincidence spectrum $\left(E_{e^-}, E'_\gamma\right)$ is shown in figure 4.5.

Experimental setup

An EJ200 calorimeter of dimensions 5cm × 5cm × 10cm is coupled to a 6mm × 6mm SiPM produced by FBK. The bias voltage of the SiPM is 34.2V. The SiPM is connected to an AdvanSiD preamplifier, biased with a double voltage at −5V and 5V. The amplifier output is then fed to a CANBERRA Model 2005 preamplifier and then to a CAEN DT5781A digitizer. This module samples the signal with an Analog to Digital Converter (ADC) and performs two different waveform analyses simultaneously. A digital $(RC)^2$ filter is applied to assign a timestamp to the event obtaining a timing information, and to properly set an energy threshold for the trigger, as shown in figure 4.1a. Moreover, the amplitude information is extracted through a trapezoidal filter, as shown in figure 4.1b. In this case, the input signal (black curve) is filtered into a trapezoidal shape (blue) with amplitude proportional to the initial pulse amplitude. The red curve shows when the trigger occurred while the green one corresponds to the moment when the trapezoidal filter amplitude is sampled. The amplitude value is then merged with the timestamp obtained from the timing analysis and is sent to a computer for storage.
The ancillary detector is a cylindrical NaI(Tl) crystal with a diameter and height of 2", coupled to an Hamamatsu H7195 PMT powered with a high-voltage power supply at −900V. Its output is fed to the CAEN DT5781A digitizer too.

Typical spectra measured in the organic scintillator and the ancillary detector are shown in figure 4.2.

The NaI(Tl) spectra have been calibrated in energy using the full-energy peaks at 1173 MeV and 1332 MeV. The spectrum in the region near the peaks has been fitted using the sum of two gaussians and polynomial functions. A typical case of these fits is presented in figure 4.3.
Once the centroid of the peaks μ_{1173} and μ_{1332} have been obtained, a linear calibration has been performed. The notation used is the following: $E_{calib} = a + b \cdot ch$.

Compton measurements

A ^{60}Co source has been placed so that the direction between the source and the organic scintillator forms an angle slightly bigger than 90° with the direction between the two detectors. The overall setup is shown in figure 4.4. Several tests using different SiPM dimensions and arrangements have been performed:

test 1 single SiPM of dimensions 6 mm × 6 mm, coupled to the EJ200 scintillator in the center of one of the 50 mm × 50 mm faces, powered at 34.2 V;

test 2 two SiPMs of dimensions 6 mm × 6 mm; the first one is coupled to the

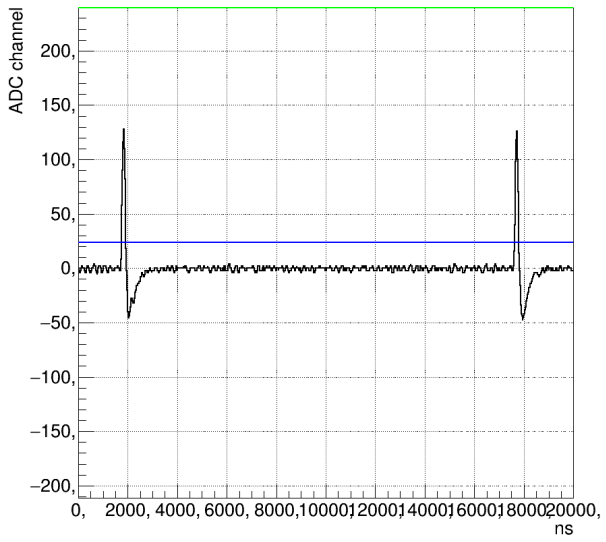

(a)

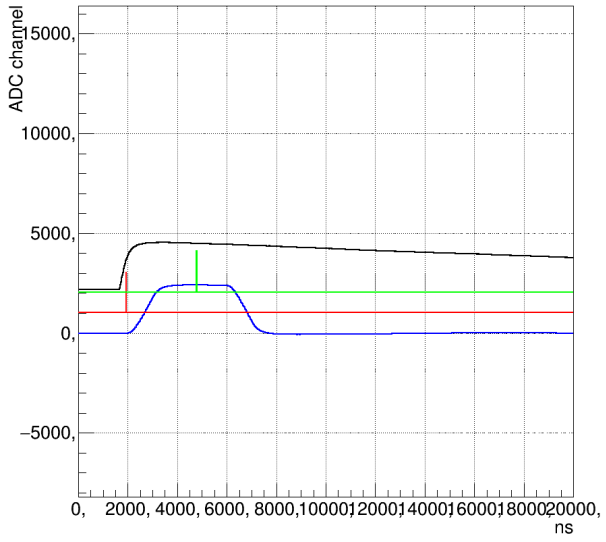

(b)

Figure 4.1: Example of the NaI(Tl) detector filtered signal with $(RC)^2$ filter (**a**) and with the correct trapezoid settings (**b**).

scintillator in the previous positions, and the second one is coupled adjacent to the first; the anode of one is connected to the cathode of the other, and they are powered together at 70.2 V;

test 3 single SiPM of dimension 10 mm×10 mm, coupled adjacent to the previous

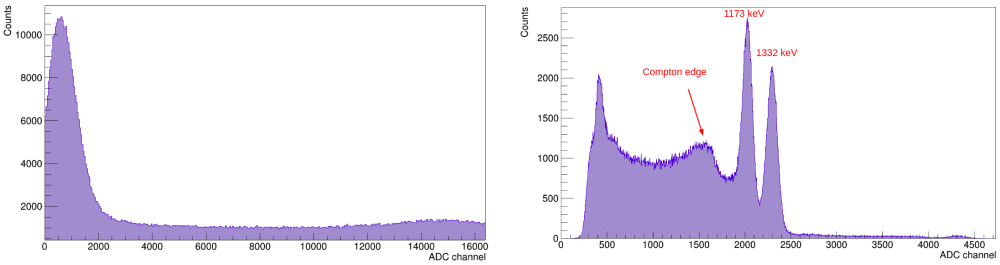

(a) (b)

Figure 4.2: Energy measured by the EJ200 calorimeter (**a**) and by the NaI(Tl) detector (**b**), expressed in ADC channels.

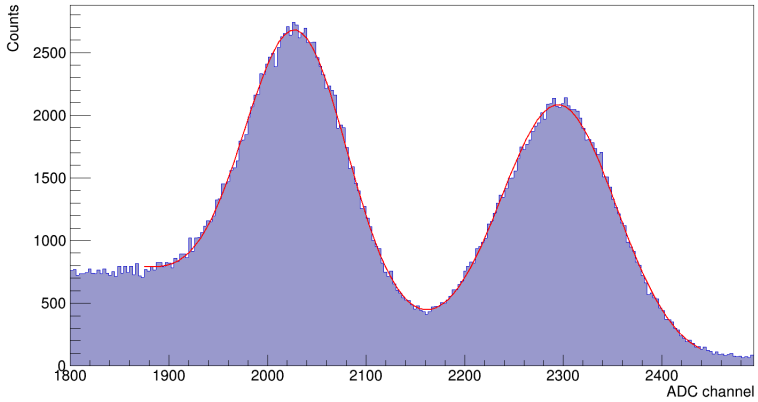

Figure 4.3: Example of fit of the two photopeaks observed in the spectrum of the energy measured in the NaI(Tl) detector.

SiPMs; it is powered at 32.1 V.

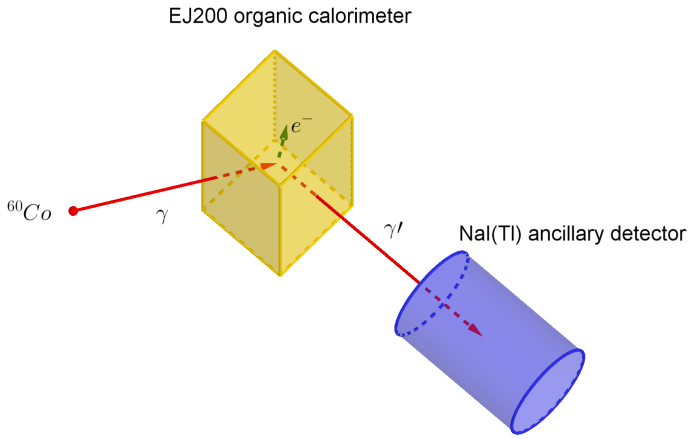

(a)

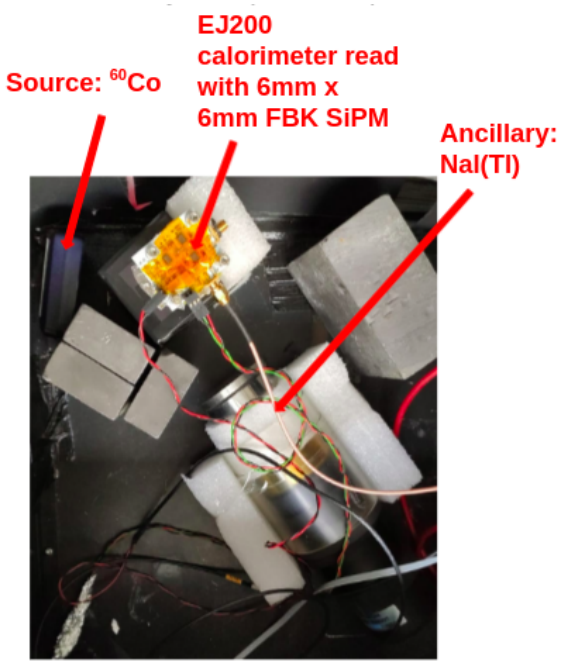

(b)

Figure 4.4: (**a**) Scheme of the Compton measurement setup. (**b**) Setup of the Compton measurement: the blue box on the top left corner contains a ^{60}Co source; the EJ200 calorimeter is on the top of the figure, while the NaI detector is in the center.

As said, the sum of the energy measured in the organic scintillator and in the ancil-

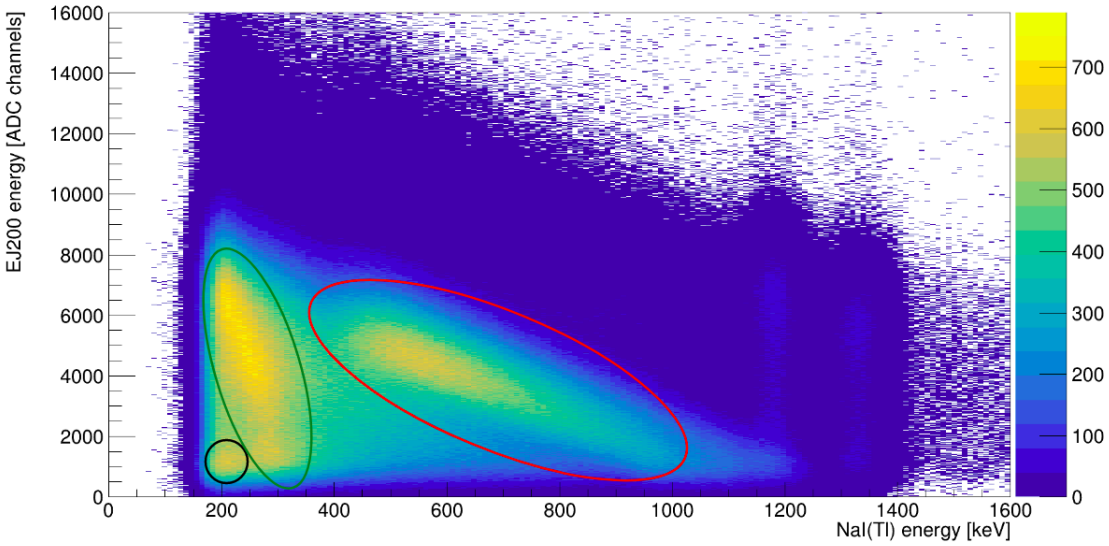

Figure 4.5: Coincidence spectrum between the electron measured in the organic scintillator and the γ detected by the ancillary detector: the red circle highlight the Compton region, while the black and green ones contain low energy background, due to coincidences between background events of both the detectors (black) or between a Compton event detected in the organic scintillator and a spurious background event in the ancillary one (green).

lary detector is constant because of the energy conservation, since $E_\gamma = E'_\gamma + E_{e^-}$. Thus, the Compton events are the ones in the diagonal region (shown in the red circle in figure 4.5) in which this sum is conserved.
At low energy both the organic and the inorganic scintillators present pedestals, because of a not perfect optical coupling. The rate of events belonging to the NaI(Tl) pedestal is quite high, so there are lots of background coincidences between the two pedestals (black circle in figure 4.5).
Moreover, a lot of coincidences between the NaI(Tl) pedestal and Compton events detected in the EJ200 scintillator are present (green region in figure 4.5): this effect is given by an event in which the γ-ray has not been detected, and spurious coincidences between electrons measured in the organic scintillator and noise background measured in the NaI(Tl) are detected. This effect is not visible in the symmetric region of the spectrum with respect to the plane bisector, because the electron freed in the Compton scattering is always measured, so it is not possible to detect the γ ray in the ancillary detector without detecting the electron in the EJ200, i.e. it is not possible to measure a coincidence between high energy detected in the NaI(Tl) and low energy measured in the EJ200.

In order to space out the Compton correlation region from the pedestal region, the source has been placed at wider angles, related to larger E'_γ energies.

Data analysis

The analysis performed is common to all the measurement with the different sources.
The Compton events have been selected by fixing windows on the organic scintillator measured energy, on the ancillary detector measured energy and on the energies sum, in order to select just the events which are part of the Compton line, as shown in figure 4.6.

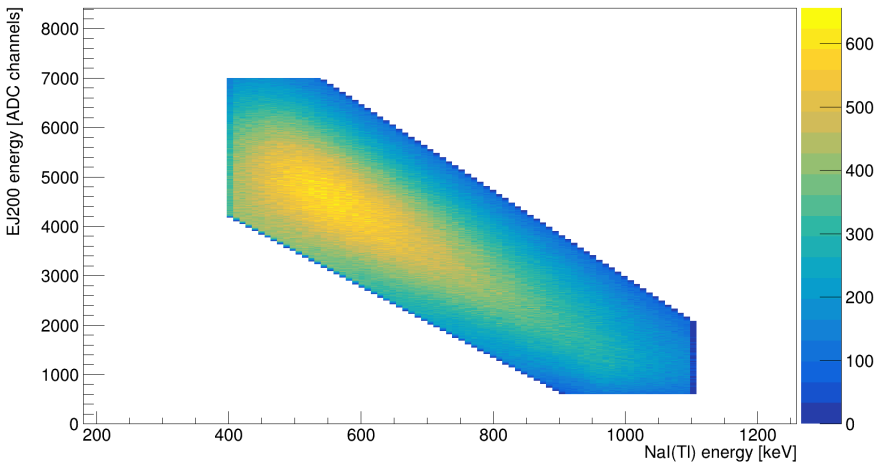

Figure 4.6: Selected events belonging to the Compton region in the coincidence spectrum between the energy measured in the organic calorimeter (expressed in channels) and the one measured in the ancillary inorganic detector (expressed in keV).

The resulting two-dimensional spectrum has been divided in several slices with at different energies measured in the NaI detector, as shown in figure 4.7a. Then, for any slice, the one-dimensional projection on the EJ200 measured energy presents a peak, solving in this way the problem of the absence of a photopeak in the organic scintillator explained in paragraph 4.1.2, and this peak has been fitted with a gaussian (figure 4.7b).
The fit parameters give the centroid and the standard deviation in channels, but the organic detector energy spectrum is not calibrated because of the absence of peaks. However, each peak is related to a specific energy measured in the NaI detector, whose energy spectrum is calibrated conversely to the EJ200 one, so the

energy measured in the organic scintillator is fixed too, because of the conservation of the γ energy. Thus by looking at several projection it is possible to calibrate the EJ200 spectrum too, and to rewrite the centroid and standard deviation values in MeV instead of channels.

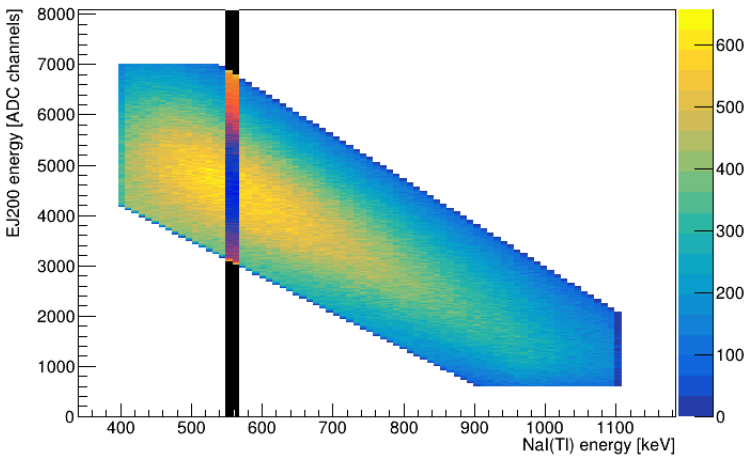

(a)

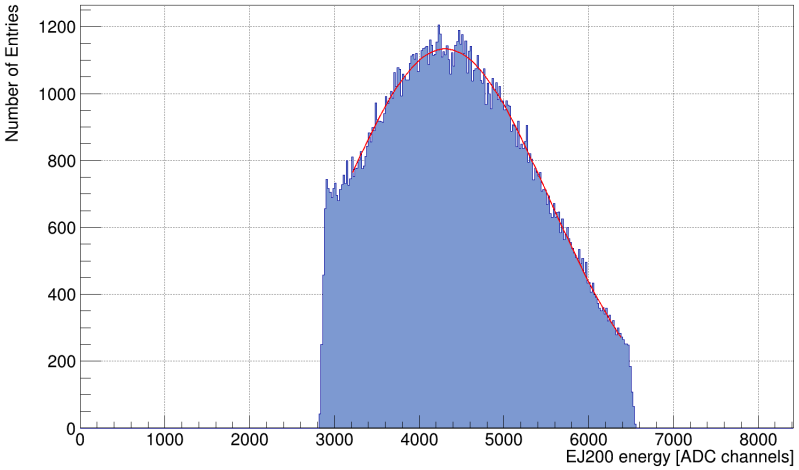

(b)

Figure 4.7: (**a**) Coincidence spectrum slice and (**b**) its projection on the EJ200 energy axis, fitted with a gaussian in order to obtain the resolution of the pseudo-peak obtained with the EJ200 calorimeter for that value of energy measured in the NaI(Tl) detector.

Each peak is now associated to an energy measured in the organic scintillator E

and a standard deviation σ_E: the resolution of each peak is computed as $R = \frac{\sigma_E}{E}$. By plotting the pairs $\left(\frac{1}{R^2}, E\right)$, they are expected to follow a linear trend, as shown in equation 4.3, and the light yield would be given by the slope. As shown in figure 4.8, the central part of the graph follows indeed a linear trend; the sides at high and low energies are not linear because they are related to the regions where the Compton line overlaps with the low energy pedestals in the organic (low energies on the graph) and inorganic (high energies on the graph) detectors.
The linear part is fitted with a line $\frac{1}{R^2} = a + b \cdot E$.

The fit parameters for the analysis performed on the measurement with ^{60}Co are $a = -16.3 \pm 0.5$ *photons* and $b = 35.5 \pm 0.7$ *photons*/MeV.
So, the estimated light yield is $L_y = 35.5 \pm 0.7$ *photons*/MeV.

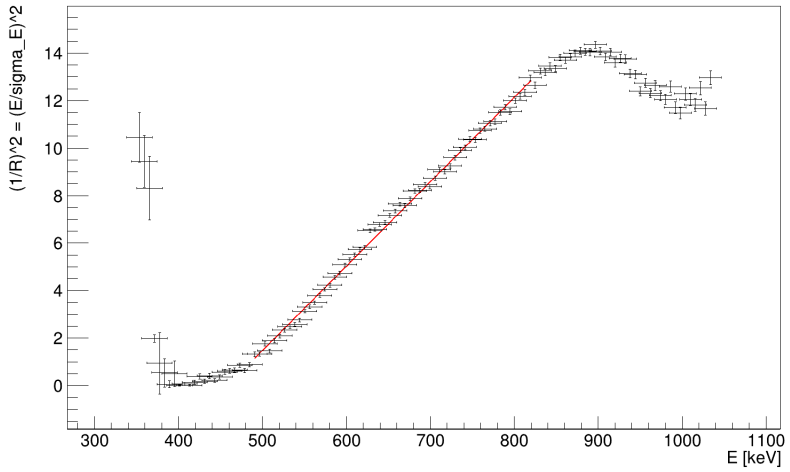

Figure 4.8: Trend of the inverse of the square resolution obtained for several pseudo-photopeaks in the EJ200 calorimeter as a function of the energies they are related to, reading the EJ200 calorimeter with one 6 mm × 6 mm SiPMs..

Compton measurement using 2 SiPMs

The result obtained is affected by the presence of two transitions at energies close one to each other (1173 MeV and 1332 MeV): the pseudo-peaks formed in the EJ200 spectrum associated to the two transitions overlap, giving a poorer resolution than the real one.
In order to obtain a better estimation of the resolution is necessary to use a source emitting γ rays of a single energy, or at energies far to each other.
Another method is to increase the readout area, using more SiPMs or a bigger one: this would increase the light yield, improving the resolution and making possible

to distinguish the two peaks of ^{60}Co.

So, a second SiPM of dimensions 6 mm×6 mm has been added, and the two SiPMs are connected in series. They are now powered with a voltage power supply at 70.2 V, while the other parts of the setup are unchanged.
Improving the resolution the two Compton lines become slightly distinguishable, and projecting the coincidence spectrum at fixed energies measured in the NaI(Tl) detector two pseudo-peaks are obtained instead of one. The analysis described before has been repeated focusing in the region related to the Compton scattering of the 1773 keV γ ray.
The result obtained is $a = -33.7 \pm 0.1$ *photons* and $b = 120 \pm 3$ *photons*/MeV, so the estimated light yield is $L_y = 120 \pm 3$ *photons*/MeV, shown in figure 4.9.
This result is coherent with the expectations: the light yield improved almost of a factor 3.4, where a factor 2 is expected to be gained doubling the area, because of the linearity dependence of the light yield in function of the sensitive area. An additional factor of almost 1.7 is left out by this explanation. However, as explained before, the Compton region in the measurement performed with a single 6 mm × 6 mm is the result of the overlap of two Compton lines, due to the two close transitions of ^{60}Co, besides in this measurement the two peaks have been distinguished; considering that the resolution is proportional to the square root of the light yield, it is sufficient that the resolution improvement granted by the overlap reduction would be of a factor $\sqrt{1.7} \sim 1.3$, that is a reasonable value.

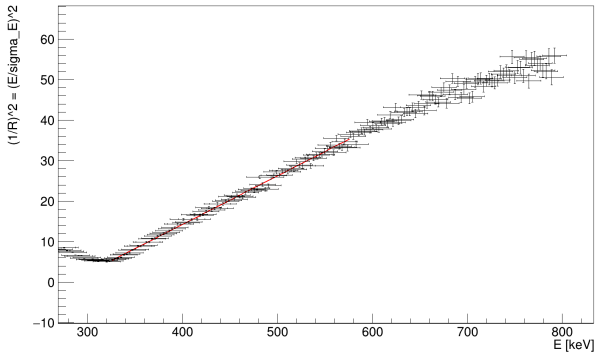

Figure 4.9: Trend of the inverse of the square resolution obtained for several pseudo-photopeaks in the EJ200 calorimeter as a function of the energies they are related to, reading the EJ200 calorimeter with two 6 mm × 6 mm SiPMs.

Light yield dependency as a function of the area

To further improve the previous estimation a new Compton measurement has been done using a SiPM of dimensions 1 cm $\times$ 1 cm.
The 1173 MeV and the 1332 MeV transitions are well distinguished, as it is evident in the coincidence spectrum in figure 4.10.
Repeating the slices method explained before, the peaks of the two transitions appearing in the EJ200 spectrum have been fitted together, as shown in figure 4.11. In this way two light yield values have been obtained for the two transitions, respectively $L_y = 230 \pm 10\ photons/\text{MeV}$ and $L_y = 239 \pm 6\ photons/\text{MeV}$.
The two results are compatible, and their weighted mean has been taken as best estimation of the light yield value: $L_y = 237 \pm 5\ photons/\text{MeV}$.

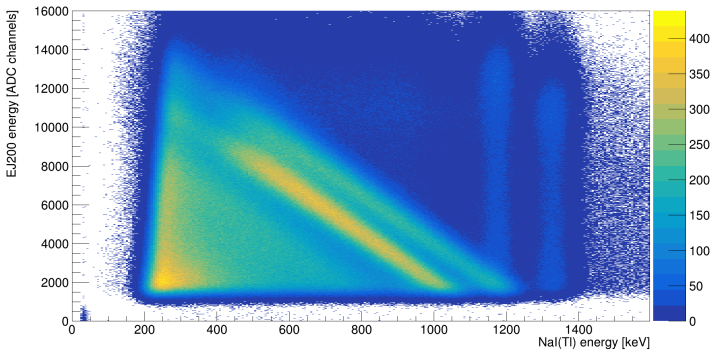

Figure 4.10: Coincidence spectrum between the electron measured in the organic scintillator, read by a 1 cm $\times$ 1 cm SiPM, and the γ detected by the ancillary detector.

The number of photons detected is expected to be proportional to the sensitive area, i.e. the area covered by SiPMs. So the resulting light yield estimated, being an effective value of the light yield dependent on the measuring setup, and not an intrinsic one dependent just on the calorimeter material, is expected to be directly proportional to the area of the SiPM used.
However, this is not the case of these estimation. The non linearity could be due to the improving separation between the 1173 MeV and the 1332 MeV transitions in the different measurements: this decreased the overlap of the two pseudo-peaks obtained and add a further increase in the estimated light yield value. Moreover, the number of photons revealed depends on the optical coupling, so optical couplings different for the different SiPMs could have affected the measurement.

A possibility to improve this estimation and better study the linearity dependence on the sensitive area is, as said, using a source emitting γ-rays at single energies

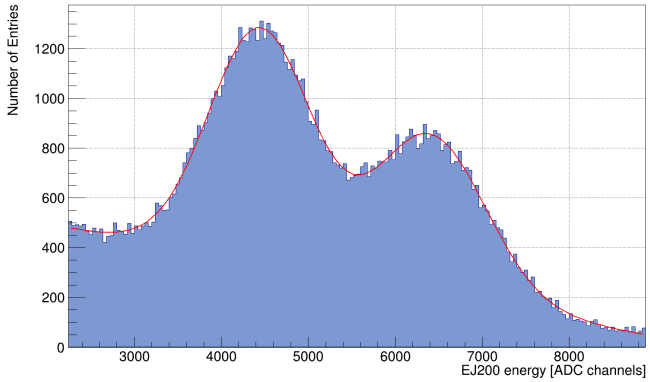

Figure 4.11: Pseudo-peaks generated in the EJ200 spectrum by the projections, at fixed energies measured in the NaI(Tl) detector, of the Compton scattering events of 1173 MeV and the 1332 MeV γ-rays.

or at energies far to each other.

The results of the three tests are gathered in table 4.1.

# Test	A_{SiPM} $[\mathrm{mm}^2]$	L_y $[photons/\mathrm{MeV}]$
1	36	35.5 ± 0.7
2	72	120 ± 3
3	100	237 ± 5

Table 4.1: Light yield values obtained in the measurements done using respectively a single 6 mm $\times$ 6 mm SiPM (**1**), two of dimensions 6 mm $\times$ 6 mm (**2**) and one of dimensions 10 mm $\times$ 10 mm (**3**).

4.2 Characterization of the tracking layer

A characterization of the ΔE layer is also needed, especially in view of the novel redout scheme implemented.
As previously mentioned, the tracking stage is made of two orthogonal segmented layers. In this section the tests performed on a single layer are reported.

4.2.1 Setup description

Each layer is composed by 10 bars of dimension 50 mm $\times$ 5 mm $\times$ 2 mm. The bars are wrapped in white Teflon, with only a 2 mm $\times$ 2 mm window on one of the small sides to allow the coupling with the photo sensor. The group of bars is

read by an array of 10 FBK SiPMs of dimensions 3 mm × 3 mm. The bars and the SiPMs array are placed inside a plastic support properly designed to contain the telescope, as shown in figure 4.12.
The SiPMs have been numbered from 1 to 10 starting from the left extreme in figure 4.12a. They are biased all together using a DC power supply at 34.2 V. A resistive chain distributes the signal produced by each SiPM among the two extremes of the array. The outputs read at the extremes are fed into two preamplifiers, biased with a double voltage at −2.5 V and 2.5 V. The preamplifiers outputs is connected to the CAEN DT5781A digitizer described in paragraph 4.1.2, and proper filters are applied as explained before, in order to correctly acquire the signals.
Since the two signals are expected to be produced by the same event, the signals are acquired only if the two digitizer channels are within a coincidence window of 20 ns.

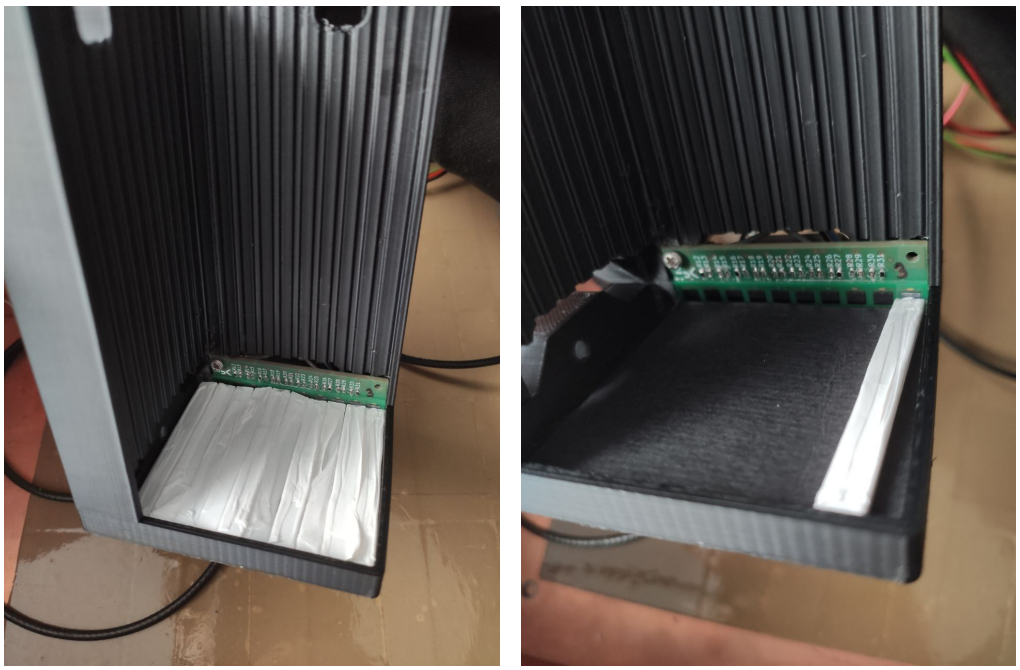

(a) (b)

Figure 4.12: Setup used for estimating the position measurement resolution, respectively using 10 bars (**a**) and 1 bar (**b**).

A ^{60}Co source has been used to perform the characterization.

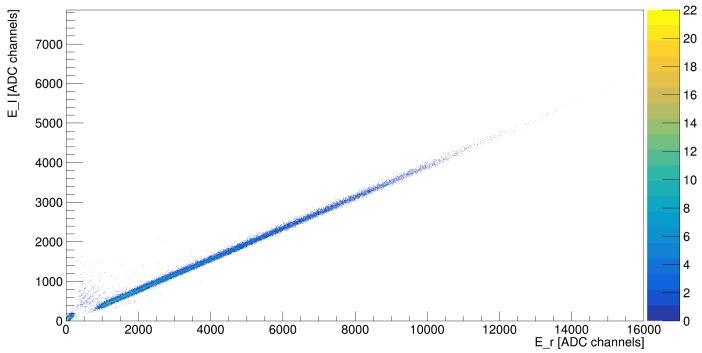

Figure 4.13: Correlation spectrum of (E_r, E_l) signals measured coupling a single EJ200 bar to the 9^{th} SiPM.

4.2.2 Position measurement resolving power

Considering an event where an amount of energy E_{tot} is deposited in the n-th SiPM, and calling E_l and E_r the energies read respectively in the left and right extremes (referring to the previous figure 4.12):

- the total energy deposited in the SiPM is given by $E_{tot} = E_l + E_r$;
- the position measurement, given by the measuring SiPM index, is obtained by the energy asymmetry

$$y = \frac{E_r - E_l}{E_l + E_r} \tag{4.4}$$

The total energy will be used in future to perform an energy resolution characterization and to calibrate the $\Delta E - E$ spectra. For the moment, a set of measurement done using a single bar, coupled to a single SiPM, has been performed.
The coincidence spectrum (E_l, E_r) has been acquired for each position, and the correlation between the events is clear. As an example, the coincidence spectrum related to the SiPM 9 is shown in figure 4.13.

Afterwards, the asymmetry variable y has been plotted, as shown in figure 4.14a. Again, the good discrimination between different positions is evident. Despite the overall result seems correct, representing the asymmetry spectrum in a logarithmic scale, it is possible to observe also the peaks related to the positions that were not coupled to the bar, as shown in figure 4.14b. This effect can be explained in terms of cross-talk between SiPMs, due to a thin epoxy layer deposited over the full SiPM array to protect the wire bonding of each sensor. The resin creates a light path causing a distribution of the light emitted by a bar among all the SiPM. Anyway, since the light emitted by the bars enters the epoxy layer almost

following the bar direction, i.e. almost orthogonally, the light distribution is highly suppressed.

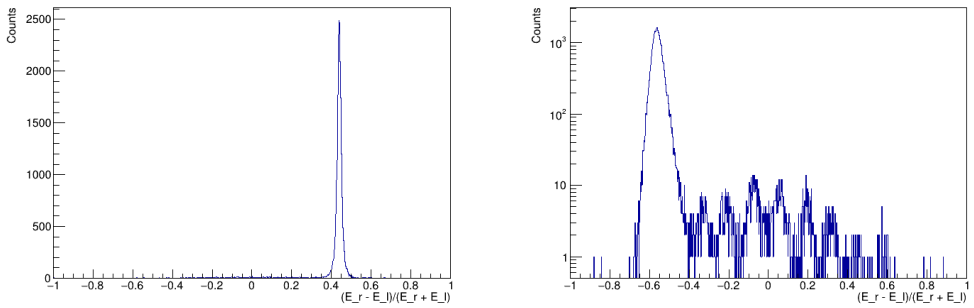

(a) (b)

Figure 4.14: Asymmetry spectrum obtained for signals measured coupling a single scintillator bar to the 9^{th} SiPM, respectively in linear (**a**) and logarithmic scale (**b**).

In order to study the position resolving power, a set of measurements has been performed using more bars.
The thickness of the Teflon envelope used for the tests made it impossible to fit 10 bars in the plastic support prototype. The design, indeed, is based on the dimensions of the bare bars and requires minimum wrapping thickness that will be realized using thin reflective coatings. Therefore, for the purpose of the present test, only 9 bars have been used. A picture of the setup is shown in figure 4.15.

The correlation spectrum and the asymmetry spectrum are shown respectively in figures 4.16a and 4.16b. It is clear that it is possible to discriminate very well the bar detecting an event, and reconstruct with a good resolution the particle position.
Moreover, reducing the cross-talk effects with a new array model, and improving the coupling between bars and SiPMs by using optical gel, the results can improve further.

A good way to evaluate the position information is by plotting the total energy $E_{tot} = E_r + E_l$ against the energy asymmetry, as shown in figure 4.17, and to apply graphical cuts to distinguish the SiPM measuring each event.

The bar coupled to the 5^{th} SiPM is not perfectly aligned, because of the Teflon thickness effects, so part of its light is read by the 6^{th}. This effect is evident in both the correlation and the asymmetry spectra, where respectively the line and the peak associated to the 6^{th} SiPM appear.

Figure 4.15: Setup for characterizing the position resolving power, using 9 bars.

The peaks have been fitted with Gaussian distributions, and the centroid μ_n of the resulting fits has been used to calibrate the asymmetry spectrum to obtain the position value in mm.
The origin of the system has been chosen to be placed between the 5^{th} and the 6^{th} bar, the five bars on the left have been assigned a negative position, and the five on the right a positive one.
Thus, being the bars 5 mm wide, the first bar has been assigned the position $x_1 = -2.25$ mm, the second one $x_2 = -1.75$ mm, and so on. The error associated to the x_n values is the error associated to a uniform distribution in an interval of 5 mm, namely $\sigma_x = \frac{5}{\sqrt{12}}$ mm.
The (μ_n, x_n) pairs have been fitted with a linear function $x_n = a + b \cdot \mu_n$, as shown in figure 4.18, and the best fit parameters are $a = 0.02 \pm 0.5$ mm and $b = 4 \pm 1$ mm.

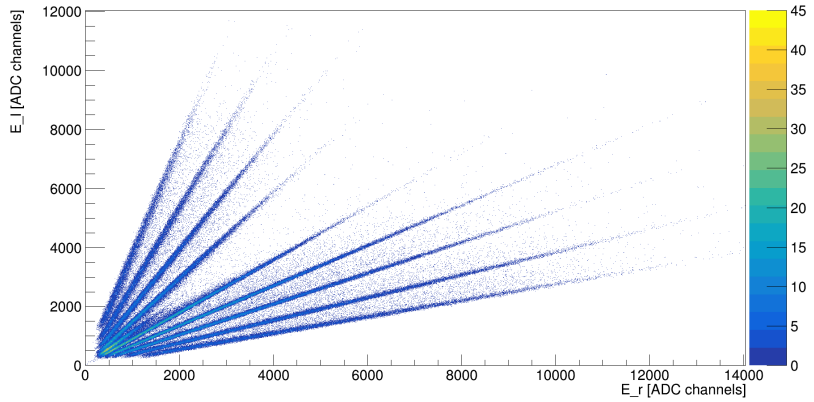

(a)

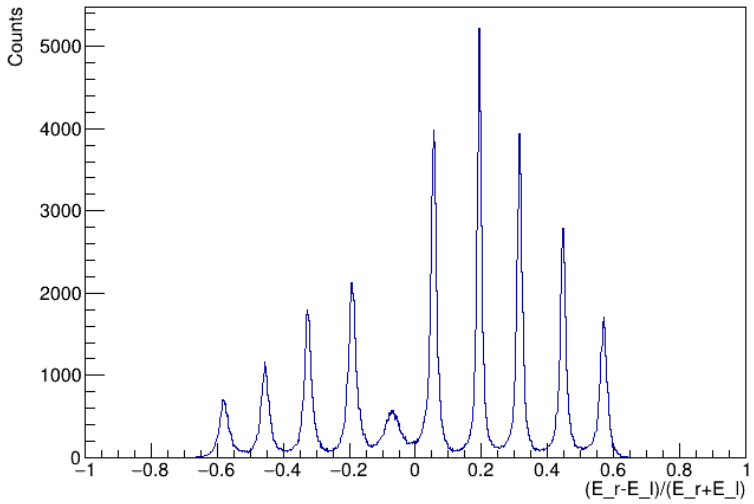

(b)

Figure 4.16: Correlation (**a**) and asymmetry (**b**) spectra obtained by the signals E_r and E_l measured using 9 scintillator bars coupled to 9 SiPMs.

4.3 Invariant mass reconstruction and resolution

The presence of the resonant boson would lead to a structure in the invariant mass distribution of the detected pairs, as well as in the distribution of the correlation angle between the leptons, as shown in figures 2.10 and 2.12b.
Thus, it is necessary to compute the expected resolution for the invariant mass reconstruction.

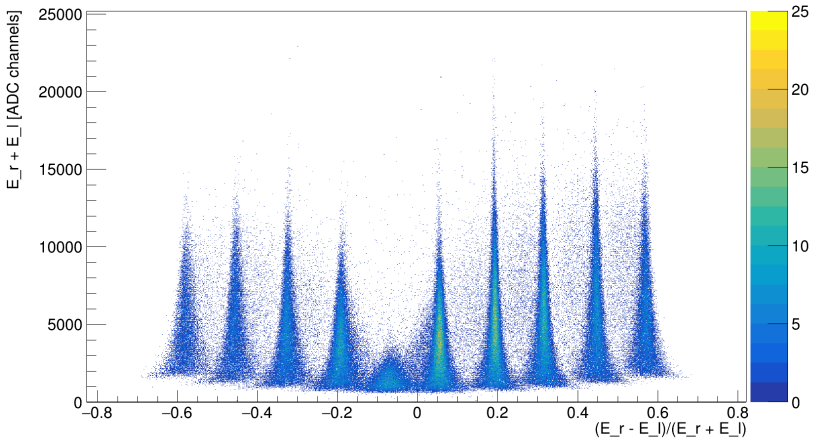

Figure 4.17: Correlation of the total energy $E_l + E_r$ against the energy asymmetry $(E_r - E_l) / (E_r + E_l)$.

If we consider an electron and a positron, respectively with energy and momentum $(E_-, \vec{p}_-)$ and $(E_+, \vec{p}_+)$.
The square of the invariant mass of such a pair is:

$$\begin{aligned} M^2 = s &= (E_+ + E_-, \vec{p}_+ + \vec{p}_-)^2 \\ &= E_+^2 + E_-^2 + 2E_+E_- - |\vec{p}_+|^2 - |\vec{p}_-|^2 - 2\cos\theta|\vec{p}_+||\vec{p}_-| \\ &= 2m_e^2 + 2E_+E_- - 2\cos\theta\sqrt{E_+^2 - m_e^2}\sqrt{E_-^2 - m_e^2} \end{aligned} \tag{4.5}$$

So the invariant mass depends on three parameters, i.e. the electron and positron energies and the correlation angle.

The error associated to M^2 can be computed as:

$$\begin{aligned} \sigma_s^2 = \sigma_{E_+}^2 &\left(2E_- + 2\cos\theta \frac{E_+}{\sqrt{E_+^2 - m_e^2}} \cdot \sqrt{E_-^2 - m_e^2} \right)^2 \\ + \sigma_{E_-}^2 &\left(2E_+ + 2\cos\theta \frac{E_-}{\sqrt{E_-^2 - m_e^2}} \cdot \sqrt{E_+^2 - m_e^2} \right)^2 \\ + \sigma_\theta^2 \cdot 4 &\left(E_+^2 - m_e^2\right)\left(E_-^2 - m_e^2\right)\sin^2\theta \end{aligned} \tag{4.6}$$

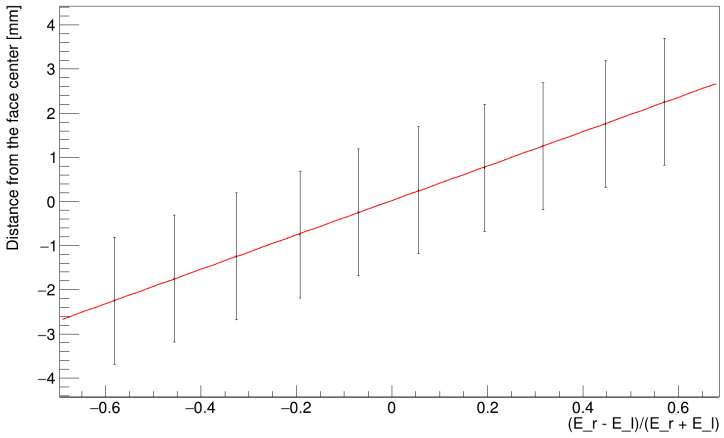

Figure 4.18: Calibration of the asymmetry spectrum to obtain a position in mm.

Finally, having $M = \sqrt{s}$, its error will be $\sigma_M = \frac{\sigma_s}{2s}$.

This error depends on six terms: $E_+, E_-, \sigma_{E_+}, \sigma_{E_-}, \theta$ and σ_θ.
Two degrees of freedom, though, can be absorbed exploiting the knowledge on the detector's resolution. Indeed, as explained in paragraph 4.1.1:

$$\sigma_E^2 = Ly \cdot E \tag{4.7}$$

and the positron energy is fixed by the electron one and the resonance energy.

Therefore, the error associated to the squared invariant mass depends on the electron energy, on the light yield of the detector, on the correlation angle and on the angular resolution.
The two terms that will be fixed in the experiment will be the light yield and the resolution, while electrons and positrons will carry a continuous range of kinetic energies, and the correlation angle is obviously not fixed.
To estimate the resolution on the invariant mass reconstruction for different values of light yield and angular resolution, the invariant mass and its error have been computed for a wide range of values of the four parameters described. The light yield has been varied between $Ly = 20\ photons/\text{MeV}$ and $Ly = 120\ photons/\text{MeV}$ with steps of 0.1 $photons/\text{MeV}$; the angular resolution has been varied between $\sigma_\theta = \left(\frac{1.5}{\sqrt{12}}\right)^\circ$ and $\sigma_\theta = \left(\frac{3.6}{\sqrt{12}}\right)^\circ$ in steps of $\left(\frac{0.1}{\sqrt{12}}\right)^\circ$; the correlation angle has been varied between $\theta = 0^\circ$ and $\theta = 180^\circ$ in steps of 0.2°, and the electron energy between $E_- = \frac{1}{4} \cdot 18.15$ MeV and $E_- = \frac{3}{4} \cdot 18.15$ MeV, with steps of 0.075 MeV.
This allows to compute a distribution in a form $f(Ly, \sigma_\theta, E_+, E_-, \theta)$. In order to

obtain a distribution depending only on the parameters that could be fixed in the experiment, namely the light yield and the angular resolution, the energies and *theta* have been marginalized, or integrated out.
This means that a new distribution has been computed as a weighted average on the parameters to be marginalized:

$$f(Ly, \sigma_\theta) = \frac{\sum_{E_-,\theta} f(Ly, \sigma_\theta, E_-, \theta)}{(E_-^{max} - E_-^{min})(\theta^{max} - \theta^{min})} \tag{4.8}$$

The result is shown in figures 4.6 and 4.19b, representing respectively the distribution $\sigma_{M_{e^+e^-}}(Ly, \sigma_\theta)$ and $R_{M_{e^+e^-}}(Ly, \sigma_\theta)$, where $R_{M_{e^+e^-}} = \frac{\sigma_{M_{e^+e^-}}}{M_{e^+e^-}}$.

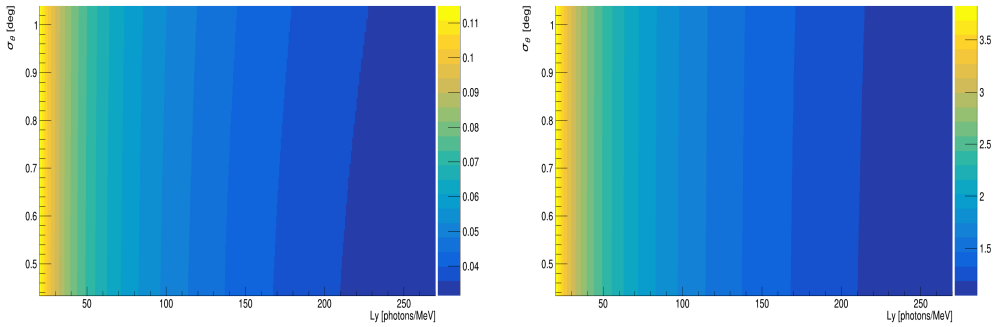

(a) (b)

Figure 4.19: (**a**) Invariant mass error and (**b**) resolution represented by the color palette as a function of the telescopes light yield and the spectrometer angular resolution.

It is worth noticing that the resolution on the reconstructed invariant mass varies more varying the light yield than the angular resolution in the respective ranges. Thus, although it would be important to have a good angular resolution to observe the peak in the correlation angle distribution, it would be more important in order to estimate the invariant mass to reach a good energy resolution and light yield for the final result.

With the light yield obtained on this work that is $L_y = 237 \pm 5$ *photons*/MeV in the best case ((see paragraphs 4.1.2), the expected invariant mass resolution related to the statistical errors is of the order of $\sigma_{M_{e^+e^-}}/M_{e^+e^-} \sim 1\%$.

Conclusion and outlook

Striking anomalies in the relative angle distribution of electron-positron pairs produced by internal pair creation in the decay of $^8Be^*$ and $^4He^*$ have been recently reported. The series of experiments was carried out at the Atomki laboratory (Debrecen, Hungary). The first results concerned the decay of the 18.15 MeV 1^+ state in ^{8}Be [1], while the group later focused on the $\approx$ 20 MeV excited states in ^{4}He [2]. Both results are compatible with the creation and subsequent decay of a 17 MeV particle, named "X17", whose properties need better investigation.

The experimental results triggered dedicated theoretical efforts: J. Feng and collaborators further explored the X17 boson interpretation and evaluated its possible coupling to ordinary matter [16]; conversely, X. Zhang and G. Miller developed more conventional approaches within the nuclear physics framework [18].

In addition to a comprehensive modeling of the phenomenon, an independent verification of the observed anomalies is clearly needed. At this purpose, a new experimental setup is being developed at the INFN Legnaro National Laboratories of INFN (Legnaro, Padova, Italy). The first goal is to provide a replica of the Hungarian experiment with an updated setup and this thesis work focused on its design, simulation and characterization. The proposed layout is constituted by an array of $\Delta E - E$ telescopes gathered in groups of four. Each telescope is composed by three layers of plastic scintillation detectors: the first two (2 mm thick) are segmented in orthogonal directions and provide position and energy loss information while the third one (10 cm thick) is big enough to absorb the particles and measure the remaining energy. The detector's dimensions have been optimized with the aim of improving the angular resolution being, at the same time, capable of completely absorbing 20 MeV electrons and positrons. The telescopes are read out by Silicon PhotoMultipliers (SiPMs), allowing the future capability of coupling to a magnetic field. The bars are read out by an array of SiPM, for which an innovative readout scheme is proposed. The full detector will be placed in vacuum, close to the reaction target, in order to minimize the material budget

before the detectors.

In this thesis work, the geant4 simulation of the full setup and the data analysis code for the particle's tracking needed to measure and discriminate e^+e^- pairs was developed. The overall consistency with the published results in terms of global efficiency of the setup has been analyzed together with the main features of the proposed arrangement. In particular, the results presented in paragraph 3.3.4 detail the expected detection efficiency and resolution. Moreover, a preliminary γ background characterization has been performed. The pair production to gamma decay ratio is expected to be of the order of 10^{-6}, therefore an optimal gamma background suppression is mandatory. According to the simulated data, the non zero probability of triple gamma coincidences in one telescope, possibly leading to a wrong particle identification, is strongly suppressed when the coincidence of two detectors is required. Clearly this effect will depend on the reaction rate and actual background condition at the experiment location. Therefore, dedicated background measurements will be performed.

The thesis work later focused on the experimental characterization of the first detector's prototypes. The energy resolution achievable using different models and arrangements of SiPMs has been discussed in paragraph 4.1.2 and the consequent effect on the invariant mass resolution is described in paragraph 4.3. The results show that the proposed setup allows to properly address the ^8Be case. At last, the first position reconstruction tests have been performed by measuring the response of the scintillating tiles to gamma radiation through an array of SiPMs read out by a custom electronic board.

In the next future in-beam tests will be exploited for a full characterization of the setup. The 6.05 MeV E0 transition from the $^{19}F\left(p,\alpha e^+e^-\right)^{16}He$ reaction will be used as standard test bench for the setup commissioning. The simulation will be improved too, by introducing the physics modeling of the IPC process and by adding experimental details for a more realistic simulation that allows to better characterize any possible source of background.

Bibliography

[1] A. J. Krasznahorkay, M. Csatlós, L. Csige, Z. Gácsi, J. Gulyás, M. Hunyadi, I. Kuti, B. M. Nyakó, L. Stuhl, J. Timár, T. G. Tornyi, Z. Vajta, T. J. Ketel, and A. Krasznahorkay, "Observation of anomalous internal pair creation in ^{8}Be: A possible indication of a light, neutral boson," *Phys. Rev. Lett.*, vol. 116, p. 042501, Jan 2016.

[2] A. J. Krasznahorkay, M. Csatlos, L. Csige, J. Gulyas, M. Koszta, B. Szihalmi, J. Timar, D. S. Firak, A. Nagy, N. J. Sas, and A. Krasznahorkay, "New evidence supporting the existence of the hypothetic x17 particle," 2019.

[3] K. S. Krane, *Introductory nuclear physics*. New York, NY: Wiley, 1988.

[4] Available online.
https://slideplayer.it/slide/577909/.

[5] P. Schlüter, G. Soff, and W. Greiner, "Pair creation by internal conversion," *Phys. Rept.*, vol. 75, no. 6, pp. 327–392, 1981.

[6] P. Schlüter and G. Soff, "Total and differential conversion coefficients for internal electron-positron pair creation," *Atomic Data and Nuclear Data Tables*, vol. 24, no. 6, pp. 509–571, 1979.

[7] M. E. Rose, "Internal pair formation," *Phys. Rev.*, vol. 76, pp. 678–681, Sep 1949.

[8] G. Goldring, "Internal pairs in anisotropic emission," *Proceedings of the Physical Society. Section A*, vol. 66, pp. 341–345, apr 1953.

[9] S. Devons and G. Goldring, "Emission of electron-positron pairs from light nuclei II: -transitions in8be,10b and16o," *Proceedings of the Physical Society. Section A*, vol. 67, pp. 413–420, may 1954.

[10] J. Gulyás, T. Ketel, A. Krasznahorkay, M. Csatlós, L. Csige, Z. Gácsi, M. Hunyadi, A. Krasznahorkay, A. Vitéz, and T. Tornyi, "A pair spectrometer for measuring multipolarities of energetic nuclear transitions," *Nuclear Instruments and Methods in Physics Research, Section A: Accelerators, Spectrometers, Detectors and Associated Equipment*, vol. 808, pp. 21–28, 2 2016.

[11] A. Buda, J. C. Bacelar, A. Balanda, H. van der Ploeg, Z. Sujkowski, and A. van der Woude, "Positron-electron decay of ^{28}Si at an excitation energy of 50 MeV," *Nuclear Physics A*, vol. 553, pp. 509–513, mar 1993.

[12] K. E. Stiebing, F. W. N. de Boer, O. Fröhlich, H. Bokemeyer, K. A. Müller, K. Bethge, and J. van Klinken, "A multi-detector array for high energy nuclear $e^+ - e^-$ pair spectroscopy," *Journal of Physics G: Nuclear and Particle Physics*, vol. 30, pp. 165–180, jan 2004.

[13] F. W. N. de Boer *et al.*, "A deviation in internal pair conversion," *Phys. Lett. B*, vol. 388, pp. 235–240, 1996.

[14] F. deBoer, R. vanDantzig, J. vanKlinken, K. Bethge, H. Bokemeyer, A. Buda, K. Muller, and K. Stiebing, "Excess in nuclear e(+)e(-) pairs near 9 mev/c(2) invariant mass," *Journal of Physics. G: Nuclear and Particle Physics*, vol. 23, pp. L85–L96, Nov. 1997.

[15] F. W. N. d. Boer, K. Bethge, H. Bokemeyer, R. v. Dantzig, J. v. Klinken, V. Mironov, K. A. Müller, and K. E. Stiebing, "Further search for a neutral boson with a mass around 9 mev/c2," *Journal of Physics G: Nuclear and Particle Physics*, vol. 27, p. L29–L40, Mar 2001.

[16] J. L.Feng, B. Fornal, I. Galon, S. Gardner, J. Smolinsky, T. Tate, and P. Tanedo, "Evidence for a protophobic fifth force from 8be nuclear transitions," 04 2016.

[17] J. L.Feng, B. Fornal, I. Galon, S. Gardner, J. Smolinsky, T. Tate, and P. Tanedo, "Particle physics models for the 17 mev anomaly in beryllium nuclear decays," *Physical Review D*, vol. 95, 04 2016.

[18] X. Zhang and G. A. Miller, "Can nuclear physics explain the anomaly observed in the internal pair production in the beryllium-8 nucleus?," *Physics Letters B*, vol. 773, pp. 159 – 165, 2017.

[19] X. Zhang and G. A. Miller, "Can a protophobic vector boson explain the atomki anomaly?," *Physics Letters B*, vol. 813, p. 136061, 2021.

[20] Available online. http://www.tunl.duke.edu/nucldata/figures/08figs/menu08.shtml.

[21] D. Tilley, H. Weller, and G. Hale, "Energy levels of light nuclei a = 4," *Nuclear Physics A*, vol. 541, no. 1, pp. 1–104, 1992.

[22] J. Balewski, J. Bernauer, J. Bessuille, R. Corliss, R. Cowan, C. Epstein, P. Fisher, D. Hasell, E. Ihloff, Y. Kahn, J. Kelsey, R. Milner, S. Steadman, J. Thaler, C. Tschalaer, C. Vidal, S. Benson, J. Boyce, D. Douglas, P. Evtushenko, C. Hernandez-Garcia, C. Keith, C. Tennant, S. Zhang, R. Alarcon, D. Blyth, R. Dipert, L. Ice, G. Randall, B. Dongwi, N. Kalantarians, M. Kohl, A. Liyanage, J. Nazeer, M. Garcon, R. Cervantes, K. Dehmelt, A. Deshpande,

N. Feege, and B. Surrow, "The darklight experiment: A precision search for new physics at low energies," 2014.

[23] O. Moreno, "The heavy photon search experiment at jefferson lab," 2013.

[24] P. Ilten, J. Thaler, M. Williams, and W. Xue, "Dark photons from charm mesons at lhcb," *Phys. Rev. D*, vol. 92, p. 115017, Dec 2015.

[25] T. Beranek, H. Merkel, and M. Vanderhaeghen, "Theoretical framework to analyze searches for hidden light gauge bosons in electron scattering fixed target experiments," *Physical Review D*, vol. 88, Jul 2013.

[26] B. Echenard, R. Essig, and Y.-M. Zhong, "Projections for dark photon searches at mu3e," *Journal of High Energy Physics*, vol. 2015, Jan 2015.

[27] B. Wojtsekhowski, D. Nikolenko, and I. Rachek, "Searching for a new force at vepp-3," 2012.

[28] S. Gardner, R. Holt, and A. Tadepalli, "New prospects in fixed target searches for dark forces with the seaquest experiment at fermilab," *Physical Review D*, vol. 93, Jun 2016.

[29] S. Collaboration, M. Anelli, S. Aoki, G. Arduini, J. J. Back, A. Bagulya, W. Baldini, A. Baranov, G. J. Barker, S. Barsuk, M. Battistin, J. Bauche, A. Bay, V. Bayliss, L. Bellagamba, G. Bencivenni, M. Bertani, O. Bezshyyko, D. Bick, N. Bingefors, A. Blondel, M. Bogomilov, A. Boyarsky, D. Bonacorsi, D. Bondarenko, W. Bonivento, J. Borburgh, T. Bradshaw, R. Brenner, D. Breton, N. Brook, M. Bruschi, A. Buonaura, S. Buontempo, S. Cadeddu, A. Calcaterra, M. Calviani, M. Campanelli, C. Capoccia, A. Cecchetti, A. Chatterjee, J. Chauveau, A. Chepurnov, M. Chernyavskiy, P. Ciambrone, C. Cicalo, G. Conti, K. Cornelis, M. Courthold, M. G. Dallavalle, N. D'Ambrosio, G. D. Lellis, M. D. Serio, L. Dedenko, A. D. Crescenzo, N. D. Marco, C. Dib, J. Dietrich, H. Dijkstra, D. Domenici, S. Donskov, D. Druzhkin, J. Ebert, U. Egede, A. Egorov, V. Egorychev, M. A. E. Alaoui, T. Enik, A. Etenko, F. Fabbri, L. Fabbri, G. Fedorova, G. Felici, M. Ferro-Luzzi, R. A. Fini, M. Franke, M. Fraser, G. Galati, B. Giacobbe, B. Goddard, L. Golinka-Bezshyyko, D. Golubkov, A. Golutvin, D. Gorbunov, E. Graverini, J.-L. Grenard, A. M. Guler, C. Hagner, H. Hakobyan, J. C. Helo, E. van Herwijnen, D. Horvath, M. Iacovacci, G. Iaselli, R. Jacobsson, I. Kadenko, M. Kamiscioglu, C. Kamiscioglu, G. Khaustov, A. Khotjansev, B. Kilminster, V. Kim, N. Kitagawa, K. Kodama, A. Kolesnikov, D. Kolev, M. Komatsu, N. Konovalova, S. Koretskiy, I. Korolko, A. Korzenev, S. Kovalenko, Y. Kudenko, E. Kuznetsova, H. Lacker, A. Lai, G. Lanfranchi, A. Lauria, H. Lebbolo, J. M. Levy, L. Lista, P. Loverre, A. Lukiashin, V. E. Lyubovitskij, A. Malinin, M. Manfredi, A. Perillo-Marcone, A. Marrone, R. Matev, E. N. Messomo, P. Mermod, S. Mikado, Y. Mikhaylov, J. Miller, D. Milstead, O. Mineev, R. Mingazheva,

G. Mitselmakher, M. Miyanishi, P. Monacelli, A. Montanari, M. C. Montesi, G. Morello, K. Morishima, S. Movtchan, V. Murzin, N. Naganawa, T. Naka, M. Nakamura, T. Nakano, N. Nurakhov, B. Obinyakov, K. Ocalan, S. Ogawa, V. Oreshkin, A. Orlov, J. Osborne, P. Pacholek, J. Panman, A. Paoloni, L. Paparella, A. Pastore, M. Patel, K. Petridis, M. Petrushin, M. Poli-Lener, N. Polukhina, V. Polyakov, M. Prokudin, G. Puddu, F. Pupilli, F. Rademakers, A. Rakai, T. Rawlings, F. Redi, S. Ricciardi, R. Rinaldesi, T. Roganova, A. Rogozhnikov, H. Rokujo, A. Romaniouk, G. Rosa, I. Rostovtseva, T. Rovelli, O. Ruchayskiy, T. Ruf, G. Saitta, V. Samoylenko, V. Samsonov, A. S. Ull, A. Saputi, O. Sato, W. Schmidt-Parzefall, N. Serra, S. Sgobba, M. Shaposhnikov, P. Shatalov, A. Shaykhiev, L. Shchutska, V. Shevchenko, H. Shibuya, Y. Shitov, S. Silverstein, S. Simone, M. Skorokhvatov, S. Smirnov, E. Solodko, V. Sosnovtsev, R. Spighi, M. Spinetti, N. Starkov, B. Storaci, C. Strabel, P. Strolin, S. Takahashi, P. Teterin, V. Tioukov, D. Tommasini, D. Treille, R. Tsenov, T. Tshchedrina, A. Ustyuzhanin, F. Vannucci, V. Venturi, M. Villa, H. Vincke, H. Vincke, M. Vladymyrov, S. Xella, M. Yalvac, N. Yershov, D. Yilmaz, A. U. Yilmazer, G. Vankova-Kirilova, Y. Zaitsev, and A. Zoccoli, "A facility to search for hidden particles (ship) at the cern sps," 2015.

[30] J. L. Feng, T. M. Tait, and C. B. Verhaaren, "Dynamical evidence for a fifth force explanation of the atomki nuclear anomalies," *Physical Review D*, vol. 102, Aug 2020.

[31] M. Viviani, E. Filandri, L. Girlanda, C. Gustavino, A. Kievsky, L. E. Marcucci, and R. Schiavilla, "The x17 boson and the $^3\mathrm{h}(p, e^+e^-)^4\mathrm{he}$ and $^3\mathrm{he}(n, e^+e^-)^4\mathrm{he}$ processes: a theoretical analysis," 2021.

[32] B. Koch, "X17: A new force, or evidence for a hard $\gamma + \gamma$ process?," *Nuclear Physics A*, vol. 1008, p. 122143, 2021.

[33] S. N. Ahmed, "2 - interaction of radiation with matter," in *Physics and Engineering of Radiation Detection (Second Edition)* (S. N. Ahmed, ed.), pp. 65 – 155, Elsevier, second edition ed., 2015.

[34] Y. Shibamoto, A. Miyakawa, H. Iwata, and S. Otsuka, *Radiobiology of SBRT*, pp. 11–25. 08 2015.

[35] Available online.
https://commons.wikimedia.org.

[36] V. Venugopal and P. Bhagdikar, "de broglie wavelength and frequency of scattered electrons in the compton effect," *Physics Education*, vol. 29, p. 35, 03 2013.

[37] Available online.
https://eljentechnology.com/products/plastic-scintillators/ej-200-ej-204-ej-208-ej-212.

[38] R. Bolzonella, "Preparazione di un esperimento per la misura di coppie e^+e^- nel decadimento del $^8be^*$," 09 2019.

[39] J. S. F. Salvat, J.M. Fernàndez-Varea, *PENELOPE-2011: A Code System for Monte Carlo Simulation of Electron and Photon Transport.*

[40] S. Agostinelli, J. Allison, K. Amako, J. Apostolakis, H. Araujo, P. Arce, M. Asai, D. Axen, S. Banerjee, G. Barrand, F. Behner, L. Bellagamba, J. Boudreau, L. Broglia, A. Brunengo, H. Burkhardt, S. Chauvie, J. Chuma, R. Chytracek, G. Cooperman, G. Cosmo, P. Degtyarenko, A. Dell'Acqua, G. Depaola, D. Dietrich, R. Enami, A. Feliciello, C. Ferguson, H. Fesefeldt, G. Folger, F. Foppiano, A. Forti, S. Garelli, S. Giani, R. Giannitrapani, D. Gibin, J. Gómez Cadenas, I. González, G. Gracia Abril, G. Greeniaus, W. Greiner, V. Grichine, A. Grossheim, S. Guatelli, P. Gumplinger, R. Hamatsu, K. Hashimoto, H. Hasui, A. Heikkinen, A. Howard, V. Ivanchenko, A. Johnson, F. Jones, J. Kallenbach, N. Kanaya, M. Kawabata, Y. Kawabata, M. Kawaguti, S. Kelner, P. Kent, A. Kimura, T. Kodama, R. Kokoulin, M. Kossov, H. Kurashige, E. Lamanna, T. Lampén, V. Lara, V. Lefebure, F. Lei, M. Liendl, W. Lockman, F. Longo, S. Magni, M. Maire, E. Medernach, K. Minamimoto, P. Mora de Freitas, Y. Morita, K. Murakami, M. Nagamatu, R. Nartallo, P. Nieminen, T. Nishimura, K. Ohtsubo, M. Okamura, S. O'Neale, Y. Oohata, K. Paech, J. Perl, A. Pfeiffer, M. Pia, F. Ranjard, A. Rybin, S. Sadilov, E. Di Salvo, G. Santin, T. Sasaki, N. Savvas, Y. Sawada, S. Scherer, S. Sei, V. Sirotenko, D. Smith, N. Starkov, H. Stoecker, J. Sulkimo, M. Takahata, S. Tanaka, E. Tcherniaev, E. Safai Tehrani, M. Tropeano, P. Truscott, H. Uno, L. Urban, P. Urban, M. Verderi, A. Walkden, W. Wander, H. Weber, J. Wellisch, T. Wenaus, D. Williams, D. Wright, T. Yamada, H. Yoshida, and D. Zschiesche, "Geant4—a simulation toolkit," *Nuclear Instruments and Methods in Physics Research Section A: Accelerators, Spectrometers, Detectors and Associated Equipment*, vol. 506, no. 3, pp. 250–303, 2003.

[41] J. Allison, K. Amako, J. Apostolakis, H. Araujo, P. Arce Dubois, M. Asai, G. Barrand, R. Capra, S. Chauvie, R. Chytracek, G. Cirrone, G. Cooperman, G. Cosmo, G. Cuttone, G. Daquino, M. Donszelmann, M. Dressel, G. Folger, F. Foppiano, J. Generowicz, V. Grichine, S. Guatelli, P. Gumplinger, A. Heikkinen, I. Hrivnacova, A. Howard, S. Incerti, V. Ivanchenko, T. Johnson, F. Jones, T. Koi, R. Kokoulin, M. Kossov, H. Kurashige, V. Lara, S. Larsson, F. Lei, O. Link, F. Longo, M. Maire, A. Mantero, B. Mascialino, I. McLaren, P. Mendez Lorenzo, K. Minamimoto, K. Murakami, P. Nieminen, L. Pandola, S. Parlati, L. Peralta, J. Perl, A. Pfeiffer, M. Pia, A. Ri-

bon, P. Rodrigues, G. Russo, S. Sadilov, G. Santin, T. Sasaki, D. Smith, N. Starkov, S. Tanaka, E. Tcherniaev, B. Tome, A. Trindade, P. Truscott, L. Urban, M. Verderi, A. Walkden, J. Wellisch, D. Williams, D. Wright, and H. Yoshida, "Geant4 developments and applications," *IEEE Transactions on Nuclear Science*, vol. 53, no. 1, pp. 270–278, 2006.

[42] J. Allison, K. Amako, J. Apostolakis, P. Arce, M. Asai, T. Aso, E. Bagli, A. Bagulya, S. Banerjee, G. Barrand, B. Beck, A. Bogdanov, D. Brandt, J. Brown, H. Burkhardt, P. Canal, D. Cano-Ott, S. Chauvie, K. Cho, G. Cirrone, G. Cooperman, M. Cortés-Giraldo, G. Cosmo, G. Cuttone, G. Depaola, L. Desorgher, X. Dong, A. Dotti, V. Elvira, G. Folger, Z. Francis, A. Galoyan, L. Garnier, M. Gayer, K. Genser, V. Grichine, S. Guatelli, P. Guèye, P. Gumplinger, A. Howard, I. Hřivnáčová, S. Hwang, S. Incerti, A. Ivanchenko, V. Ivanchenko, F. Jones, S. Jun, P. Kaitaniemi, N. Karakatsanis, M. Karamitros, M. Kelsey, A. Kimura, T. Koi, H. Kurashige, A. Lechner, S. Lee, F. Longo, M. Maire, D. Mancusi, A. Mantero, E. Mendoza, B. Morgan, K. Murakami, T. Nikitina, L. Pandola, P. Paprocki, J. Perl, I. Petrović, M. Pia, W. Pokorski, J. Quesada, M. Raine, M. Reis, A. Ribon, A. Ristić Fira, F. Romano, G. Russo, G. Santin, T. Sasaki, D. Sawkey, J. Shin, I. Strakovsky, A. Taborda, S. Tanaka, B. Tomé, T. Toshito, H. Tran, P. Truscott, L. Urban, V. Uzhinsky, J. Verbeke, M. Verderi, B. Wendt, H. Wenzel, D. Wright, D. Wright, T. Yamashita, J. Yarba, and H. Yoshida, "Recent developments in geant4," *Nuclear Instruments and Methods in Physics Research Section A: Accelerators, Spectrometers, Detectors and Associated Equipment*, vol. 835, pp. 186–225, 2016.

[43] Available online. https://geant4-userdoc.web.cern.ch/UsersGuides/IntroductionToGeant4/fo/IntroductionToGeant4.pdf.

[44] Available online. https://geant4-userdoc.web.cern.ch/UsersGuides/AllGuides/html/index.html.

[45] Available online. https://www.bogotobogo.com/Algorithms/uniform_distribution_sphere.php.

[46] R. Basko, G. Zeng, and G. Gullberg, "Application of spherical harmonics to image reconstruction for the compton camera," *Physics in medicine and biology*, vol. 43, pp. 887–94, 04 1998.

A

Appendix

A.1 Isotropic particle emission

In this section the method used to generate particles emitted isotropically will be explained.
The isotropic emission of electrons and positrons is based on the uniform distribution of points on a spherical surface.

To distribute points uniformly on the surface of a sphere, the first idea could be to use uniform distributions of θ and ϕ respectively in $[0, 2\pi)$ and $[0, \pi]$.
However, this method would lead to an incorrect distribution. Indeed, a point on a spherical surface having polar coordinates (r, ϕ, θ), shown in figure A.1, in Cartesian coordinates is becomes:

$$\begin{aligned} x &= r \sin\phi \cos\theta \\ y &= r \sin\phi \sin\theta \\ z &= r \cos\phi \end{aligned} \tag{A.1}$$

therefore, the differential solid angle is given by

$$d\Omega = \sin\phi d\theta d\phi \tag{A.2}$$

The differential solid angle is a function of $\sin\phi$, so for the same solid angle value the spherical area will be lower at the poles than near the equator. Therefore picking values of ϕ uniformly distributed in $[0, \pi]$ would result in a points distribution "bunched" near the poles of the sphere. Indeed, the points would be uniformly distributed in the $\theta\phi$ plane, but being the area lower at the poles, the

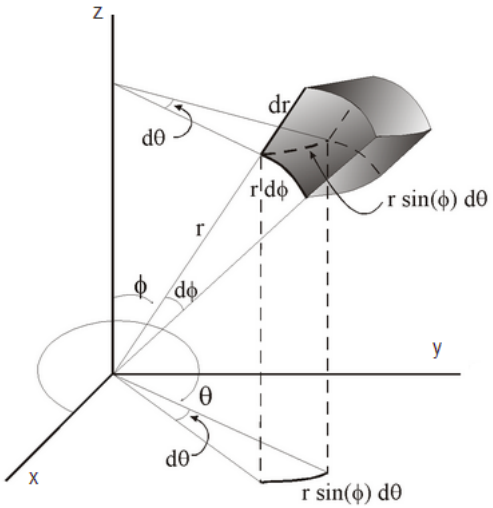

Figure A.1: Infinitesimal portion of a spherical surface. [45]

points distribution would be more dense, as shown in figure A.2.

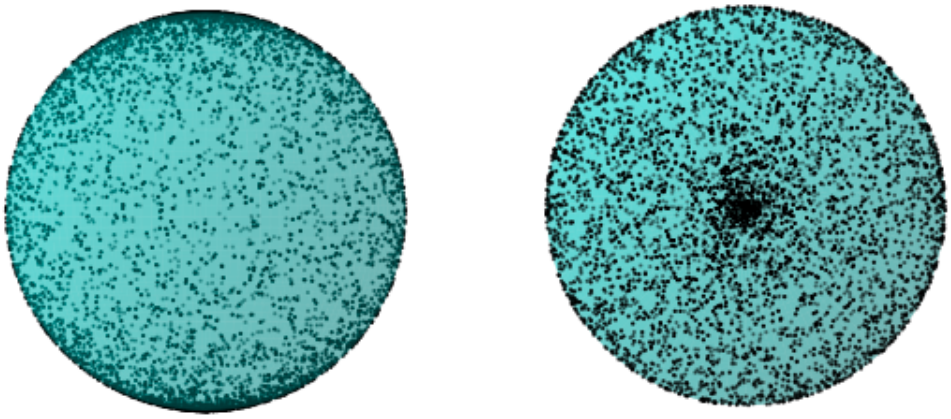

(a) (b)

Figure A.2: Example of points distribution selecting ϕ and θ uniformly distributed in $[0, 2\pi)$ and $[0, \pi]$, side (**a**) and top (**b**) views. [45]

Let's compute the correct θ and ϕ distributions to be used.

The probability that a points lies in an infinitesimal cone is

$$P(\Omega)d\Omega = P(\phi, \theta)d\phi d\theta \tag{A.3}$$

Since the surface area of a unit sphere is $A = 4\pi$, the probability density function (PDF) is $P(\Omega) = \frac{1}{4\pi}$.
Replacing $P(\Omega)d\Omega$ using the PDF just found and the relation A.2, it results:

$$P(\phi, \theta) = \frac{\sin\phi}{4\pi} \tag{A.4}$$

so

$$P(\theta) = \int_0^{\pi} P(\phi, \theta)d\phi = \frac{1}{2\pi} \tag{A.5}$$

$$P(\phi) = \int_0^{2\pi} P(\phi, \theta)d\phi = \frac{\sin\phi}{2} \tag{A.6}$$

Once the PDF with respect to θ and ϕ have been found, to generate random values following these PDF is sufficient to generate values from their cumulative density functions (CDF), $F(\theta)$ and $F(\phi)$

$$F(\theta) = \int_0^{\theta} P(\theta\prime)d\theta\prime = \frac{\theta}{2\pi} \tag{A.7}$$

$$F(\phi) = \int_0^{\phi} P(\phi\prime)d\phi\prime = \frac{1 - \cos\phi}{2} \tag{A.8}$$

To distribute points such that any small area on the sphere expected to contain same number of points, we choose two independent random variables $u = F(\theta)$ and $v = F(\phi)$ uniformly distributed in $[0, 1]$, and solving for θ and ϕ it will result

$$\theta = F^{-1}(u) = 2\pi u \tag{A.9}$$

$$\phi = F^{-1}(v) = \cos^{-1} 2v - 1 \tag{A.10}$$

Thus, θ would follow a uniform distribution, while ϕ would follow a sine dependency in order to avoid a thickening of points near the poles.
The correct $\theta\phi$ distributions are shown in figure A.3, resulting in a distribution in a spherical surface shown in figure A.4.

Generating pairs of uncorrelated electrons and positrons, both emitted isotropically, the correlation angle distribution will result in a sine distribution as shown in figure A.5.

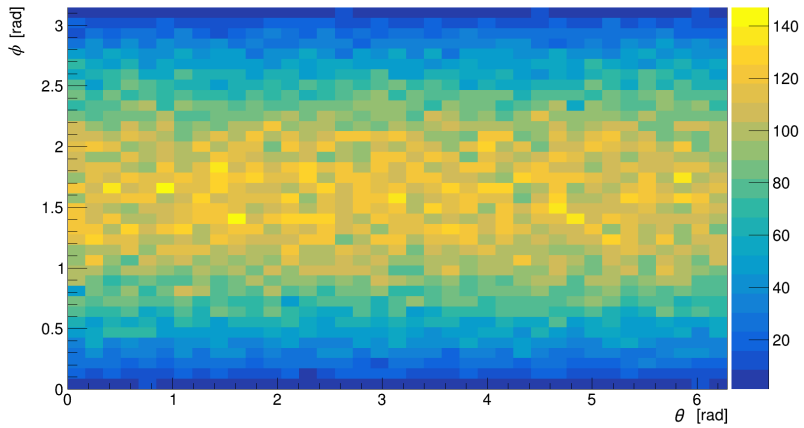

Figure A.3: Correct distribution on the $\theta\phi$ plane to obtain an isotropic distribution in the tri-dimensional space.

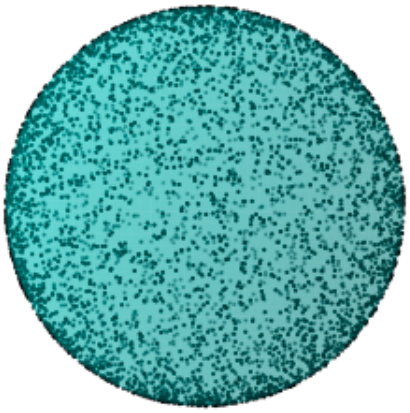

Figure A.4: Correct isotropic distribution. [45]

A.2 Angle correlated emission

In this section it will be presented a method to generate pairs emitted with a defined correlation angle, in example β, referring to figure A.6.
In particular, in the case discussed in this section the electron direction will be considered as fixed, and it will be described the correlation of the positron direction with respect to the electron one.
This would be useful to simulate pairs emitted following a certain correlation angle distribution in the future improvements of the simulation code.

Let's call $\hat{k}$ the electron emission direction versor, and $\hat{n}$ the positron one, where

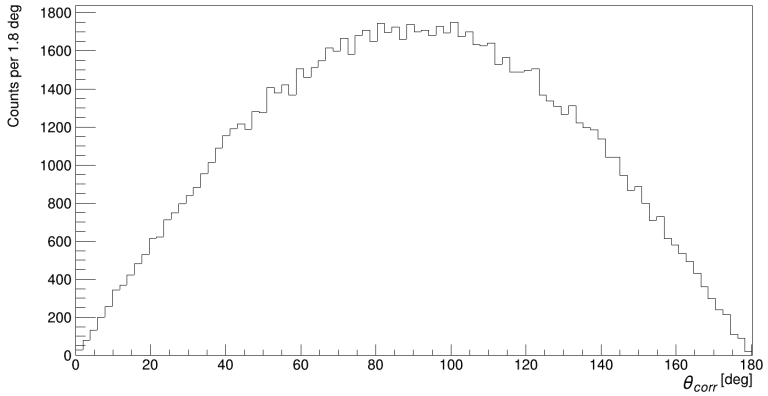

Figure A.5: **a** Correlation angle distribution obtained by emitting pairs of uncorrelated electrons and positrons, both isotropically distributed.

for simplicity both of them are unitary and applied in the origin O.
Given a fixed versor $\hat{k}$ and a fixed correlation angle β, there are infinite possible choices to generate $\hat{n}$. Indeed, considering a unitary sphere centered in O, the point $\hat{n}$ could be placed in an entire circle $S(\hat{k}, \beta)$ standing on the sphere surface, as shown in figure A.6.
Each of this possible versors could be obtained by rotating $\hat{k}$ with respect to a vector applied in O standing on the plane orthogonal to $\hat{k}$ containing O. Thus, in order to select one of the possible choices for $\hat{n}$, it is necessary to select also one of the vector standing on the plane orthogonal to $\hat{k}$.

So, in order to simulate a certain number of correlated pairs, it has been used the following method:

- generating the electron direction $\hat{k}$, following an isotropic distribution;
- obtaining a vector $\hat{u}_\perp$, applied in the same application point of $\hat{k}$, standing on the plane orthogonal to $\hat{k}$ itself;
- generating an angle ϕ uniformly distributed in $[0, 2\pi)$ and rotating $\hat{u}_\perp$ around $\hat{k}$ to be sure that the orthogonal vector is randomly selected and uniformly distributed in the orthogonal plane;
- generating an angle β, distributed following a selected correlation angle distribution, and rotating $\hat{k}$ around $\hat{u}_\perp$, finally obtaining $\hat{n}$.

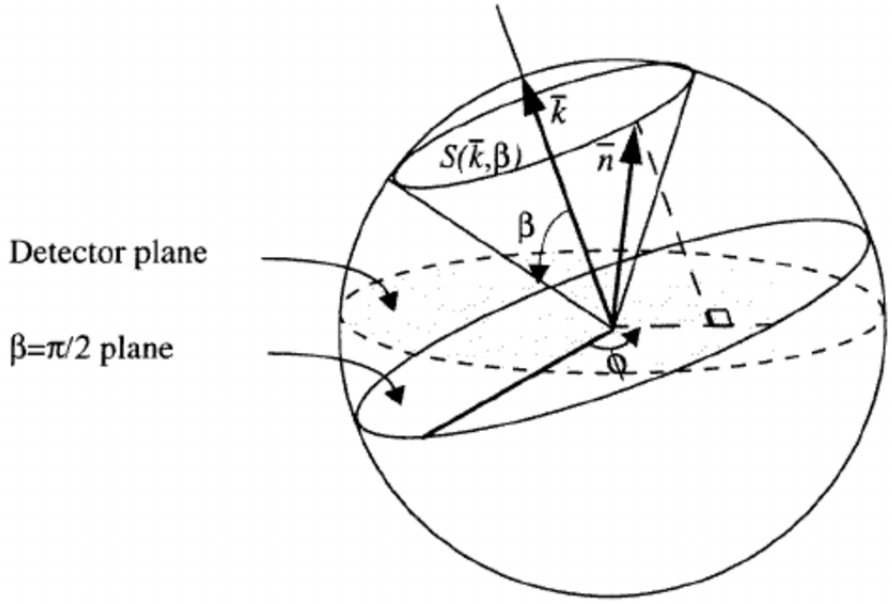

Figure A.6: Scheme of the possible choices to generate a versor $\hat{n}$ correlated to a given versor $\hat{k}$ by a correlation angle β, and of the method used to select just one of these choices. [46]